Montana Tech Library
Digital Commons @ Montana Tech

Graduate Theses & Non-Theses | Student Scholarship

Fall 2019

RECOVERY OF RARE EARTH ELEMENTS BY ADVANCED PROCESSING TECHNOLOGIES

Prince Sarfo

Follow this and additional works at: https://digitalcommons.mtech.edu/grad_rsch

Part of the Materials Science and Engineering Commons

RECOVERY OF RARE EARTH ELEMENTS BY ADVANCED PROCESSING TECHNOLOGIES

by

Prince Sarfo

A dissertation submitted in partial fulfillment of the requirements for the degree of

Doctor of Philosophy:

Materials Science

Montana Technological University

2019

RECOVERY OF RARE EARTH ELEMENTS BY ADVANCED PROCESSING TECHNOLOGIES

By

PRINCE SARFO

B.Sc., University of Mines and Technology, Tarkwa, Ghana, 2011
M.Sc., Montana Tech, Butte, Montana, 2016

Dissertation
presented in partial fulfillment of the requirements
for the degree of

Doctor of Philosophy
in Materials Science

Montana Technological University
Butte, MT

December 2019

Approved by:

Courtney Young

Dr. Courtney Young, Chair
Montana Technological University, Metallurgical and Materials Engineering Department

Hsin-Hsiung Huang

Dr. Hsin-Hsiung Huang, Professor Emeritus
Montana Technological University, Metallurgical and Materials Engineering Department

Dr. Avimayu Das, Professor
Montana Technological University, Metallurgical and Materials Engineering Department

Royce C Engstrom

Dr. Royce Engstrom,
University of Montana, Chemistry Department

Dr. Stephen Sofie, Professor
Montana State University, Mechanical and Industrial Engineering Department

Beverly K. Hartline, Vice Chancellor of Research and Dean of Graduate School
Montana Technological University

© COPYRIGHT

by

Prince Sarfo

2019

All Rights Reserved

Prince Sarfo, PhD in Materials Science, December 2019

Recovery of Rare Earth Elements by Advanced Processing Technologies

Chairperson: Dr. Courtney Young

Rare earth elements (REEs) are strategic materials of extreme importance to both military and civil applications. REEs are mined and processed because of their criticality. End of life rare earth metals are recycled for efficient use of natural resources and also to ensure supply of these critical raw materials. By using hydro- or pyro-metallurgical approaches, REEs can be processed from mined ore or recycled from magnets and other materials as rare earth oxides, fluorides and chlorides. Typically, rare earth oxides are dissolved in a molten halide bath, converted to metal by electrolysis at elevated temperatures, and then recovered as a liquid upon tapping and, later, as a solid upon casting and cooling. This research focuses on advanced separations which differences in physical and chemical properties of the molten bath are taken advantage of to yield effective recovery of neodymium metal. To achieve the neodymium metal recovery, a unique approach using novel potential (E)-pO^{2-} diagrams coupled with cyclic voltammetry (CV) and electrowinning (EW) was employed. Another aspect includes the use of a novel hydrometallurgical method to recycle neodymium magnets to produce neodymium fluoride so it could also become a feedstock to the molten bath considered in this work.

Keywords:
Rare earths, Molten Fluoride, E-pO^{2-} diagrams, Electrowinning, Cyclic-Voltammetry

Dedication

This dissertation is dedicated to my beloved family, friends and everyone who helped in the completion of this work. Thank you all for your prayers, sacrifice and advice.

Acknowledgements

I will like to thank Dr. Courtney Young for giving me the opportunity and guidance for the entire journey in this project. I also want to acknowledge Dr. Hsin-Hsiung Huang for teaching me his StabCal program; it was a critical part of this dissertation. Many thanks are also extended to Dr. Avimanyu Das, Dr. Royce Engstrom and Dr. Stephen Sofie for serving on my committee. Much gratitude to Mr. Thomas Frasz for the wonderful help on the recycling of the end-of-life hard drive magnet and special thanks to Mr. Gary Wyss of CAMP for his help in the use of some of the characterization equipment and laboratory. I am also extremely grateful to everyone in the Metallurgical and Materials Engineering Department.

Equally, I would also like to recognize my sponsor, the Devcom Army Research Laboratory, under Cooperative Agreement Number **W911NF-15-2-0020**. In views of that, any conclusions contained in this document are those of the author and should not be interpreted as representing the official policies, either expressed or implied, of the Army Research Laboratory or the U.S. Government. The U.S. Government is authorized to reproduce and distribute reprints for Government purposes notwithstanding any copyright notation herein.

Table of Contents

List of Tables

List of Figures

List of Equations

List of Acronyms and Symbols

Term	Definition
A	Ampere
Ag	Silver
AgCl	Silver chloride
Al	Aluminum
$AlCl_3$	Aluminum chloride
Aliquat 336	Tricaprylylmethylammonium chloride
B	Boron
C	Carbon
Ca	Calcium
CaF_2	Calcium fluoride or Fluorite
CaO	Calcium oxide or lime
Cd	Cadmium
CE	Counter/auxiliary electrode
Ce	Cerium
CeO_2	Cerium oxide or Ceria
Cl	Chlorine
Cl_2	Chlorine gas
ClO_4^-	Perchlorate
cm	Centimeter
CN	Coordination number
CO	Carbon monoxide
CO_2	Carbon dioxide
Cp	Heat capacity
CV	Cyclic voltammetry
Cyanex 272	Dialkyl phosphinic acid
Cyanex 923	Trialkylphosphine oxides
DOE	Design of Experiment
DODGAA	Dioctyldiglycol amic acid
Dy	Dysprosium
D2EHPA	Di (2-ethyl-hexyl) phosphoric acid
E	Potential
e^-	Electron
$E\text{-}pO^{2-}$	Potential partial oxygen pressure
EDX	Energy Dispersive X-ray
E_H-pH	Pourbaix
Eqn	Equation
Eu	Europium
EW	Electrowinning
F	Fluorine
F	Faraday constant
F_2	Fluorine gas
Fe	Iron

FeO	Iron (II) oxide
Fig	Figure
G	Grams
G°	Free energy
Gd	Gadolinium
H	Hydrogen
H	Enthalpy
HCl	Hydrochloric acid
Hg	Mercury
HgCl	Mercury chloride
$HmimHSO_4$	1-methylimidazolium hydrogen sulfate
HNO_3	Nitric acid
HREEs	Heavy Rare Earth Elements
Hrs	Hours
H_2O_2	Hydrogen peroxide
H_2S	Hydrogen sulfide
H_2SO_4	Sulfuric acid
I	Current
ICP-MS	Inductively Coupled Plasma – Mass Spectrometry
ICP-OES	Inductively Coupled Plasma – Optical Emission Spectrometry
IHP	Inner Helmholtz Plane
IT	Information Technology
K	Potassium
K	Kelvin
KCl	Potassium chloride
K_2O	Potassium oxide
kV	Kilovolts
La	Lanthanum
La_2O_3	Lanthanum oxide
Li	Lithium
LiCl	Lithium chloride
LiF	Lithium fluoride
Li_2O	Lithium oxide
Log	Logarithms
LREEs	Light Rare Earth Elements
Lu	Lutetium
M	Metal
M	Molar mass
M	Mass
MBMG	Montana Bureau of Mines and Geology
mm	Millimeters
mA	Milliamperes
$MgCl_2$	Magnesium chloride
Mo	Molybdenum
MREEs	Middle Rare Earth Elements
n	Number of electrons

Na	Sodium
Na_3AlF_6	Cryolite
NaCl	Sodium chloride
$NaNO_3$	Sodium nitrite
Nd	Neodymium
$NdCl_3$	Neodymium chloride
NdF_3	Neodymium fluoride
Nd_2O_3	Neodymium oxide
NdOF	Neodymium oxyfluoride
NiMH	Nickel metal hydride
O	Oxygen
O_2	Oxygen gas
OHP	Outer Helmholtz plane
PC 88A	2-ethyl-hexyl phosphonic acid mono-2-ethyl-hexyl ester
pH	Quantitative measure the acidity or basicity
PM	Permanent magnet
PPE	Personal Protective Equipment
Pr	Praseodymium
Pt	Platinum
Q	Total electric charge
R	Ideal gas constant
RE	Reference electrode
$REECO_3F$	Bastnaesite
REEs	Rare Earth Elements
Ref	Reference
REO	Rare Earth Oxide
RSM	Response surface methodology
ROM	Run-of-mine
$(REE,Y,Th)PO_4$	Monazite
S	Entropy
SClE	Standard Chloride Electrode
SDS	Safety Data Sheets
SEM	Scanning Electron Microscopy
SFE	Standard Fluoride Electrode
SHE	Standard hydrogen electrode
Si	Silicon
Sm	Samarium
SNE	Standard Nitrogen Electrode
StabCal	Stability Calculations for Aqueous Systems
UHP	Ultra-High Pure
U.S.A.	United States of America
USB	Universal Serial Bus
T	Temperature
t	Time
Tb	Terbium
TBP	Tributyl phosphate

V	Voltage
Versatic 10	Neodecanoic acid
V/s	Voltage per second
V_i	Stoichiometric coefficients
v/v	Volume per volume
w/w	Weight per weight
W	Current efficiency
WE	Working electrode
µm	Micros
wt	Weight
XRD	X-Ray Diffraction
Y	Yttrium
$(YREE)PO_4$	Xenotime
Z	Valance number of ions of a metal
Z	Electrochemical equivalent of the metal
Zn	Zinc
3D	Three dimensions
(g)	Gas
(l)	Liquid
(s)	Solid
-	Minus or negative
+	Plus or positive
=	Equal to
>	Greater than
<	Less than
:	Colon
{}	Brackets
%	Percent
°C	Degrees Celsius
ΔE	Change in potentials
ΔG	Change in free energies
Σ	Summation
η	Overvoltage
ΔH	Change in enthalpy
ΔS	Change in entropy

1. Overview of Rare Earth

1.1. Definition of Rare Earths

Rare earth elements (REEs) encompass of seventeen elements: scandium (Sc), yttrium (Y) and the succession of fifteen elements on the periodic table known as the lanthanides (La-Lu) as shown in Figure 1 [1, 2]. The term 'rare earths' can be ambiguous, not with respect to their abundance in the earth's crust, but to the inconspicuous appearance of the minerals from which they were originally isolated. These REEs, with the exception of radioactively unstable promethium (Pm), are more in the earth's crust than silver (Ag) and gold (Au). Cerium (Ce) is the most abundant. In essence, the REEs become less abundant with increasing atomic weight. However, in determining their abundance, the REEs become scarcer with increasing atomic number and those with even atomic numbers are more abundant than neighboring ones with odd atomic numbers [3].

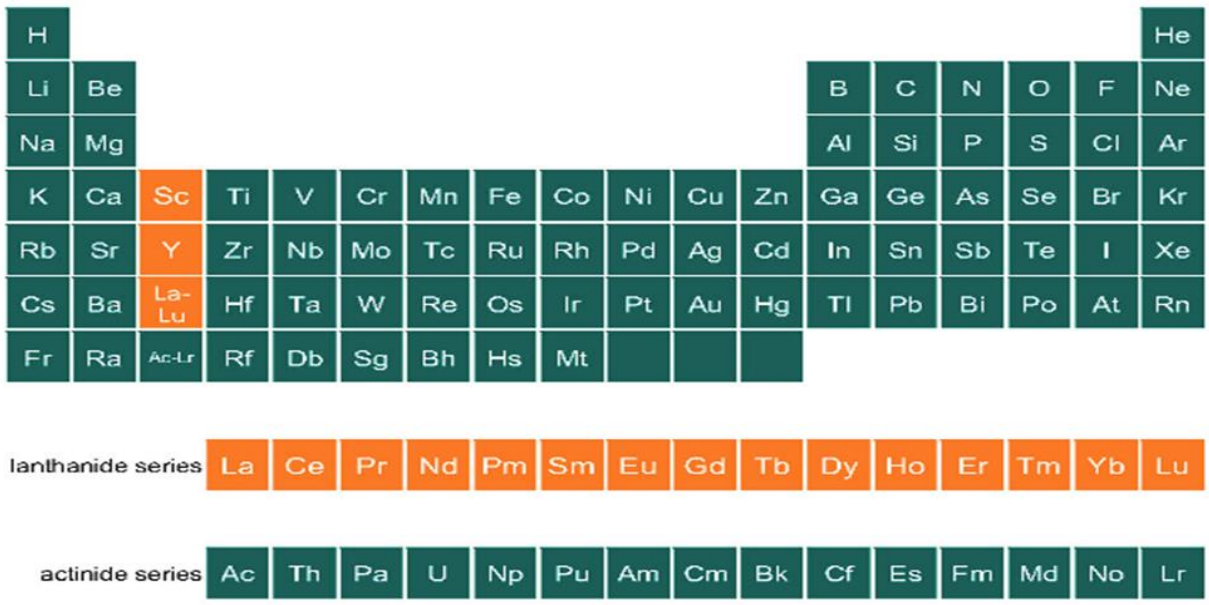

Figure 1: The Periodic table showing the Rare Earths

Furthermore, per their atomic weights, REEs are routinely categorized into two groups specifically light rare earth elements (LREEs) and heavy rare earth elements (HREEs). LREEs on the periodic table array from lanthanum (La) to gadolinium (Gd) and HREEs from terbium (Tb) to lutetium (Lu) plus Sc and Y which are also considered HREEs because of their comparable chemical and physical properties. In recent times, pending the source, REEs have been grouped to include Sm to Dy as the middle rare earth elements (MREEs) [4].

1.2. Ore and Occurrence of Rare Earths

There are more than 200 known REE-bearing minerals. Bastnaesite ($REECO_3F$), xenotime ($(Y,REE)PO_4$), and monazite ($(REE,Y,Th)PO_4$) are cogitated as the most common. Due to this, these minerals are deemed the most realistic for studying the extraction of REEs with LREEs abundant in bastnaesite and monazite and xenotime being rich in HREEs [5-8].

Geologically, these elements and minerals originate in connotation with alkaline to peralkaline igneous complexes which form from magma cooling derived by small degrees of partial melting of rocks in the Earth's mantle. Pegmatites attendant with alkaline magmas are complex and not fully understood but can be thought of as a geologic process that extracts and concentrates those elements that do not fit into the structure of the common rock-forming minerals as well as in, or associated with, carbonatite intrusions [1, 2, 5]. In addition, perovskite mineral phases, mantle-derived carbonate melts and hydrothermal deposits associated with alkaline magmatism, all contain a variety of rare-earth minerals [2, 6]. For now, the main production of REEs around the world are from carbonatite deposits found at Mountain Pass, California, United States of America (U.S.A) and three in China: Bayan Obo in inner Mongolia, the Maoniuping and Daluxiang deposit in Sichuan Province, and the Weishan deposit in Anhui Province [9]. These Chinese deposits account for over 75% of concentrate production.

Ore deposits of rare earths are typically made up of two or more rare earth element phases. Hence, deposits in which one elemental phase has a larger concentration have the modest advantage to be considered an ore. Because of that, of the hundreds of potential REE projects around the world, only a very few projects are in an advanced stage of development and may commence mining operations within the foreseeable future, particularly those containing HREEs. However, better and more economical processing technologies are needed [10]. It is worth noting that the concentrates from Mountain Pass in the U.S.A. are sold to China because the Chinese have the only REE refining capabilities. In this regard, China controls over 96% of REE production. This "monopoly" is reason why Mountain Pass has shut down and why the U.S.A. has deemed REEs as critical materials. In addition, the Chinese will dump REEs on the market to prevent it from being reopened let alone other deposits from being developed. The main question is "Will the Chinese government continue to control the REEs they export?" Consequently, the research being reported herein takes on added meaning [11].

1.3. Applications of Rare Earths

REEs are used in both consumer products and industry in diverse forms. For instance, cerium oxide (CeO_2) is used in the fabrication of some glasses that require exactitude polish and decolorization. Likewise, Ce-based catalysts are employed in automotive catalytic converters [12]. Other form of catalysts from REEs like the La-based are also used in petroleum refining. These catalysts are indispensable for the breaking down of heavy hydrocarbon molecules into smaller molecules which enables more production of oil processed in petroleum refineries.

In the field of metallurgy, REEs are used as additives and in alloys. Example, permanent magnets are made from alloys of neodymium-iron-boron and demand for these magnets have rapidly grown in recent years because the magnets are known to be stronger than all the other

types of magnets. Their usage includes computer hard drives, cell phones, electric motors for hybrid vehicles and windmills, actuators in aircrafts, etc. as shown in Table I [13]. It is important to point out that REE-magnet due to their strong magnetism, allow these consumer devices to be small. Their continued development will allow further miniaturization to continue [11].

From the platform of defense and security, REEs are also engaged in metal form to manufacture high precision guided munitions, lasers, radar, sonar, communications, displays, jet engines, and many more applications [14-17]. These REE markets are also listed in Table1. Owing to their exceptional physical and chemical properties, REEs are unable to meet the industrial needs for the manufacturing sector because some of these materials have been identified to be critical materials as shown in Figure 2 [26-28]. Apart from other factors like lack of collection and recycling, environmental issues that accompany the production of the materials, the main reason why some of these materials are categorized as critical materials is geopolitical.

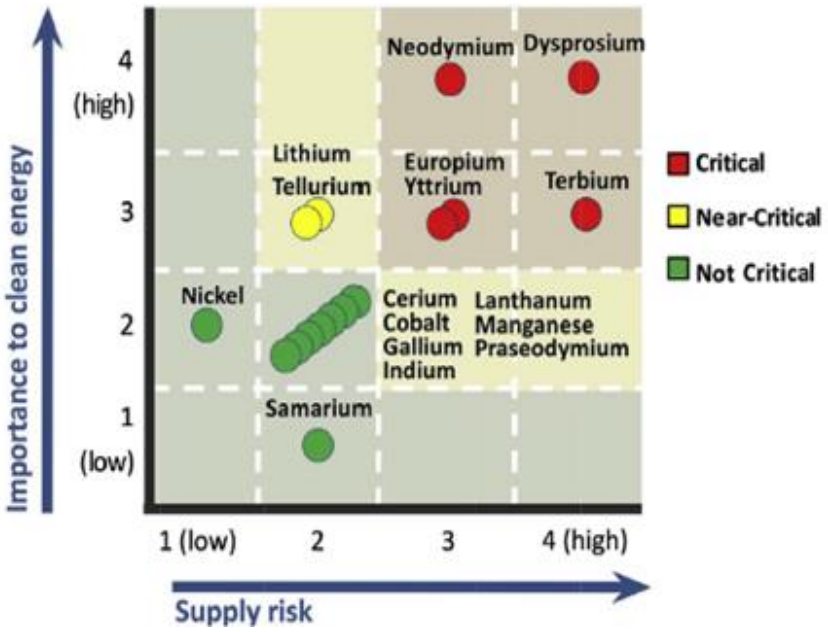

Figure 2: The five most critical being rare-earth elements [26,27]

Table I: Abundance, resources, production and usage of individual REEs [18]

Element	Crustal Abundance (ppm)	Resources (tonnes)	Production, tonnes/annum (years of reserve)	Uses, Source of Data and References
Lanthanum (La)	32	22,600,000	12,500 (1,800)	Hybrid engines, metal alloys [19], catalysis, phosphors [20], Carbon Arc Lamps, cigarette lighter flints [21]
Cerium (Ce)	68	31,700,000	24,000 (2,000)	Catalysis particularly auto [22], petroleum refining, metal alloys [19], Phosphors [18], corrosion protection, Carbon Arc Lamps, cigarette lighter flints [21, 23]
Praseodymium (Pr)	9.5	4,800,000	2,400 (2,000)	Magnets [19], Optical Fibers, Carbon Arc Lamps [21]
Neodymium (Nd)	38	16,700,00	7,300 (2,300)	Catalysis particularly petroleum refining [19], hard drives in laptops, headphones, hybrid engines, Nd-Fe-B magnets [21]
Promethium (Pm)	NA	NA	NA	Nuclear Battery [21]
Samarium (Sm)	7.9	2,900,000	700 (4,100)	Sm-Co magnet, IR absorption in glass [21]
Europium (Eu)	2.1	244,333	400 (610)	Red color for TV and computer screens [19], (5%Eu,95%Y), green phosphor (2%Eu) [20]
Gadolinium (Gd)	7.7	3,622,143	400 (9,100)	Magnets, nuclear magnetic resonance imaging, phosphors [21]
Terbium (Tb)	1.1	566,104	10 (57,000)	Phosphors [20] particularly for fluorescent lamps [21], magnets [19]
Dysprosium	6	2,9800,000	100 (209,800)	Magnets [19], hybrid engine [19, 21], can increase the coercivity of Nd-Fe-B magnets.
Holmium (Hm)	1.4	NA	10	Glass coloring agent, lasers [19]
Erbium (Er)	3.8	1,850,000	500 (3,700)	Red, green phosphors, amplifiers for optical fibers transmission, pink in glass melts, sunglasses [21]
Thulium (Th)	0.48	334,255	50 (6,700)	Medial X-ray units—X-ray sensitive phosphors [21]
Ytterbium (Yt)	3.3	1,900,000	50 (38,00)	Laser, steel alloys—grain refiner [19,21], stress sensors [21]
Lutetium (Lu)	NA	395,000	NA	Catalysts in petroleum refining, Ce-doped Lu-glass used in positron emission tomography (PET) as detectors [18]
Yttrium	30	9,000,000	8,900 (1,011)	Red phosphors [20], fluorescent lamps, metals, Y-Fe-garnets resonators [19], ceramic [23,24]
Scandium	22	NA	400 kg primary production, 1600kg/year from Russian stockpile	Aluminum-scandium alloys for aerospace industry [25], defense industry, and high intensity discharge light.

Although every market experiences price fluctuations, they are usually a consequence of major events; however, the high prices with REEs are mostly conjectured from tension between nations. For examples, China and Japan have a dispute over the Senkaku Islands in the East China Sea and U.S.A. and China are in a trade war. These geopolitics have resulted in reduction of export quotas of rare earth oxides (REOs) from China to both Japan and the U.S.A. helping illustrate why REEs have been named a critical material. In this case, the Chinese have a monopoly on REEs which has resulted in high commodity prices, particularly HREEs [29].

2. Scope of the Research

2.1. Research Goals

The drive of this research is to recover REEs using advanced separation technologies by studying their electrochemical behavior in molten salts of alkaline halides and developing a novel recycling process. These will be accomplished by using cyclic voltammetry (CV) and electrowinning (EW) in pyrometallurgical studies and applying hydrometallurgical practices such as leaching, precipitation and ion exchange in recycling. To do these, techniques including X-Ray Diffraction (XRD), Inductively Coupled Plasma (ICP) Spectroscopy, and Scanning Electron Microscopy with Energy Dispersive X-ray (SEM/EDX) will be employed for structure, composition, physical properties and surface analysis. Several properties will also be investigated in order to determine the optimal properties needed for REE production to occur with high process efficiency and low cost/energy consumption. Thus, specific goals of this research are to:

- Minimize the melting temperature for energy efficiency;
- Maximize the solubility/ionization of REEs without chemical interaction;
- Use potential (E)-pO^{2-} diagrams of the REE to molten salt explain thermodynamics;
- Modify the cell design as needed to conduct CV and EW experiments;
- Recover rare earth metal from the electrolysis process;
- Optimize the metal recovery in the molten halide bath;
- Develop a hydrometallurgical process to recycle REE- magnet; and
- Focus on the producing REE fluoride so it will be a feedstock to the molten salt.

For the electrolysis process (pyrometallurgical method), the rare earth oxide (REO) is first dissolved in a molten bath and then electrically deposited as metal by reduction on the

cathode while simultaneously evolving a gas or gases by oxidation on the anode. When used in this manner, electrolysis is often referred to as electrowinning. Thermodynamic evaluations by calculating novel E-pO^{2-} diagrams showed conditions needed to obtain Nd metal and ternary/binary phase diagrams suggested there would be solubility limitations driven by not only temperature but also by bath chemistry. By using Nd as the main REE in this work, it demonstrates that Nd molten-salt electrolysis is complicated due to the physicochemical relationships involved and therefore is not straight forward. However, in order to develop a fundamental understanding of the process, statistically designed experiments were also used to understand molten-salt electrolysis of Nd and allow for the technology to be applied to other REEs. Similarly, by developing a technology for recycling Nd magnet into a product that will be a feedstock to the molten salt electrolysis process, it will simultaneously become a sustainable process and thereby save our natural resources.

2.2. Safety Protocols

Safety was a priority in this project in order to prevent an accident in the workplace due to the chemicals and equipment used:

- Personal Protective Equipment (PPE) was used per the job requirement: eyeglasses, rubber and thermal gloves, lab and thermal coat, and ear plugs.
- Chemical handling and disposal criteria for various materials per Montana Tech standard were followed due to the all of the waste generated.
- Laboratory, housekeeping and chemical hygiene were performed following all experimental work including following all Safety Data Sheets (SDSs) processes for cleaning chemicals upon spillage or contact with the skin.
- All chemicals were stored in their appropriately labeled cabinets after use.

- All electrowinning and cyclic voltammetry work were performed under a fume hood to prevent exposure to off gasses.
- Electrical safety rules were followed to help prevent shock and electrocution from the misuse of the electronic instruments which also included checking the equipment for damaged cords or plugs and having them repaired or replaced as needed.
- Finally, high voltage equipment was turned off and or adjusted always with one hand with the other hand behind my back per stray voltage/current protocols.

2.3. Finding and Layout

With an overview of REEs covered in Chapter 1 and research goals laid out in Chapter 2, the research can now be presented. REEs beneficiation and procedures for the techniques used herein are described in two chapters. Chapter 3 involves developing a hydrometallurgical process to recycle Nd magnets to produce rare earth oxide or fluoride which are feedstock components to the molten bath. Chapter 4 focuses on developing and optimizing a pyrometallurgical process and its theoretical consideration.

In Chapters 5 and 6, E-pO^{2-} diagrams for Nd and other REEs are presented and used in helping determine the potential window at which electrowinning of the REEs are achievable, namely Nd. Chapters 7 and 8 contain the results of characterization and analysis by XRD, SEM/EDX and ICP-MS/OES; whereas, Chapters 9 and 10 are used to optimize the Nd electrowinning process by statistical modelling through varying critical process parameters. Chapters 11 and 12 are used to specifically compare cyclic voltammetry experiments of Nd with thermodynamically calculated E-pO^{2-} diagrams. Finally, Chapter 13 presents a summary of the general conclusions and proposes potential future work based on the research findings. This future work is intended to give direction on how to help improve upon the process.

3. Rare Earth Beneficiation

Aside from recycling or being made as by-products, REEs are mostly mined and processed as shown in Figure 3. Production from mining is either open pit or underground but is directly established on demand and supply with ore grades ranging from <1% to about 15% REEs by weight of the mined ore [7, 30].

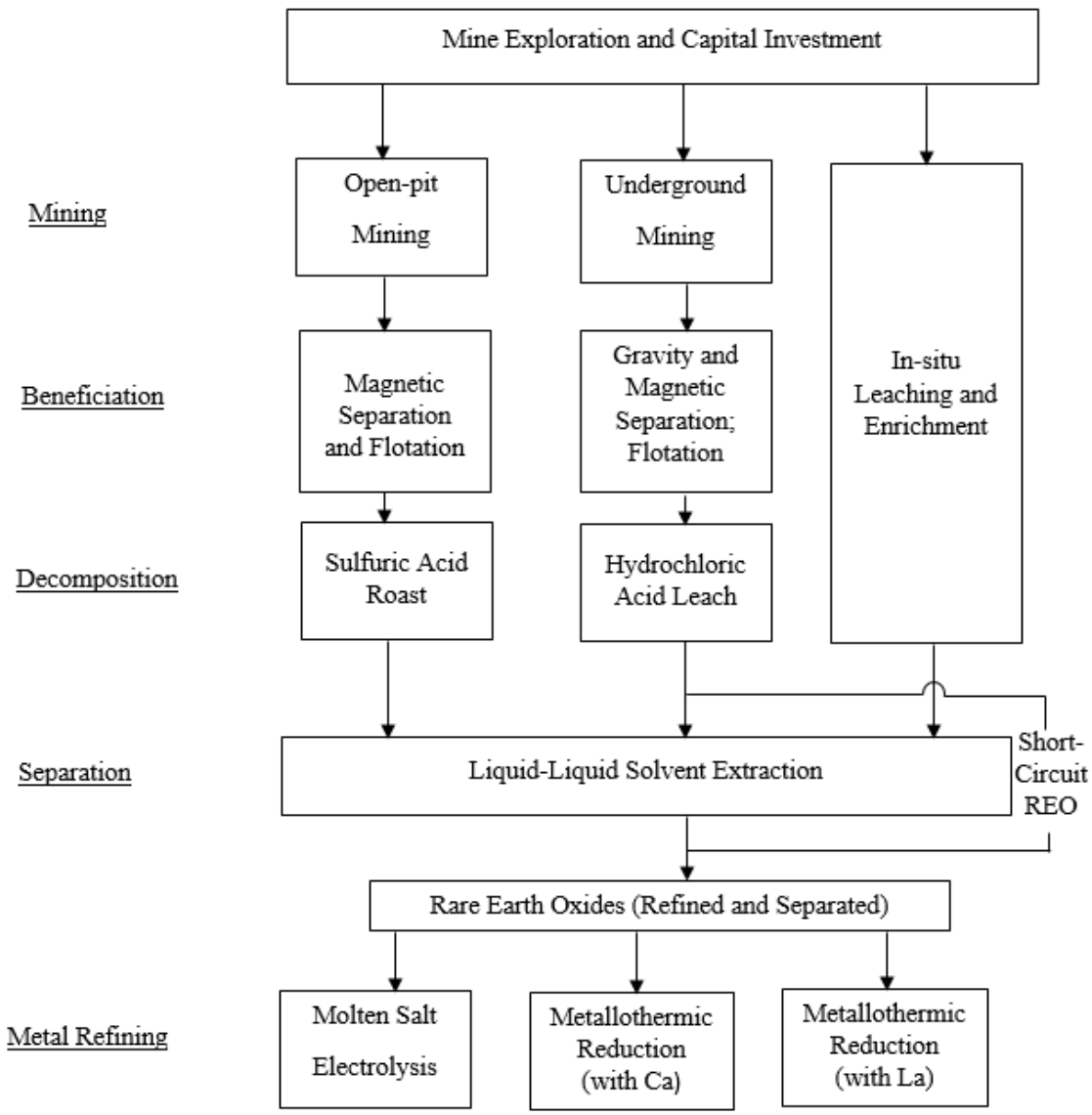

Figure 3: Flow chart for mineral processing and extractive metallurgy of REEs into final products [31]

Run-of-mine (ROM) ores containing REEs are comminuted by crushing and grinding to a particle size appropriate for mineral separation. Flotation is the most common separation process employed. In flotation, the ores are pulped and various chemicals (i.e., collectors, modifiers, and depressants) are added to make the valuable REE-bearing minerals selectively hydrophobic. Air bubbles are then used to separate them from the gangue minerals with the REEs adhering to the bubbles and floating to the top of the cell as a froth. Another chemical, called a frother, is added to stabilize the froth which is then scraped off to form a concentrate. This process typically befalls at the processing plant and, for the duration, the REE-bearing minerals are upgraded to 50–70% REEs content by weight. For non-Chinese ores, the minerals of interest are usually bastnaesite and monazite. By comparison, for the Chinese ores, the REE minerals are ion-exchange clays that are upgraded to at least 90% [30].

Further processing of the REE-bearing concentrate is done in an extractive manner to separate each REE into their respective pure forms. Each REE may have its own unique extraction steps and chemical processes; however, that may necessitate numerous steps to achieve ideal purity. After separation, the REEs are generally in their oxide form; hence, the final processing stage is to convert the REOs to metal so they can be made into final products.

Global REO production through mining grew with an average growth of 5% per year from 1990 through 2007 and is still growing [30]. In terms of total global mining in 2016, China represented a total of 85%, Australia 10%, and 5% was other including the U.S.A. [7, 32-35]. This made China the world leading producer of REOs as shown in Fig. 4. Also, a significant fraction of global REE reserves that are economically advantageous in terms of exploitation are also located in China with their reserves standing at 97%, 2% for India and 1% for Brazil. This makes the whole world dependent on China for REEs [34].

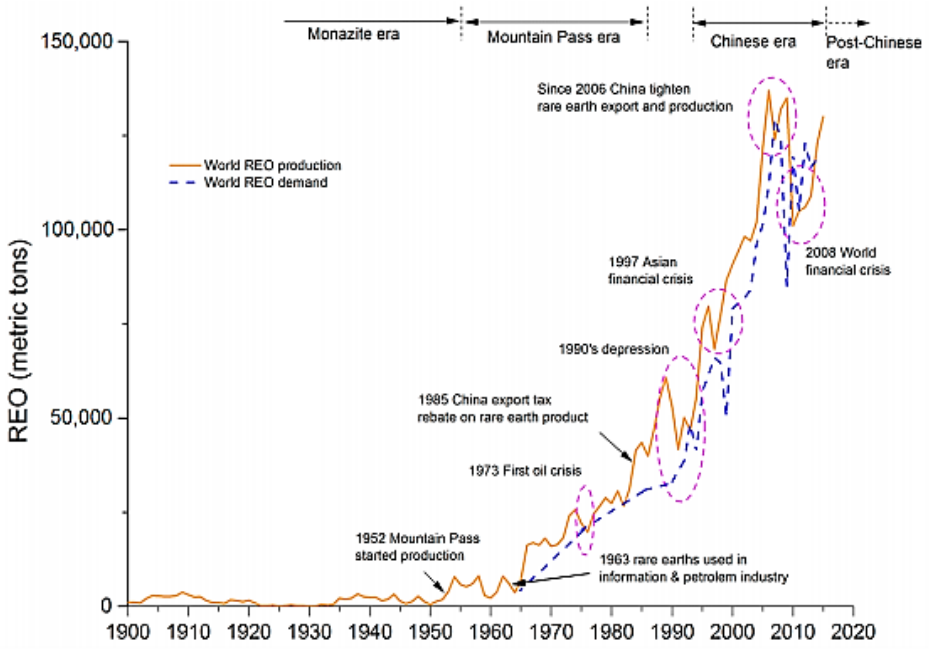

Figure 4: Global REO production in 1956-2010 [35]

However, with China tightening its export quota from 50,145 tons in 2009 to only 31,130 tons in 2012 in order to address serious environmental pollution and ecological destruction from mining and processing, REEs are in short supply [28]. These situations also have contributed to the criticality of the materials. To solve these problems, production with less environmental issues have to be implemented [36].

Likewise, REE recycling from alternative sources, such as industrial wastes, have become important and can provide an efficient way to control natural resource use and to ensure supply of these critical materials. But, notwithstanding all the research work done over the years to help recycle these materials, commercial recycling of REEs is low with less than 1% of REEs being recycled in 2011 due mainly to inefficient collection, technological difficulties, and lack of incentives [37-41].

3.1. Hydrometallurgical Processes

When elements of interest are found in two or more mineral phases and each require a different processing technology, hydrometallurgical approaches are the common and efficient way to extract the REEs. Hence, for REEs of similar chemical and physical properties, leaching is done first [17, 38, 42]. REE leaching is commonly done directly by adding lixiviants such as sulfuric acid (H_2SO_4), hydrochloric acid (HCl), perchlorate (ClO_4^-), and nitric acid (HNO_3) with or without heat treatment of solids to aid REE dissolution. Once in solution, various processes such as solvent extraction, ion exchange and precipitation can be used to economically produce individual REEs in the required form [43, 44].

For solvent extraction, different cationic, anionic and solvating extractants such as di (2-ethyl-hexyl) phosphoric acid (D2EHPA), dialkyl phosphonic acid (Cyanex 272), 2-ethyl-hexyl phosphonic acid mono-2-ethyl-hexyl ester (PC 88A), neodecanoic acid (Versatic 10), tributyl phosphate (TBP), and tricaprylylmethylammonium chloride (Aliquat 336) have been reported for the separation of REEs from solution with D2EHPA being more commonly used with nitrate, sulfate, chloride and perchlorate solutions, PC 88A with chloride solutions, and TBP with nitrate solutions [44-55]. Interestingly, many of the same chemical types used as solvent extractants are used in solid form as resins for ion exchange purposes from the same type of leaching solutions [56, 57]. For both solvent extraction and ion exchange, the REE-loaded material must then be selectively stripped. Resulting solutions are then predominantly processed to precipitate the individual REEs, often as REOs, but not always [2, 58-60].

As reported, Tian et al. (2016), Tunsu et al. (2016), and Yang et al. (2013), in their recycling of phosphor powder from waste cathode ray tubes, employed acid leaching technology [59-63]. Tian et al. adopted an "H_2SO_4 + H_2O_2" system to minimize the release of hydrogen

sulfide (H_2S) into the atmosphere. Their results demonstrated the recovery of Y and Eu had highly positive profits and Zn and Al gave negative profits due to their lower enrichment factors [61]. Tunsu et al., also after leaching, separated REEs with Cyanex 923, a commercial mix of trialkylphosphine oxides, in a counter-current mixer/setter system comprising three extraction and four stripping stages, respectively. They produced a Y-Eu concentrate which was further precipitated with oxalic acid and then thermally treated to produce an oxide containing 99.96% REEs of which 94.61% was Y, 5.09% Eu and 0.26% are the other REEs extracted alongside [62]. Yang et al., on the order hand, used an ionic liquid with NN-dioctyldiglycol amic acid (DODGAA) as novel extractant system and reported an effective recovery of Y, Eu, La and Ce [63].

Additionally, Yoon et al. (2016) reported recycling strategies for permanent magnets (PM) for the recovery of Dy and Nd using solvent extraction [64]. They discussed the use of organophosphorus extractants and compared D2EHPA and PC 88A. They varied experimental conditions such as the maximum loading rates, theoretical extraction stages, scrubbing processes, and stripping processes for both extractants and found that, in a comparative case study, that both the extractants (D2EHPA and PC 88A) can be used for REE recovery from permanent magnet (PM) scrap leach liquors with significant recovery efficiencies. Nonetheless, comparing to each other, PC 88A outperformed D2EHPA. Both systems used kerosene as a diluent.

Sahin et al. (2017) studied the recycling of REEs and base metals from slag powders of nickel metal hydride (NiMH) batteries by leaching with an ionic liquid, 1-methylimidazolium hydrogen sulfate ($HmimHSO_4$) [65]. REEs such as La, Ce, Nd and Y (total 22.50% w/w) with the maximum leaching efficiencies of only 15% for La and Ce, 20% for Nd and 100% Y even

after a thorough investigation where temperature, particle size and time were systematically varied.

3.1.1. Recycling of Neodymium Magnet

For this research, hydrometallurgical methods were employed to produce rare earth fluoride which is part of the salt composition that will be used in subsequent pyrometallurgical experiments. In this part of the work, Nd magnets from end-of-life hard disk drives were used [66]. This component is found in system unit of computers and is used to store data electro-mechanically (i.e. digital usage of a rigid rapidly rotating disks is coated with magnetic material and information is stored and/or retrieved by the magnet). The rotating disks or plates are paired with magnetic heads arranged on the moving actuator arm, which reads and writes data to the rotating disks surface (see Fig. 5).

Per the amount of REEs produce, neodymium usage in the production of NdFeB magnets from mining is about 13% and, of that, 34% of the magnets produced are used in the manufacturing of hard disk drives. Their life span is based on their application but is typically the life of the computer itself [67-69]. Hence, a recycling program could be established.

Another application of REEs in hard disk drives is in the manufacture of printed circuit boards (PCB) [68]. This magnet material is coated with a protective polymeric layer containing copper, aluminum or nickel, usually nickel [70].

Depending on required physical properties, NdFeB magnets may have multiple REEs at varied composition including other alloying elements. The specific addition of each element depends on the required material properties needed for their application [71, 72]. For example, cobalt is substituted for REE and Fe materials (up to 5%) to increase the curie temperature of the magnet [73, 74]. Also, the addition of dysprosium (Dy) increases the temperature characteristics

of the magnet but decreases the residual induction of the magnet. Recently, the use of praseodymium (Pr) as a substitute for Nd (20-25%) to lower production costs has also been on the rise [72,74]. Dy and Pr are LREEs and are therefore cheaper than Dy which is a HREE.

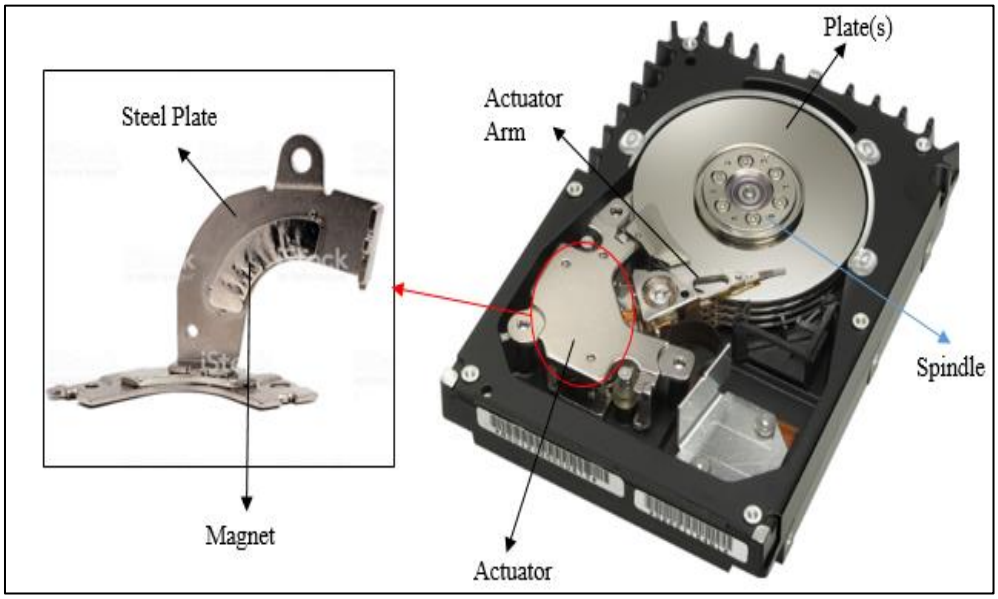

Figure 5: Parts of the hard disk drive and the magnetic component

3.1.2. Experimental

3.1.2.1. Materials and Reagents

Sample magnets were obtained from end-of-life computer hard drives from the Information Technology (IT) Department at Montana Tech. 98% sulfuric acid (H_2SO_4) from Pharmco Products Inc., 28-30% ammonium hydroxide (NH_4OH) from VWR International, and 98.8% ammonium bifluoride ($NH_4F{\cdot}HF$) from by J.T. Baker were the reagents used in the work.

3.1.2.2. Demagnetization

The actuator in the hard drives contains the magnet. So, for the demagnetization work, the actuators were removed from the hard drives, assembled and loaded in the Thermo Scientific

Lindberg/Blue M box furnace. The furnace was programmed to ramp up at 5°C per minute under air from room temperature to 500°C. When the temperature was reached, the magnets were placed in the oven for 60 minutes to demagnetize them as well as weaken the adhesive used to hold the magnet on the steel plate. Afterwards, the demagnetized magnets were air-cooled, and hand sorted from the steel plates.

3.1.2.3. Crushing and Size Analysis

Crushing and pulverizing were done to liberate the NdFeB part of the demagnetized sample so that it could be easily leached with the lixiviant due to the increased surface area of the material. Using a Bico pulverizer from Bico Inc., the samples were crushed and pulverized from dimensions 3.10 mm to 0.3 mm as determined by the gap on the pulverizer. A sieve analysis was performed to determine the size distribution of the comminuted material.

3.1.2.4. Leaching

REEs were leached from the crushed and pulverized sample in a 2M H_2SO_4 acid solution with sample solution ratio of 1g:10ml. This process was done under a fume hood for 2 hours with the acid solution being added in small amounts because of the aggressiveness of the reaction. Filtration was performed after leaching to separate the REE-acidic solution from the residue and SEM analysis shows the residue comprised mostly of nickel for the protective layer of the magnet. NH_4OH was then added to the filtrate in a ratio of 1ml NH_4OH to 20ml rare earth rich solution. Upon addition, the solution was stirred to completely dissolve back into solution the jade green precipitate that formed. After that, the solution was allowed to sit for 12 hours so the REE-rich precipitate could fully form and settle. Finally, filtration was also performed so the residue could be collected and allowed to dry. The dry REE-rich precipitate is then added into mixture of $NH_4F{\cdot}HF$ and deionized water in a ratio of 1g:1.5g:10g and stirred for 30 minutes.

Filtration were also done in this case, and the residue obtained after drying were mainly made up of NdF_3 and PrF_3. The flowchart for all of this hydrometallurgical recycling process is shown in Figure 6.

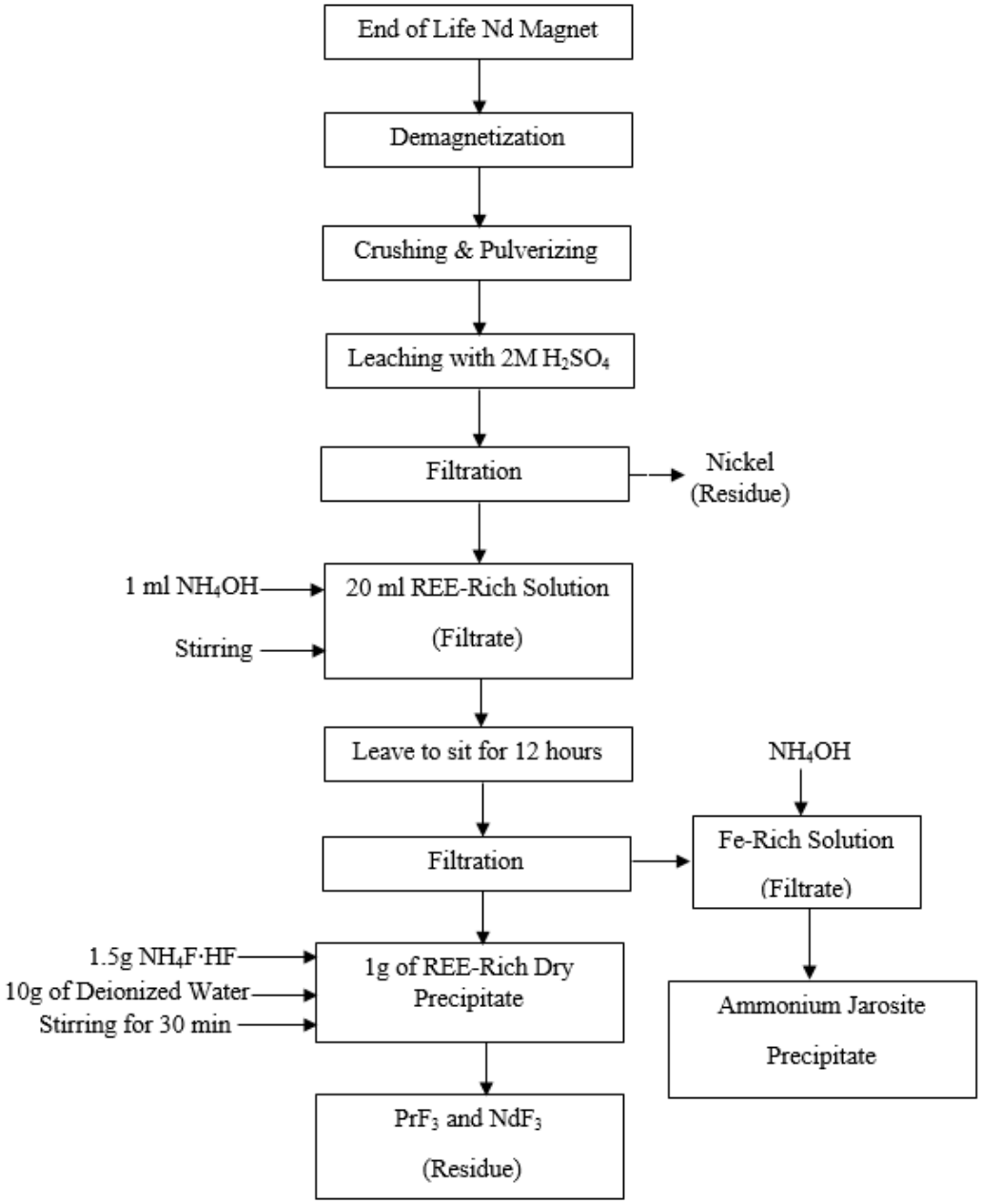

Figure 6: Flow chart of the hydrometallurgical recycling process

3.1.2.5. Characterization Experiments

Characterization studies were carried out on the precipitate and the final products after demagnetization using X-ray Diffractometry (XRD) and Scanning Electron Microscopy with Energy Dispersive X-ray (SEM-EDX).

3.1.2.5.1. SEM/EDX

SEM-EDX was engaged to determine the chemical composition of all phases in the demagnetized material using a TESCAN TIMA with a tungsten filament and an EDAX Z2 analyzer. A sample was hand-separated and hot-mounted with phenolic from MetLab Corporation in a TECHPRSS 2™ from Allied High-Tech Products Inc. Resulting mounts were ground and polished to a smooth finish and then conductively coated with carbon to obtain SEM images by Backscattered Electron (BSE) detection. EDX analyses helped determine the chemical composition of all products.

3.1.2.5.2. XRD

XRD was carried out with a Rigaku Ultima IV X-ray Diffractometer (XRD) using Cu-Kα radiation at 40 kV and 40 mA. This was used to quantify the materials and determine the various phases in the precipitates and the filtrate after $NH_4F{\cdot}HF$ addition.

3.1.3. Results and Discussions

3.1.3.1. Size Analysis

Using a sieve size ranging from 0.0059 inch to 0.185 inch, the size distribution of a crushed and pulverized sample is shown in Figure 7. From the plot, it is seen that 49.1% of the material passed the 0.0234-inch sieve.

3.1.3.2. SEM/EDX Results

Image from the Backscatter Electronic (BSE) demonstrates some dissimilar phases in the demagnetized magnet. EDX analyses were done on three spots. Each of the spots are shown in Figure 8 to have a distinctive chemistry: spot (a) contains Ni suggesting it is the protective coating; spot (b) is a combination of Pr, Nd and Fe with Pr substituting for Nd up to 20–25% Nd to lower production costs in the magnet itself; and spot (c) shows mixture of Nd and Fe and therefore is also part of the magnet. Boron (B) was not seen due to its low EDX activity (i.e., it has only 3 electrons and is therefore impossible to analyze).

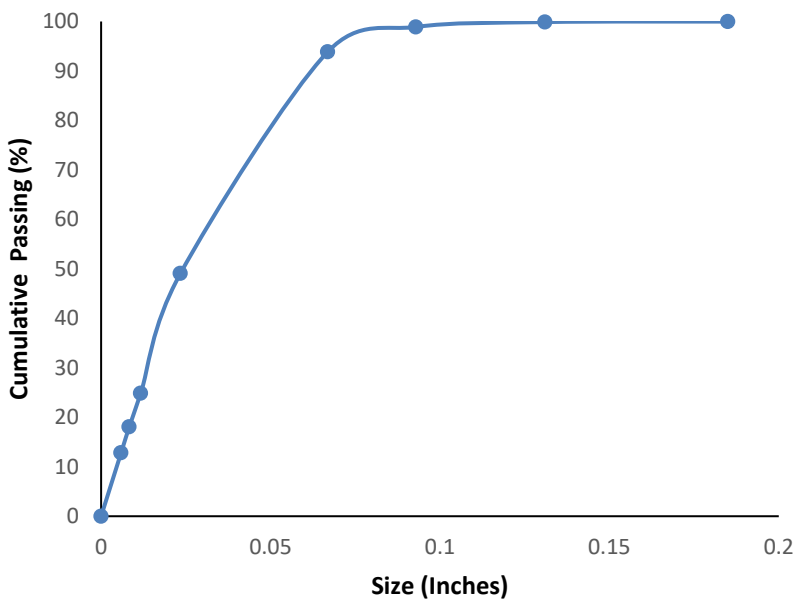

Figure 7: Cumulative particle size distribution of the pulverized demagnetized sample

3.1.3.3. XRD results

Figures 9 and 10 show the phase compositions in the precipitate (Fig. 9) and the dry filtrate after $NH_4F{\cdot}HF$ addition (Fig. 10). From Figure 9 it can be seen that most of the Fe remains in solution and that the precipitate consists mainly of $(NH_4)(Nd(SO_4)_2(H_2O)_3)$. This

precipitate chemically looks like ammonium jarosite if the Nd is replaced by Fe. Figure 10 also shows the phases of the product after the precipitate was made with in $NH_4F{\cdot}HF$ and stirred for 30 min. Based on the results, it can be concluded that NdF_3 can be produced from the recycling of Nd magnets from hydrometallugical processes and the product can be used as a feedstock to the pyrometallurgical processes examined next.

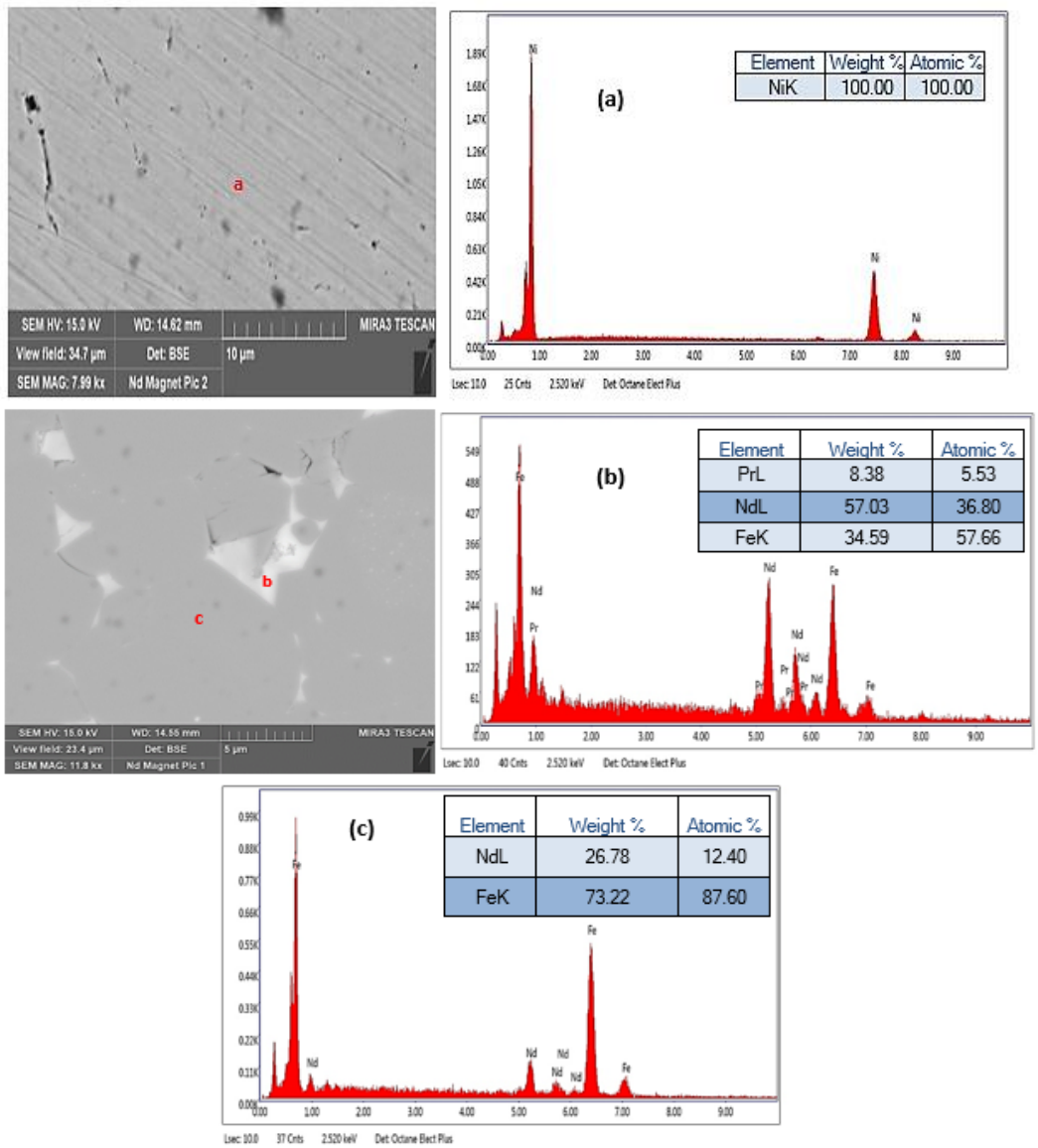

Figure 8: SEM morphology of the magnet

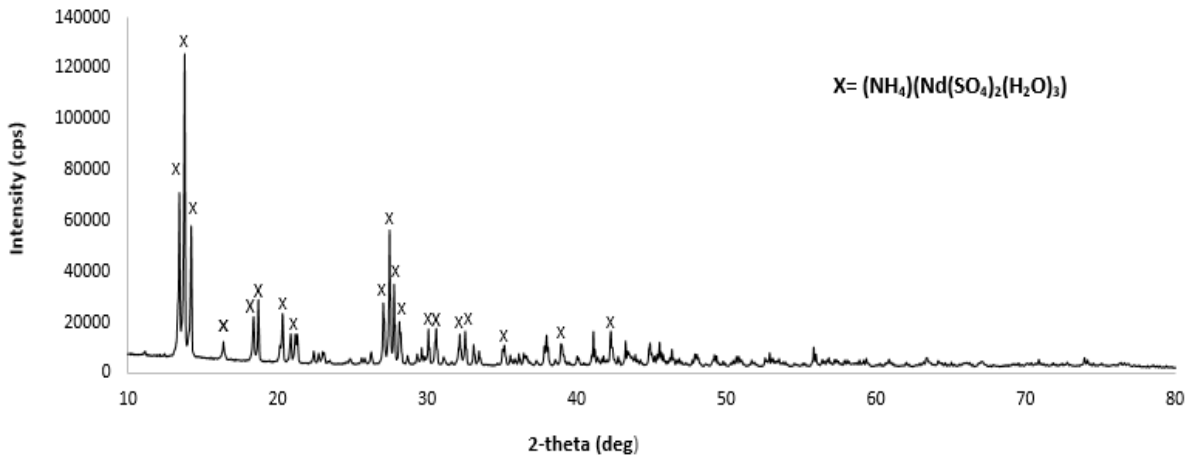

Figure 9: Crystal phases in the metal rich precipitate

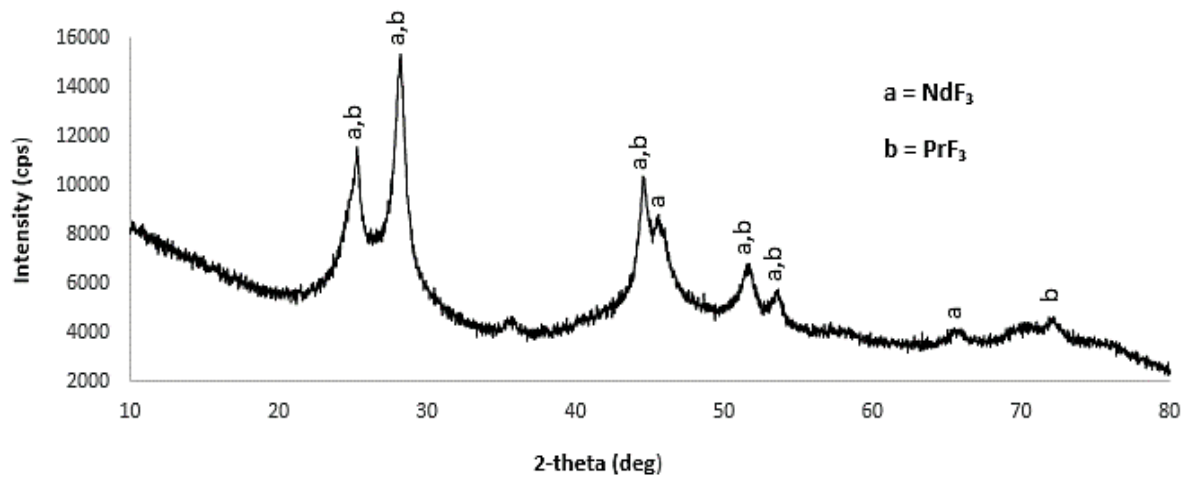

Figure 10: Crystal phases the filtrate after 30 min in $NH_4F{\cdot}HF$

3.2. Pyrometallurgical Processes

Rare earth metals cannot be electrochemically recovered from aqueous media because their negative deposition potentials are significantly below the stability region of water. On the other hand, pyrometallurgical processing provides an opportunity for the electrochemical formation of these metals [75]. If molten salt electrolysis is to be used, an appropriate bath

chemistry must be established. Likewise, if metallothermic reduction is to be used, a metal with an even lower reduction potential will be needed. In spite of all these problems, molten salt electrolysis and metallothermic reduction are currently the most commonly used pyrometallurgical methods employed to make REEs [76].

Metallothermic reduction, especially, is more widely used in REE metal preparation and, in the process, an active metal such as alkali and alkaline earth as well as aluminum are used to substitute for the REE. Typically, a REO salt is required as exemplified in Equation 1 with La_2O_3:

$$La_2O_{3(s)} + 3Ca_{(l)} \rightarrow 2La_{(l)} + 3CaO \qquad \text{Equation 1}$$

In this case, because molten Ca is used, it is analogous to the Kroll process for making titanium with molten magnesium [77, 78]. Furthermore, this technique has been used as a purification process as reported by Bose et al. (1984) who achieved a higher REE recovery producing an REE-Si-Fe alloy with better grade than the ones obtained by molten salt electrolysis using a commercial submerged arc technique [79]. Bose et al. used reduction experiments where a mixed REO was combined with ferro silicon and aluminum as reductants in the presence of a flux (CaO-MgO or CaO-CaF_2) to prevent the loss of REO into the slag phase. A 5-kg alloy per batch was smelted in an induction furnace at a temperature of 1500-1550°C. The resulting REE-Si-Fe alloy corresponded to more than 50% REE content and over 80% REE recovery.

Mayer et al. (1985) used metallothermic reduction of trichlorides of Eu, Yb, Sm, Tm, Dy and Nd [80]. La and Na produced chlorides of the divalent lanthanides when stoichiometric quantities were used. In this process, they employed a eutectic system such as LiCl-RCl_2 (where R = Nd, Sm and Eu) and NaCl-RCl_2 (where R = Sm, Eu, Dy, Tm and Yb), determined the lattice constants using XRD, and even refined the crystal structure of $SmCl_2$ as defined by its

coordination number (CN). MCl_2 (M = Nd, Sm and Eu) crystallinity showed $PbCl_2$-type structure (CN 9), $DyCl_2$ yield a $SrBr_2$-type structure (CN 8), and $TmCl_2$ and $YbCl_2$ gave the SrI_2-type structure (CN 7). Also, in the system of LiCl-RCl_2 (where R = Dy, Tm and Yb), it was reported to contain the ternary chlorides LiM_2Cl_5 and the crystal structure of $LiTm_2Cl_5$ (CN 8) was refined and compared with that of $LiDy_2Cl_5$.

Likewise, Sharma et al. (1988) produced Nd metal by metallothermic reduction of Nd_2O_3 with calcium in a $CaCl_2$-NaCl melt with the overall reaction as $Nd_2O_3 + 3Ca = 3CaO + 2Nd$ at temperatures between 983 and 1063 K [81]. Nd was recovered from the salt melt by dissolution in the molten metal pool of either Nd-Zn or Nd-Fe. To obtain good metal yields, the concentration of $CaCl_2$ in their molten salt phase was kept to least at 70% and NaCl at 30% by weight (w/w). Percentage of Nd_2O_3 recovered as metal was found to be 95% in the case of Nd-Zn extraction. Nd metal was freed of zinc by vacuum distillation yielding as high as 99% purity. Also, in the case of Nd-Fe extraction, metal yields were reported to be about 95% with high quality near 98%. Both products could be directly used in the production of permanent magnets.

Luna et al. (2011) studied cerium recovery by Al-Mg alloy through metallothermic reduction of CeO_2 to obtain a main alloy of 96%Al-4%Ce [82]. Their resulting master alloy was for the grain refinement and modification of Al-Si alloys. By using a submerged powder injection technique, reagents were incorporated into the molten salt and yielded metallic product during the injection. Chemical and microstructural analyses by ICP and SEM confirmed Ce uptake in the bath (0 to 4% w/w) as CeO_2 was due to metallothermic reduction to the molten alloy.

In molten-salt electrolysis, REO is primarily dissolved in a molten bath and then electrolytically deposited as metal on the cathode while simultaneously evolving a gas (O_2, Cl_2 or F_2) at the anode [83, 84]:

$$\textit{Cathode}:\ 2La^{3+} + 6e^- \rightarrow 2La_{(l)} \qquad \text{Equation 2}$$

$$\textit{Anode}:\ 3O^{2-} \rightarrow 3/2O_{2\,(g)} + 6e^- \qquad \text{Equation 3}$$

$$\textit{Overall}:\ 2La^{3+} + 3O^{2-} \rightarrow 2La_{(l)} + 3/2O_{2\,(g)} \qquad \text{Equation 4}$$

The difference between the two processes is the source of electrons. In metallothermic reduction, they are supplied internally from the oxidizing metal and the process is run in batches; whereas, in molten-salt electrolysis, they are supplied externally through electrical circuits (see Fig. 11, where M represent the REE) and the process can be both batch and continuous. Both redox reactions show 3 electrons (e^-) for electroneutrality purposes. Examples of molten-salt electrolysis with application to REEs are presented in the following discussions.

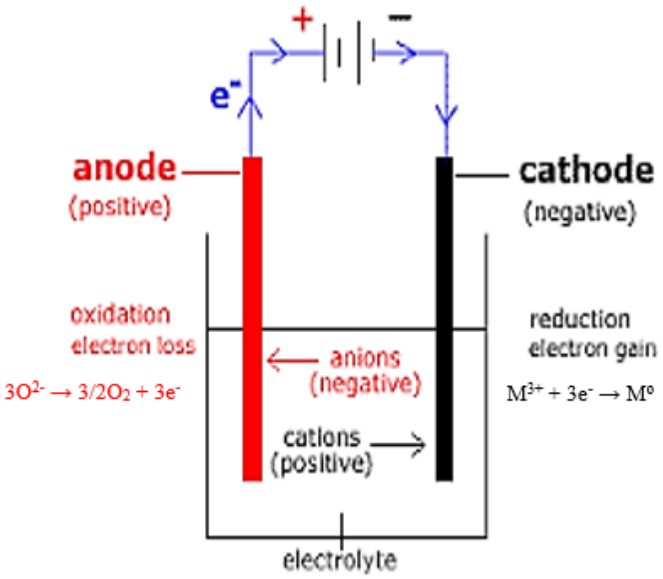

Figure 11: Schematic of the typical molten salt electrolysis process [85]

Morrice et al. (1967) prepared high-purity Nd, Pr and Dy from electrolysis of their oxides in a medium consisting of their respective REE fluorides and LiF [86]. The cells were operated at temperatures ranging from 1000-1100°C. Metals were electrodeposited in the molten state and collected as nodules after the bath was cooled to room temperature. Recoveries of 99.9 percent metal were obtained at current efficiencies of 83 percent.

Murphy et al. (1995) examined two techniques for making Nd metal. In the first, they electrowon Nd onto an Mg-Cd molten cathode from a chloride system of neodymium chloride ($NdCl_3$) and potassium chloride (KCl) at 650°C [87]. The Nd was deposited into the molten cathode until the Nd concentration reached 20 wt% at current efficiencies exceeding 80%. After the product was vacuum melted, the Nd purity was >99.9%. In the second system, Nd was electrowon at 1030°C from Nd_2O_3 dissolved in a molten fluoride electrolyte. They had current efficiencies up to 60% and obtained metal of 99.8% purity with impurities of oxygen and carbon.

Grebnev et al. (2007) conducted similar experiments and reported a mechanism for the production of Nd and Nd-Fe alloy from fluoride oxide systems [88]. They mapped current voltage dependencies of the processes against dissolving Nd_2O_3 in fluoride salts of lithium (Li), potassium (K) and sodium (Na) while optimizing process variables of current density, temperature and melt composition. A neodymium ingot of mass ranging from 150-200g were recovered with a current output of 80-82% in the laboratory electrolyzer which had a volume of 15 liters.

Electrochemical behavior of the systems LiF-NdF_3, LiF-Nd_2O_3 and LiF-NdF_3-Nd_2O_3 were investigated by Stefanidaki et al. (2001) with cyclic voltammetry [89]. They found NdF_3 reduced from LiF-NdF_3-Nd_2O_3 melts, via a three-electron reaction to Nd metal that was

deposited on the electrode substrate. Oxidation of oxide (O^{2-}) at anode to oxygen (O_2) was observed before the oxidation of fluoride (F^-) to fluorine (F_2).

Abbasalizadeh et al. (2015) studied the feasibility of the neodymium extraction from Nd–Fe–B magnet using a molten salt electrodeposition method [90]. For this study, aluminum chloride ($AlCl_3$) was added as a flux and graphite rods were used as electrodes in a mixture of LiCl–KCl–NaCl at their eutectic composition. $NdCl_3$ was produced at 802ºC as the result of chemical reaction of neodymium magnet with $AlCl_3$. Fe-free Nd deposition was reported in view of the proximity of the electrode potentials and aluminum as oxide phase was also detected using EDX and XRD analysis.

Shirayama et al. (2018) also conducted experiments to recycle Nd from Nd-Fe-B permanent magnets. Magnesium chloride ($MgCl_2$) molten salt at 1000°C was chosen as an extraction medium; hence, a side reaction would be chlorine gas formation [91]. For magnets that also contained Dy, recoveries of both REEs were found to be high with extraction ratios of Nd and Dy equaling 87 and 78 mass %, respectively.

For metallothermic reduction and molten-salt electrolysis, both chloride and fluoride baths are the most commonly used electrolytes and both processes make REE metal from REO. However, fluoride baths are being favored currently because current efficiencies are better due to the higher hygroscopicity of fluoride baths and divalent REE being metastable in chloride which forces electrochemical reactions to undergo two-step reduction processes at the minimum [92,93]. It is noted Sm^{2+} is an exception since it is also stable in fluoride systems [94, 95]. It is important to note that K and Na salts cannot be used because they would form metal rather than Nd [91-98]. Hence, such systems favor calciothermic conditions. This process can also be done

as a semi-continuous reduction in a large scale as proven by Carlson and Schmidt in preparation of yttrium by calcium reduction of rare earth fluoride in a pouring furnace [2, 99].

Conversely, hydrometallurgical processes have some drawbacks mostly by generating wastewater that can pose serious environmental problems depending on the type and quantity of contaminants present, particularly if it is acidic and corrosive. Furthermore, additional purification of the products may be needed, depending on the processes used. By comparison, pyrometallurgical processes also have drawbacks mostly by generating wastes such as slags and gases that pose environmental problems as well but are also dependent on the type and quantity of contaminants present. Further purification also depends on the processes used. Finally, the processes suffer from high energy requirements to obtain the high temperatures needed and the systems are often more corrosive making materials of construction special and costly [44, 98-102].

Thus, the research conducted for this study, aimed at developing both hydrometallurgical and pyrometallurgical processes to not only cheapen costs but to make them more efficient and applicable for recycling of secondary materials (i.e., REE magnets), not just the processing of primary minerals (i.e., ores and concentrates).

4. Theoretical Considerations

4.1. E_H-pH for Aqueous versus Potential (E)-pO^{2-} Molten Salt

Molten-salt electrolysis is similar to electrolysis in aqueous systems. For example, in both processes, current is charged between two electrodes through an ionized medium (molten bath/electrolyte) to deposit metal (typically by reduction of metallic cations) on the cathode and evolve gas (typically by oxidation of anions) on the anode. For aqueous systems, E_H-pH (Pourbaix) diagrams are used to determine thermodynamically the phase of the metal of interest and to predict materials corrosion resistance, particularly for the electrodes as well as materials of construction in contact with the solutions. Similarly, E-pO^{2-} diagrams have been designated for thermodynamically modeling molten salt systems. A concept introduced by Edeleanu et al. (1960) to predict the conditions that would allow electrolytic production of metal and to investigate its corrosion along with the electrodes and other materials [78,103-105].

A comparison of the two diagrams shows that pO^{2-} works opposite that of pH [106, 107] such that increasing one corresponds to decreasing the other. Furthermore, unlike Pourbaix diagrams for aqueous systems, E-pO^{2-} diagrams for molten salts have three thermodynamic items to contemplate: electrochemistry of the molten salt; the lack of a particular molten salt as a common medium interaction (solubility) between the metal and molten salt; and redox couple for establishing a Standard Electrode (V=0) [107]. Noticeably, each molten salt system is distinctive even at constant composition but different temperature. This does not seem to be a problem for aqueous systems because electrolysis is not operated at extreme elevated temperatures and, because the medium is always water, the Standard Hydrogen Electrode (SHE) is universally used.

To construct E-pO^{2-} diagrams, the free energies of formation (G^o_f) are usually used and not absolute free energies (G^o_{abs}). This is because G^o_f is zero by definition for all elements and the ΔG^o_f's for half-cell reactions become easy to determine along with their potential independence of the reactions (i.e., oxidation or reduction). E_H-pH and E-pO^{2-} diagrams are illustrated in Figure 12 and 13 for iron (Fe) assuming a unit activity for both Fe^{2+} and Fe^{3+}. In the E-pO^{2-} diagram in Figure 13, a molten bath of sodium nitrate ($NaNO_3$) at 327°C was used and the reference potential for NO_3^-/NO_2 redox couple was considered to be the reference electrode as labeled at V=0 and is referred to as the Standard Nitrogen Electrode (SNE). For the E_H-pH diagram in Figure 12, the temperature is set at 25°C; however, for simplicity, only Fe^{2+} and Fe^{3+} were considered as aqueous species [108]. In this case, the Standard Hydrogen Electrode (SHE) is the reference potential as previously noted (i.e., $E_H = E_{SHE} = 0$). Clearly and also as mentioned earlier, the roles of pO^{2-} and pH are reversed; otherwise, the E-pO^{2-} diagram for Fe in the $NaNO_3$ melt bears a strong resemblance to the E_H-pH diagram for the Fe aqueous system. The only other major difference is the appearance of the small predominance region for iron (II) oxide (FeO) in the E-pO^{2-} diagram.

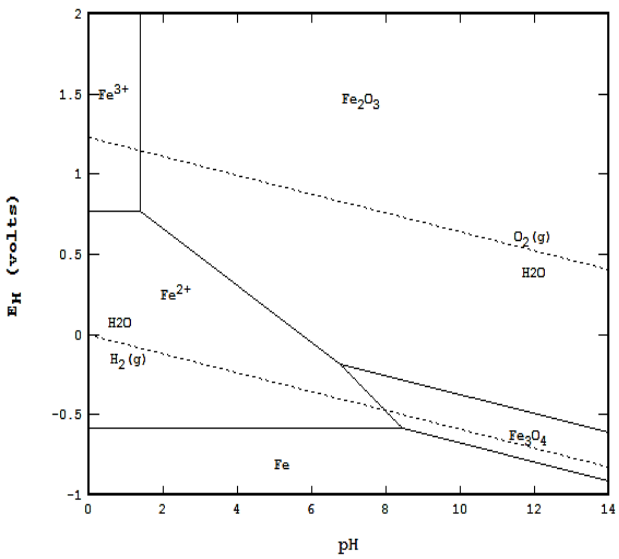

Figure 12: E_H-pH diagram for the aqueous system at 25°C

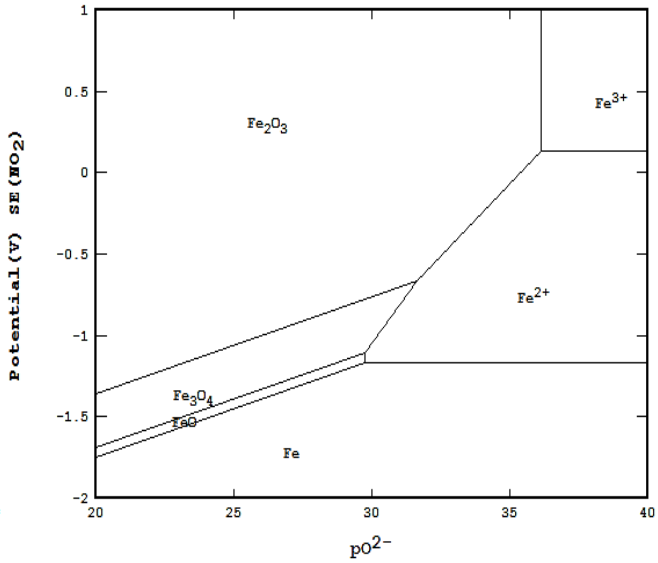

Figure 13: E-pO^{2-} diagram for Fe in $NaNO_3$ melt at 327°C

The electrode potential, E_H, for aqueous systems and E for molten salts, is relative and is defined as the difference between two combined half-cells, E_1- E_2. The second potential E_2 can be defined as the reference electrode. For aqueous systems, there is one conventional standard for the reference because the bath is always water. But for molten salt systems, each composition of the molten bath is different so the reference electrode can be a variable and may therefore be arbitrarily selected.

Under standard temperature and pressure conditions, and assuming a unit activity for H^+, the Hydrogen oxidation reaction shown in Equation 5 has a potential (E_{SHE}) = 0 at 25°C as well as at all other temperatures:

$$H_{2\,(g)} \leftrightarrow 2H^+ + 2e^- \qquad \text{Equation 5}$$

To satisfy this convention, free energies of formation (G^o_f) of each species in Equation 5 at all temperatures are defined to be zero. Because of that, it is not necessary to calculate E_2 from thermodynamics since it will also be zero. According to the Nernst equation, E_1 then becomes:

$$E_1 = \Delta E^o = E_1^o - E_{ref}^o (= 0V) = \frac{\Delta G_{rxn}^o}{n \times F} \qquad \text{Equation 6}$$

where n is the number of electrons, *F* is Faraday constant = 23.06055 kcal/ (V*EQ), and ΔG^o_{rxn} can be calculated from free energies of formation $G_{f,i}^o$ and their stoichiometric coefficients, v_i:

$$G_{rxn}^o = \Sigma(v_i \times G_{f,i}^o) \qquad \text{Equation 7}$$

Take, for instance, the equilibrium between the redox couple, Cu/Cu^{2+}:

$$Cu \leftrightarrow Cu^{2+} + 2e^- \qquad \text{Equation 8}$$

At 25°C, ΔG^o_{rxn} = 15.652 kcal, n = +2 for the number of electron, $E^o_{H\ Cu/Cu2+} = E_H^o$ = 0.33937 V. Notice that, regardless of the reaction direction (i.e., oxidation or reduction), the standard potential, E_H^o, will be the same value because, in the opposite direction, n = -2 and thereby yield the same result. Likewise, as indicated in Equation 6, the calculation for E^o_{ref} for SHE can be totally ignored (E^o_{SHE} = V = 0).

If a general reaction is considered between species A and B undergoing an electrochemical reaction in the presence of complexing ligands C and D in an aqueous system:

$$aA + bB + wH_2O = cC + dD + hH^+ + ne^- \qquad \text{Equation 9}$$

An E_H-pH equation can be derived from Nernst Equation under nonstandard state conditions:

$$\mathrm{E}_H = \mathrm{E}_1 = E_H^O + \frac{\ln(10)\,\mathrm{RT}}{(\mathrm{n} \times \mathrm{F})}\left[\log\left(\frac{\{\mathrm{C}\}^{\mathrm{c}}\{\mathrm{D}\}^{\mathrm{d}}}{\{\mathrm{A}\}^{\mathrm{a}}\{\mathrm{B}\}^{\mathrm{b}}}\right) - \mathrm{hpH}\right] \quad \text{where } \mathrm{E}_H^O = \frac{\Delta \mathrm{G}_{\mathrm{rxn}}^o}{(\mathrm{n} \times \mathrm{F})} \qquad \text{Equation 10}$$

Because, there is no standard reference electrode potential (E) for a molten salt system, it becomes necessary to compute the potential between two half cells for molten salt systems; similar to SHE for the aqueous system:

$$\Delta \mathrm{E}^{\mathrm{o}} = \mathrm{E}_1^{\mathrm{o}} - \mathrm{E}_2^{\mathrm{o}} = \frac{\Delta \mathrm{G}_{\mathrm{rxn}}^o}{\mathrm{n} \times \mathrm{F}} \qquad \text{Equation 11}$$

which is the same as Equation 6. Using LiCl as an example, the first and the second half-cells become:

$$\text{For } \mathrm{E}_1^{\mathrm{o}}: \ \mathrm{bB} \leftrightarrow \mathrm{aA} + \mathrm{ne}^-; \quad \mathrm{Li}_{(\mathrm{s})} \leftrightarrow \mathrm{Li}^+(\mathrm{melt}) + \mathrm{e}^- \qquad \text{Equation 12}$$

$$\text{For } \mathrm{E}_2^{\mathrm{o}}: \ \mathrm{dD} + \mathrm{ne}^- \leftrightarrow \mathrm{cC}; \quad 0.5\mathrm{Cl}_{2(\mathrm{g})} + \mathrm{e}^- \leftrightarrow \mathrm{Cl}^-(\mathrm{melt}) \qquad \text{Equation 13}$$

In this case, the first half-cell reaction is oxidation and the second is reduction with the second also being the reference reaction and therefore referred to as the Standard Chloride Electrode (SClE). It is important that the two reactions have the same number of electrons so that, when they are combined, the electrons are cancelled in the overall reaction as in Equation 14. If a general reaction is considered between species B and D undergoing an electrochemical reaction in the presence of complexing ligands A and C in a molten system:

$$\Delta \mathrm{E}^{\mathrm{o}} = \mathrm{E}_1^{\mathrm{o}} - \mathrm{E}_2^{\mathrm{o}}: \ \mathrm{bB} + \mathrm{dD} \leftrightarrow \mathrm{aA} + \mathrm{cC}\ (+\ \mathrm{oO}^{2-}); \quad \mathrm{Li}_{(\mathrm{s})} + 0.5\mathrm{Cl}_{2(\mathrm{g})} \leftrightarrow \mathrm{LiCl}(\mathrm{melt}) \qquad \text{Equation 14}$$

The Nernst Equation yields the E-pO^{2-} equation considering nonstandard state conditions and $E^o_2 = E^o_{ref} = 0V$ depending on the choice of the reference reaction which, in this case, is the SClE (see Eqn. 13):

$$E = E_1 = E^o + \frac{\ln(10)RT}{(n \times F)}\left[\log\left(\frac{\{A\}^a\{C\}^c}{\{B\}^b\{D\}^d}\right) - opO^{2-}\right] \quad \text{where } E^o = \frac{\Delta G^o_{rxn}}{(n \times F)} \qquad \text{Equation 15}$$

This also requires that the overall reaction be balanced and the number of electrons (n) needed in each half-cell reaction be used. Thus, in the LiCl example just illustrated, n=1. With $Cl_{2(g)}/Cl^-_{(melt)}$ as the reference, Table II shows the potentials E^o and E for Li and K at 420°C at a LiCl:KCl ratio of 42:58% molar composition of the eutectic (see Fig. 14). According to the calculation, Li^+ reduces to Li metal at E^o = -3.5922V with respect to the Cl_2/Cl^- reference potential. The overall reaction has a free energy change of -82.8386 kcal. However, when the composition is reduced from 100% to 42%, the potential becomes E = -3.6252V.

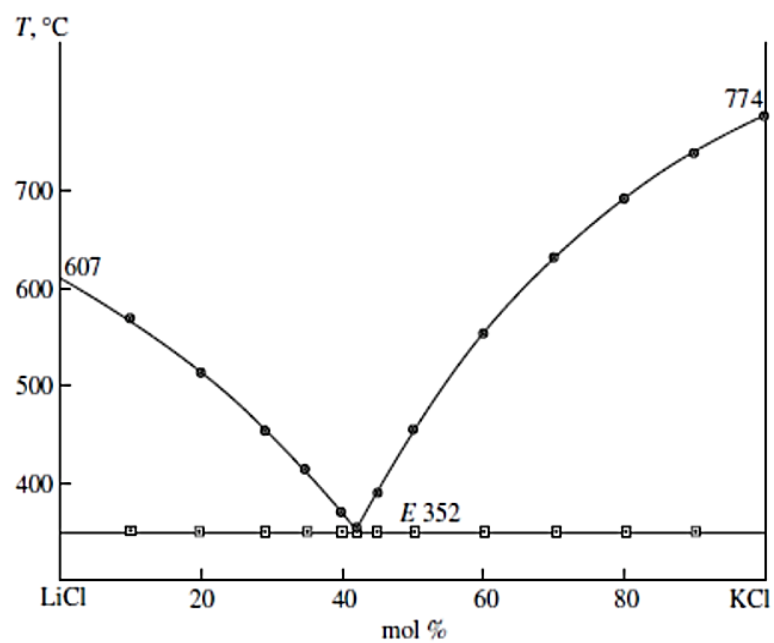

Figure 14: LiCl-KCl Binary System [109]

Likewise, K^+ reduces to $K_{(s)}$ at E^o = -3.7438V with respect to Cl_2/Cl^- reference. The overall reaction has a free energy change of -86.3346 kcal. However, when the composition is reduced from 100% to the eutectic 58 mol%, the potential becomes E = -3.7964V. Therefore, if electrolysis is done on this melt at a potential between these E-values such as -3.7V, Li metal will be produced, and K metal will not. Operating in this voltage range or "potential window" is critical to producing pure metal. It is noted that, as Li metal continues to be produced, the Li^+ concentration will decrease and the ratio will change to, for example, 30:70 mol% which will narrow the "potential window" by increasing the E-potential that K metal is produced and decreasing the E-potential that Li metal is produced. This may therefore slow Li metal production and potentially prevent it unless the operating temperature is increased (i.e., at 30:70 mol%, the temperature must be above 450°C for the bath to be completely molten. Thus, controlling the bath composition and temperature becomes critical for economic performance and additionally illustrates the importance of continuous processing to maintain concentrations [110].

Table II: Potentials E^o and E for Li and K with LiCl:KCl ratio of 58:42% at 420°C.

Half-Cells	Half-Cell Reaction	n (e-)	Combined Reaction	ΔG^o_{rex} (kcal)	E^o (V)	% Composition (eutectic)	E (V)
$Cl^-/Cl_{2(g)}$ (Ref)	$0.5Cl_{2(g)} + e^- = Cl^-$	-1	-	-	-	-	-
$Li^+_{(melt)}/Li_{(m)}$	$Li = Li^+ + e^-$	1	$Li + 0.5Cl_{2(g)} = LiCl$	-82.8386	-3.5922	42%	-3.6252
$K^+_{(melt)}/K_{(m)}$	$K = K^+ + e^-$	1	$K + 0.5Cl_{2(g)} = KCl$	-86.3346	-3.7438	58%	-3.7964
$\Delta E = E_1(Li/Li^+) - E_2(K/K^+)$		1	$Li + KCl = LiCl + K$	3.4960	0.1516		0.1712

4.2. Thermodynamic Consideration of Molten Salt

High temperatures are needed to melt salts to provide an inert molten bath that allows for the solubilization of reactive metal salts so that an electrolytic process can be used to produce metal [107]. This cannot be done in aqueous solutions because the water bath will become reactive forming hydrogen gas before the metal can be produced. Since reactive metal salts like rare earth oxides have solubilities that increase with increasing temperatures in molten salts, thermodynamic considerations of the interaction between the metal oxide and molten salt at elevated temperature is essential to accomplish effective electrolysis of the rare earths [18].

With that in mind, lower melting temperatures of a molten bath can be obtained by mixing two or more salts in an appropriate ratio. As can be seen from Figure 14, the phase diagram of LiCl-KCl shows the eutectic composition of KCl (58 mole%) and LiCl (42%) has a melting temperature of only 352°C which is significantly below the melting temperatures of the pure materials: LiCl at 607°C and KCl at 774°C. This makes the molten salt process economically more viable and easier to control [109, 111, 112].

Commonly used thermodynamic databases such as HSC (2002) and Kubaschewski (1965) list solid and liquid phases in a single table but are separated by individual melting temperatures [113, 114]. For mixtures with lower melting temperatures, it becomes necessary to create data sets for only the liquid phase as illustrated in Table III regarding entropy (*S*), enthalpy (*H*) and coefficient data (a, b, c and d) for calculating heat capacity (*Cp*): $\boldsymbol{Cp = a + 1\times10^{3}b + 1\times10^{-5}c + 1\times10^{6}d}$.

Table III: Thermodynamic Data of LiCl and KCl from HSC (2002) Database and Recreated Data for the Liquid Phases [113]

Species	*S* (cal)	*H* (kcal)	Phase	Start Temp (*K*)	*a*	*b*	*c*	*d*
LiCl (l)	17.16996	-93.9482	L	298.15	15.105	0.0	0.0	0.0
KCl (l)	21.23224	-100.522	L	298.15	17.208	0.0	0.0	0.0

4.3. Equilibrium Potential in Molten Salt Systems

When an equilibrium potential is polarized, the sign and magnitude of polarization $\eta = E_{apply} - E$ determines not only the direction of the reaction but also its rate. Positive η (overvoltage) promotes oxidation and negative η (undervoltage) promotes reduction. Generally, a large magnitude of η yields higher rate if the reaction is under chemical control; however, if it is under mass-transport control, a limiting current will be reached, and rate becomes constant.

For two half-cells without external power supply, the half cells will polarize the other. The half-cell with the higher E will have an undervoltage ($-\eta$) and will be pushed into reduction. Likewise, the half-cell with the lower E will have an overvoltage ($+\eta$) and will be pushed into oxidation. On the order hand, when an external power supply is used, a voltage between the two half-cells must be applied to produce the metal with the higher E. According to Table III, as already discussed and now illustrated in Figure 15, the electrolysis of Li metal from LiCl-KCl, the decomposition of LiCl occurs at or below -3.6252V ($E_{Li/LiCl}$). By comparison, the decomposition of KCl to K metal occurs at or below -3.7964V ($E_{K/KCl}$). To reduce only Li from LiCl-KCl, the cathode voltage to be applied must be in the “potential window” between those two values as shown by the dashed line in Figure 15.

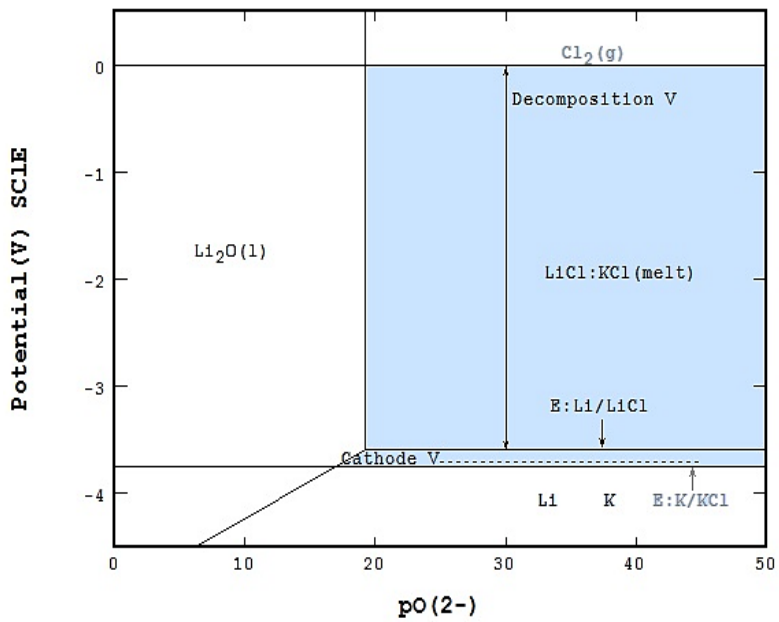

Figure 15: Potential (E)-pO^{2-} diagram of Li in LiCl-KCl melt

This clearly illustrates that the applied potential would be close to -3.7V as already mentioned. Thus, this potential is an undervoltage with respect to Li metal so Li^+ is reduced as shown in Figure 16; furthermore, it is an overvoltage with respect to K metal which is not stable so K^+ becomes favored.

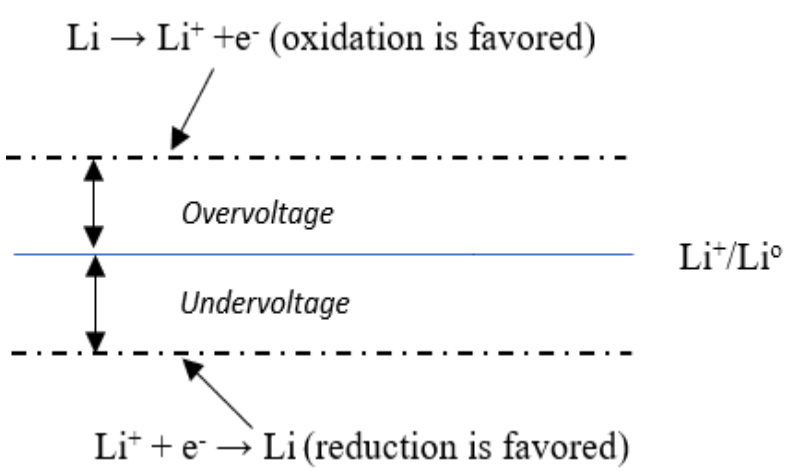

Figure 16: Over and undervoltage potential of Li

4.4. Determination of Free Energy of O^{2-} from a Molten System

The free energy value of O^{2-} (G^o_{O2-}) in molten salt varies not only with temperature and composition of the melt, but also the half-cell to be defined as the reference electrode. It can be calculated by combining free energies of formation from the metal-oxide and metal-salt as well as the selected reference. Table IV shows results applied to a LiCl:KCl melt with two different redox couples selected as the reference, namely $Cl_{2(g)}/Cl^-_{(melt)}$ as System 1 and $K^+_{(melt)}/K_{(s)}$ as System 2. For Systems 1 and 2, calculations show G^o_{O2-} is 103.95 kcal and -53.17 kcal, respectively. The results concur with the literature but are different because the references for the two systems are different.

Table IV: Free Energy of O^{2-} as Determined at 800°C for Two Different Reference Reactions.

Species	Equation #	G^o (kcal)	Formation Reaction
1. Cl^- Anion Reference: KCl Melt [115]			
K_2O	A1	-53.710	$2K + 0.5O_2 = 2K^+ + O^{2-}$
KCl	A2	-78.830	$K + 0.5Cl_2 = K^+ + Cl^-$
Cl^- (Ref)	A3	0.000	$0.5Cl_2 + e^- = Cl^-$
O^{2-}	A4=A1-2(A2-A3)	103.950	$0.5O_2 + 2e^- = O^{2-}$
2. K^+ Cation Reference: KCl Melt [115]			
K_2O	D1	-53.710	$2K + 0.5O_2 = 2K^+ + O^{2-}$
KCl	D2	-78.830	$K + 0.5Cl_2 = K^+ + Cl^-$
Cl^-	D3=D2-2(D2)	-78.830	$0.5Cl_2 + e^- = Cl^-$
K^+ (Ref)	D4	0.000	$K = K^+ + e^-$
O^{2-}	D5=D1-2(D2-D3-D4)	-53.710	$0.5O_2 + 2e^- = O^{2-}$

4.5. Mass Transport of Rare Earths

Mass transport of species involved in electrowinning is an essential counterpart to charge transfer and was considered in this study. This is because charge transfer from the bulk solution (molten bath) causes the occurrence of either oxidation or reduction reaction depending on the electrode. Mass transport is associated with three processes: diffusion, migration and convection. However, with respect to this work, convection was not considered because experiments could not be stirred; hence, there were no association with any external mechanical energy [116].

4.5.1. Diffusion

The dissolution of solute in a solvent is important when it comes to electrochemical extraction. Because, as the solute (Nd_2O_3) is consumed and the product (Nd metal) is formed at the cathodic electrode, concentration gradients develop around the electrode up to the bulk of the solution, meaning that reactants move towards the electrode surface, metal is deposited, and by-product leave the interfacial region. Fick's law is therefore applicable [117,118].

$$J_O = -D_O \frac{\partial c}{\partial x} \qquad \text{Equation 16}$$

where, *Jo* represents the diffusion flux in weight per unit area per unit time, *Do* is the diffusion coefficient in area per unit time, and $\frac{\partial c}{\partial x}$ is the rate of change of concentration in the direction *x* with the minus sign indicating the flow is from higher to lower concentration.

For neodymium oxide, diffusion and succeeding electrode reactions depend on the complex ions forming in the melt. In fluoride systems, solubility of the oxide in the bath is an important parameter. Although molten fluorides have a low oxide solubility, with the exemption of cryolite (Na_3AlF_6), which has an elevated solubility for alumina near 10 wt.%, temperature as

well as the addition and amount of a third fluoride salt with the same REE can also affect the solubility of the oxide [84,86,99,119].

4.5.2. Migration

Migration is a result of inner potential gradient in the solution proximate to the electrode and, by that, mass transport occurs [120]. This is because charge transfer automatically changes the charge balance of the chemical species close to the electrode. Figure 17 illustrates and characterizes the layers in the molten bath which are also referred to as electrical double layers. This was developed to account for the composition of the solution close to a charged metal surface in terms of excess ionic and non-ionic species without faradic current [121, 122].

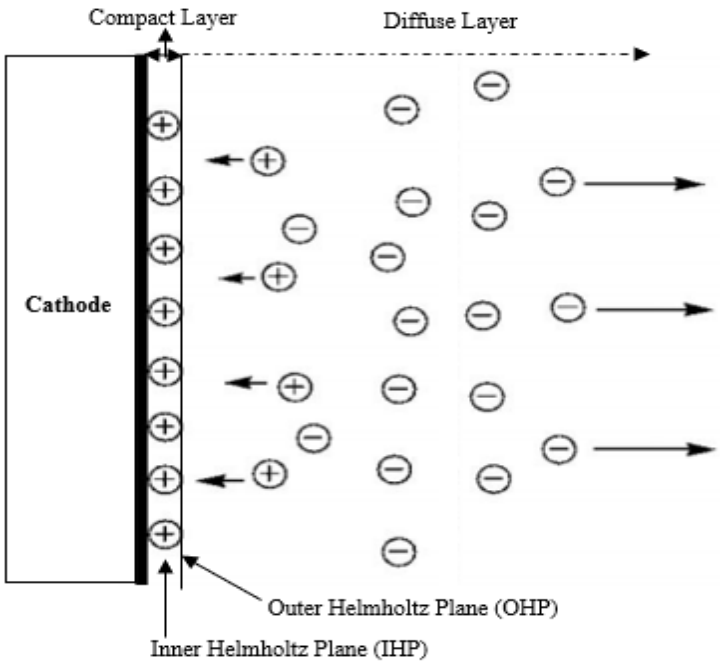

Figure 17: The electrical double layer [123]

In the electrolyte, there is a solid-liquid interface reaction when the metal is immersed and polarized as a cathode. This is because both the metal cathode and the electrolyte have

different energy levels which leads to tension at the interface once they are in close contact [116]. Basically, the cathode carries a negative charge at the surface upon contact with the electrolyte which is caused by its high dielectric constant [124]. The electrolyte also contains ions of dissolved salts with cations being attracted to and anions being repelled from the negative surface charge on the cathode. The cations will gather at the cathode surface in an orderly manner and form an immovable layer called the Stern layer (see Fig. 17). The Stern layer is made up of the inner Helmholtz plane (IHP) and the outer Helmholtz plane (OHP) such that the IHP is the region of adsorbed cations and the OHP constitutes the region where anions first appear [123, 125]. In essence, the cations help to neutralize the negative charge of the cathode which is caused by electrons flowing out from the cathode to the anode [126].

5. Potential (E)-pO^{2-} Diagrams

5.1. Neodymium

For this research, a combination of lithium fluoride (LiF) and calcium fluoride (CaF_2) was used as the molten bath to solubilize various quantities of neodymium fluoride (NdF_3) and neodymium oxide (Nd_2O_3) as reported by Shiguan et al. [94, 127] where the Nd ions were reduced to metal on a molybdenum (Mo) electrode. E-pO^{2-} diagrams were modeled and constructed by calculating and modelling the chemical equilibria based on all of the concepts discussed earlier in Chapter 4 using the computer program, Stability Calculations for Aqueous Systems (StabCal) [128] which was developed by Dr. Hsin-Hsiung Huang, a professor of Metallurgical and Materials Engineering at Montana Technological University. StabCal was first released in 1989. Since the released time, StabCal has experienced frequent reformations to accommodate different computation and operating systems but also to accommodate technological updates. StabCal uses numerous Gibbs free energy databases including but not limited to NBS, MINTEQ (visual minteq), Naumov (Russia), Kubaschewski, HSC and others. Lately, the software has been adapted to do thermodynamic calculations for non-aqueous systems and were used in this dissertation.

The HSC thermodynamic database was used in this study as the source for G^o values at a temperature of 1050° C [113]. StabCal was used to convert them to G^o_{ref} and perform the actual E-pO^{2-} diagram calculations. The melt was assumed to be 72, 18 and 10 %mole for LiF, CaF_2 and NdF_3, respectively. As an obligation, the melt should encompass one anion (i.e., F^-) with the anion also requiring a second species (i.e., $F_{2\,(g)}$) to make a half-cell reaction: $2F^- = F_2 + 2e^-$. In addition, fluorine (F) was chosen as the main component for this work. Furthermore, to make F^-

$_{(melt)}/F_{2\,(g)}$ the reference half-cell, the $G^o_{F2\,(g)}$ and G^o_{F-} were adjusted to be zero by convention so that both ΔG and E (V= 0) of their half-cell reaction would also be zero.

For the calcium (Ca) and lithium (Li) cations, the mole fraction of each of the cations were calculated such that their sum was 100 %mole fraction. In this case study, %mole fractions for Ca^{2+} and Li^+ were set at 20 and 80, respectively. Because each cation is also in equilibrium with its metal, oxide and fluoride, three half-cell reactions can be envisioned for each. Ca was used as the first component and Li was used as the second component. Species CaF_2 and CaO as well as and LiF and Li_2O were therefore considered as cation-anion and cation-oxide pairs, respectively. All of this allows G^o values of various species to be calculated with respect to the $F^-/F_{2\,(g)}$ reference herein referred to as Standard Fluoride Electrode (SFE).

The system components (Nd, F, Ca, O and Li) and various species along with their G^o values and activities were calculated (see Table V). An additional system components of carbon (C) was considered because graphite electrodes were employed as the anodes. Consequently, carbon monoxide (CO) and carbon dioxide (CO_2) were included so the diagram could depict regions of stability of all the various phases at unit activity in equilibrium with their respective dissociated ions.

5.2. Other Rare Earths

Similarly, using the same principle, the E-pO^{2-} diagram for some of the other REEs were constructed. HSC thermodynamic database was also used as the source for G^o values at a temperature of 1050° C. The percentage mole composition of lithium fluoride (LiF) and calcium fluoride (CaF_2) used to solubilize rare earth fluoride and other condition used in the construction of the Nd diagram were the same for the other REEs.

5.3. Results and Discussions

5.3.1. Neodymium

With the various conditions selected, Table V was constructed to demonstrate the G^o values at 1050°C for all the relevant species with respect to SFE ($F^-/F_{2\,(g)}$). Fluoride (F^-) and electrons (e^-) are both considered ionic species in the molten bath and the G^o of F^- is 0 kcal because the SFE was chosen to be the reference electrode. The resulting E-pO^{2-} diagram of Nd_2O_3 in 72 %mole LiF, 18 %mole CaF_2, and 10 %mole NdF_3 is presented in Figure 18(a)-(b).

Table V: Free Energies for Species Involved in Nd Fused-Salt Electrolysis at 1050°C Referenced against the SFE [113]

Species	G^o (kcal)	Species	G^o (kcal)	Species	G^o (kcal)
e^-	0.0	$CO_{2(g)}$	-94.6837	Nd	0.0
F^-	0.0	Li	0.0	$Nd_{(l)}$	-9.3042E-09
$F_{2(g)}$	0.0	LiF	-118.2533	Nd^{3+}	-325.1430
$O_{2(g)}$	0.0	Li_2O	-100.6708	$NdOF_{(l)}$	-230.9062
O^{2-}	133.0750	Ca	0.0	Nd_2O_3	-343.3114
C (graphite)	0.0	CaF_2 (fluorite)	-240.2955	$Nd_2O_{3(s)}$	-342.8370
$CO_{(g)}$	-55.6861	CaO	-118.2632		

Figure 18 shows the y-axis as the potential (E) referenced against SFE (V=0) and the x-axis as the activity of oxide ion (pO^{2-} = -log [O^{2-}]) which epitomizes the acidity and basicity of the system. Assuming a basic chemical is added to the system, it will upsurge the concentration of O^{2-} and subsequently decrease the value of pO^{2-}. This clearly means the pO^{2-} will shift to the left on the diagram which is opposite that of E_H-pH diagrams when base is added. Also, basicity

determines the affinity a species has for an electron or anion, how soluble the salts are, the stability of complex ions, and the quantity of cations in the melt. From this, it can be said that cations with the least affinity for electrons are considered to be most basic, and those with the greatest affinity are considered the least basic.

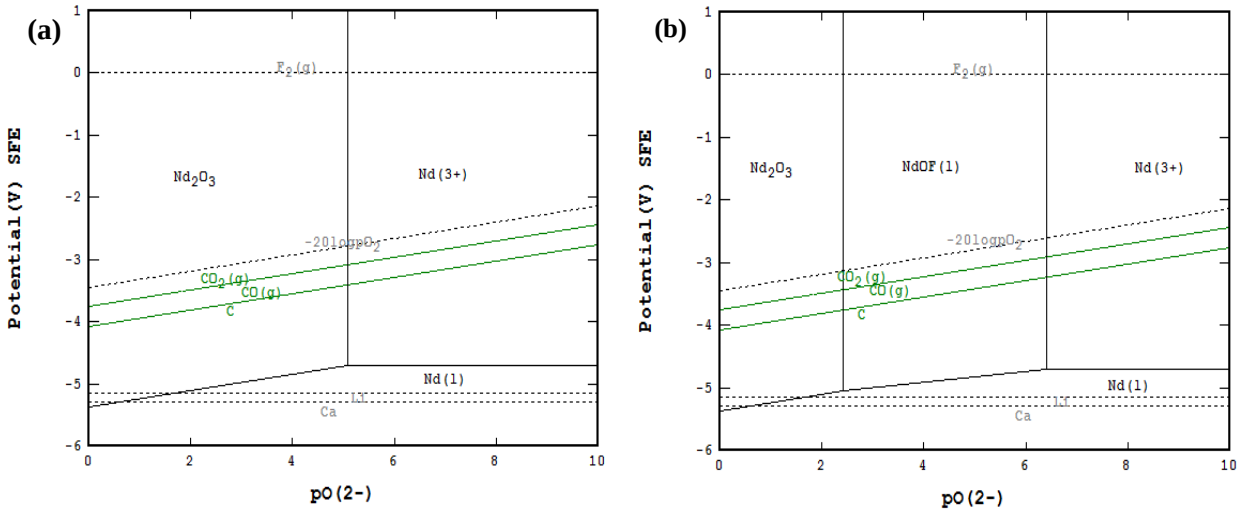

Figure 18(a)-(b): E-pO^{2-} Diagram of Nd in NdF_3-CaF_2-LiF Melt including C as a Component (a) with and (b) without the NdOF phase

The distribution of the species on the diagram depends on the potential and concentration of O^{2-}. From Figure 18(b), the horizontal line at -4.71V represents the equilibrium between Nd^{3+} and $Nd_{(l)}$ and the vertical line at $pO^{2-} = 6.41$ represents the equilibrium between Nd^{3+} and NdOF. Nd^{3+} is stable under oxidizing (SFE > -4.71V) and acidic ($pO^{2-} > 6.41$) conditions. It will reduce to $Nd_{(l)}$ if the potentials become reducing (SFE < -4.71V):

$$Nd^{3+} + 3e^- = Nd_{(l)} \qquad \text{Equation 17}$$

It is important to avoid conditions becoming basic ($pO^{2-} < 2.4$ from Fig. 18(b)) in order to maximize electrolysis according to Equation 17 and thereby avoid Nd_2O_3 precipitation:

$$2Nd^{3+} + 3O^{2-} = Nd_2O_3 \qquad \text{Equation 18}$$

because electrolysis works best for the reduction of cations similar to Equation 17 and not neutral and anionic species. Theoretically, Nd_2O_3 can reduce to $Nd_{(l)}$ if the E and pO^{2-} conditions fall below the diagonal line shown in Figure 18(b):

$$Nd_2O_3 + 6e^- = 2Nd_{(l)} + 3O^{2-} \qquad \text{Equation 19}$$

However, this reaction is inefficient because the species is neutral and, if present, could settle to the bottom of the electrowinning cell.

On the other hand, if it were to form, it would likely dissolve in the presence of NdF_3 and excess F^- to form neodymium oxyfluoride (NdOF) [88, 93-97, 127-131]:

$$1/3Nd_2O_3 + 1/3NdF_3 = NdOF \qquad \text{Equation 20}$$

$$Nd_2O_3 + 2F^- = 2NdOF + O^{2-} \qquad \text{Equation 21}$$

The stability region of NdOF is illustrated in Fig. 18(b). It is known to dissolve into NdO^+ and F^- and also react in excess F^- to form $NdOF_5^{4-}$:

$$NdOF = NdO^+ + F^- \qquad \text{Equation 22}$$

$$NdOF + 4F^- = NdOF_5^{4-} \qquad \text{Equation 23}$$

Likewise, NdO^+ can reduce to $Nd_{(l)}$ at the cathode and $NdOF_5^{4-}$ can oxidize at the anode:

$$NdO^+ + 3e^- = Nd_{(l)} + O^{2-} \qquad \text{Equation 24}$$

$$NdOF_5^{4-} = NdO^+ + 5/2\ F_{2(g)} + 5e^- \qquad \text{Equation 25}$$

The conditions for Equations 22 and 24 need to be slightly acidic such that, according to Figure 18(b), $2.4 < pO^{2-} < 6.41$. Likewise, Equations 23 and 25 are acidic so $pO^{2-} > 6.41$.

Finally, it is noted that NdF_6^{3-} can also form by reacting NdF_3 with excess F^- which, in regard to Fig. 18(a)-(b), can be shown to co-exist with Nd^{3+}:

$$NdF_3 + 3F^- = NdF_6^{3-} \qquad \text{Equation 26}$$

Resulting NdF_6^{3-} can also react at the anode by oxidation to form Nd^{3+}:

$$NdF_6^{3-} = Nd^{3+} + 3F_{2(g)} + 6e^- \qquad \text{Equation 27}$$

It is noted that the condition for this reaction also needs to be acidic such that, according to Figure 18(b), the $pO^{2-} > 6.41$. In addition, the resulting Nd^{3+} can be reduced to metal according to Equation 17.

From the study, it can be said that Equations 17 and 24 occur at the cathode to produce metal. At the anode, primarily, the potential should be lower than 0V SFE to minimize $F_{2(g)}$ formation and maximize F^- stability. Also, reactions that occur at the anode are Equations 25 and 27 as well as any that lead to the formation of at least one of these gases [93]:

$$2F^- = F_{2(g)} + 2e^- \qquad \text{Equation 28}$$

$$O^{2-} = 1/2O_{2(g)} + 2e^- \qquad \text{Equation 29}$$

$$C + O^{2-} = CO_{(g)} + 2e^- \qquad \text{Equation 30}$$

$$C + 2O^{2-} = CO_{2(g)} + 4e^- \qquad \text{Equation 31}$$

As long as potentials are held below the SFE reaction, Equation 28 will not occur; however, oxide could react to form oxygen ($O_{2(g)}$) per Equation 29 or with the C electrode to form $CO_{(g)}$ and $CO_{2(g)}$ Equations 30 and 31, respectively.

It is also possible for back reactions between $Nd_{(l)}$ metal and these gases to occur. Examples are shown in Equations 32 and 33 with $CO_{2(g)}$:

$$2Nd_{(l)} + 3CO_{2(g)} + NdF_3 = 3NdOF + 3CO_{(g)} \qquad \text{Equation 32}$$

$$3CO_{2(g)} + 2Nd_{(l)} = Nd_2O_3 + 3CO_{(g)} \qquad \text{Equation 33}$$

Because the $Nd_{(l)}$ metal is molten, it may form and drip from the cathode into the cell. In fact, these reactions are known as one of the primary mechanisms of current inefficiency [132, 133].

Finally, with Li^+ and Ca^{2+} also in the melt, it will be important to avoid their reduction to metal in order to maintain as high purity of $Nd_{(l)}$ as possible:

$$Li^+ + e^- = Li_{(l)} \qquad \text{Equation 34}$$

$$Ca^{2+} + 2e^- = Ca_{(l)} \qquad \text{Equation 35}$$

In this regard, as shown in Figure 18, the dashed horizontal line at -5.20V SFE denotes the equilibrium for Equation 34. Equation 35 occurs at a slightly lower potential of -5.34V SFE. Thus, only Nd will form if the cathode voltage is held in the potential window between -4.71 and -5.2V SFE.

Equations 20-25 for the production of Nd are most likely to occur in this study because of the addition of the oxide. The equilibrium potential of formation for oxygen can be varied depending on the activity of the oxide ion (O^{2-}) and will be close to -2.62V at pO^{2-} 6.41 and -2.13V at pO^{2-} 10. Overall, the cathode potential will allow only $Nd_{(l)}$ to form (likely in accordance with Equation 24) and the anode potential will yield $O_{2(g)}$ (Equation 29). It is important to note that the anode potential is significantly below 0V SFE and will therefore allow F^- to remain stable throughout the process and thereby prevent Equation 28 from occurring.

5.4. Other Rare Earths

All REEs exist in the +3 oxidation state but can have others: Ce (+4), Pr (+4), Tb (+4), Sm (+2), Eu (+2), and Yb (+2). In Chapter 1, it was noted that REEs are very similar to one another in their chemical properties. This similarity is exhibited in their E-pO^{2-} diagrams (see Fig. 19-22) as determined from their species and corresponding free energies (see Tables VI-IX), respectively. In general, Ce and Pr have similar diagrams (Fig. 19 and 20) because they both have oxidation states of +3 and +4; whereas, Eu is different (Fig. 21) because it has oxidation

states of +2 and +3. On the other hand, Dy (Fig. 22) is same as Nd (Fig. 18) because they only have the +3 oxidation state.

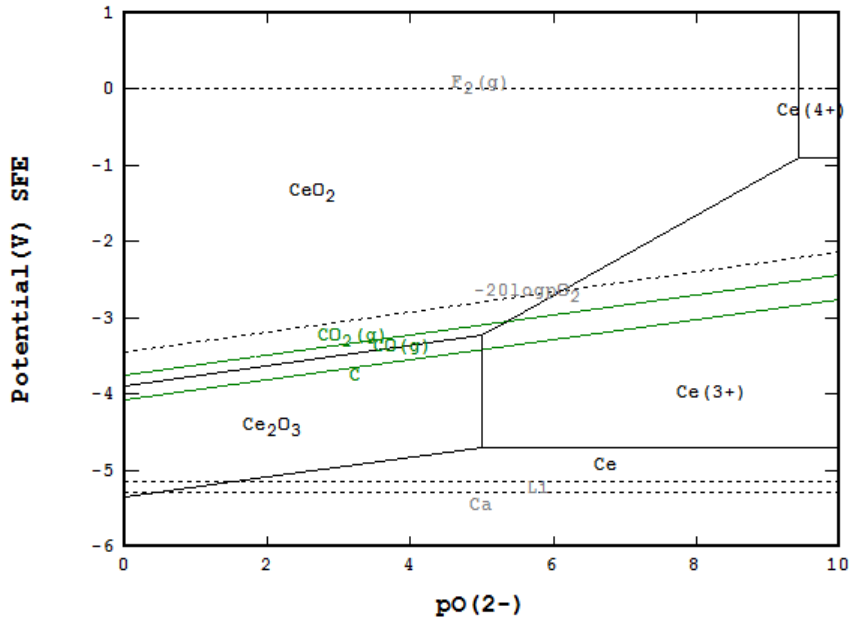

Figure 19: E-pO^{2-} Diagram of Ce in CeF_3-CaF_2-LiF Melt including C as a Component

Table VI: Free Energies for Species Involved in Ce Fused-Salt Electrolysis at 1050ºC Referenced against the SFE [113]

Species	Gº (kcal)	Species	Gº (kcal)	Species	Gº (kcal)
e^-	0.0	$CO_{2(g)}$	-94.6837	CaO	-118.2632
F^-	0.0	Li	0.0	Ce^{3+}	-324.9986
$F_{2(g)}$	0.0	LiF	-118.2533	Ce^{4+}	-345.9348
$O_{2(g)}$	0.0	Li_2O	-100.6708	CeO_2	-194.1052
O^{2-}	133.0750	Ca	0.0	Ce_2O_3	-341.7103
C (graphite)	0.0	CaF_2 (fluorite)	-240.2955	Ce	0.0
$CO_{(g)}$	-54.6861				

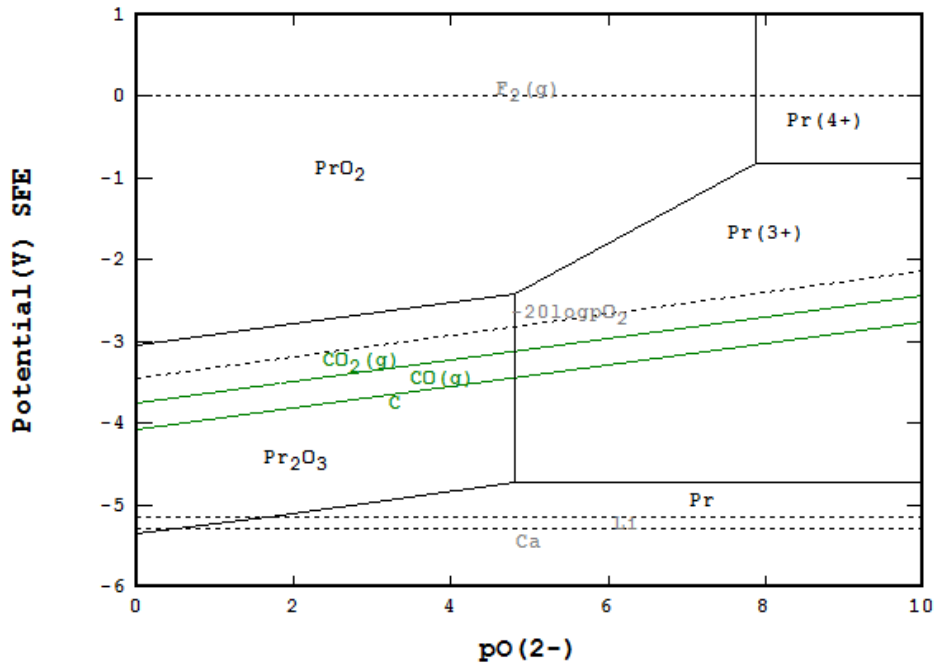

Figure 20: E-pO^{2-} Diagram of Pr in PrF$_3$-CaF$_2$-LiF Melt including C as a Component

Table VII: Free Energies for Species Involved in Pr Fused-Salt Electrolysis at 1050ºC Referenced against the SFE [113]

Species	Gº (kcal)	Species	Gº (kcal)	Species	Gº (kcal)
e^-	0.0	$CO_{2(g)}$	-94.6837	CaO	-118.2632
F^-	0.0	Li	0.0	Pr^{3+}	-327.1462
$F_{2(g)}$	0.0	LiF	-118.2533	Pr^{4+}	-345.8442
$O_{2(g)}$	0.0	Li_2O	-100.6708	PrO_2	-174.9786
O^{2-}	133.0750	Ca	0.0	Pr_2O_3	-342.5845
C (graphite)	0.0	CaF_2 (fluorite)	-240.2955	Pr	0.0
$CO_{(g)}$	-54.6861				

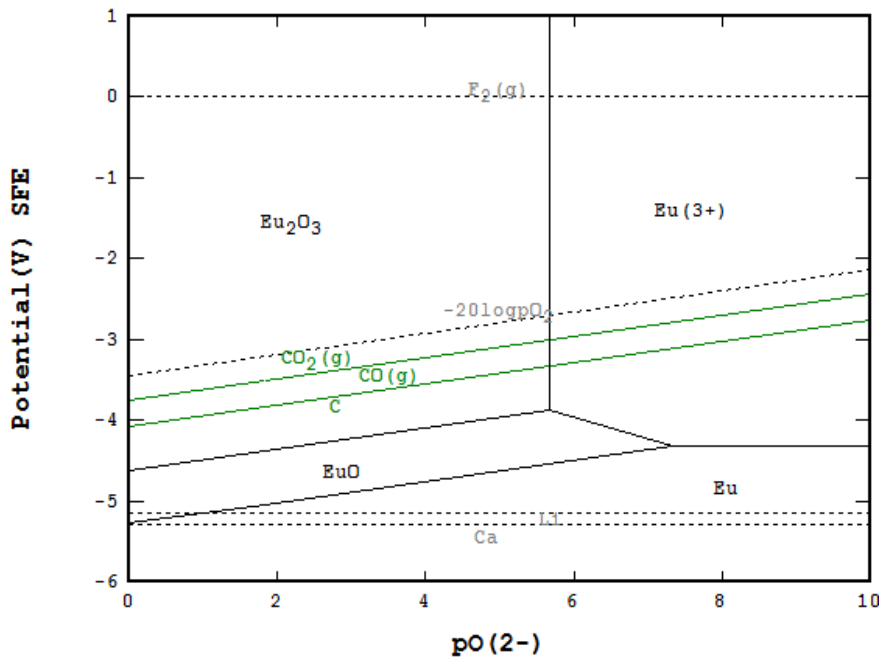

Figure 21: E-pO^{2-} Diagram of Eu in EuF$_3$-CaF$_2$-LiF Melt including C as a Component

Table VIII: Free Energies for Species Involved in Eu Fused-Salt Electrolysis at 1050ºC Referenced against the SFE [113]

Species	Gº (kcal)	Species	Gº (kcal)	Species	Gº (kcal)
e^-	0.0	$CO_{2(g)}$	-94.6837	CaO	-118.2632
F^-	0.0	Li	0.0	Eu_2O_3 (cubic)	-299.3031
$F_{2(g)}$	0.0	LiF	-118.2533	Eu_2O_3 (monoclinic)	-301.1689
$O_{2(g)}$	0.0	Li_2O	-100.6708	Eu^{3+}	-298.7506
O^{2-}	133.0750	Ca	0.0	EuO	-110.5061
C (graphite)	0.0	CaF_2 (fluorite)	-240.2955	Eu	0.0
$CO_{(g)}$	-54.6861				

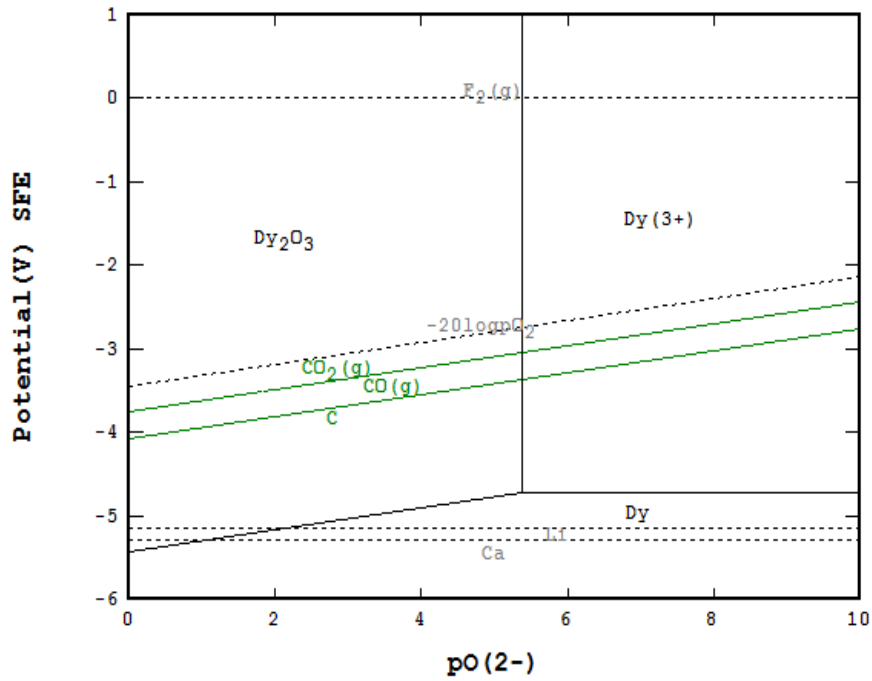

Figure 22: E-pO^{2-} Diagram of Dy in DyF_3-CaF_2-LiF Melt including C as a Component

Table IX: Free Energies for Species Involved in Dy Fused-Salt Electrolysis at 1050ºC Referenced against the SFE [113]

Species	Gº (kcal)	Species	Gº (kcal)	Species	Gº (kcal)
e^-	0.0	$CO_{2(g)}$	-94.6837	CaF_2 (fluorite)	-240.2955
F^-	0.0	Li	0.0	CaO	-118.2632
$F_{2(g)}$	0.0	LiF	-118.2533	Dy_2O_3 (monoclinic)	-3530751
$O_{2(g)}$	0.0	Li_2O	-100.6708	Dy^{3+}	-327.2459
O^{2-}	133.0750	Ca	0.0	DyO	-33.2035
C (graphite)	0.0	$CO_{(g)}$	-54.6861	Dy	0.0

As already noted, according to Figures 19 and 20, Ce and Pr have comparable diagrams because they both have +3 and +4 oxidation states. The respective potentials at which Li and Ca will form are shown as dashed lines on both diagrams at -5.20V and -5.34V. Some of the

important differences is the potential window of these elements and the pO^{2-} values at which there is equilibrium between the RO_2 and R^{4+} as well as R_2O_3 and R^{3+} (where R = Ce and Pr). More importantly, because the dashed lines are shown to overlap regions of Ce and Pr elemental stability, their formation using fused-salt electrolysis is possible. With respect to the potential window, Ce is 0.46V above Li and Pr is 0.42V above. For Ce, the $pO^{2-} > 5.0$ and, for Pr, the $pO^{2-} > 4.81$. The equilibria between the PrO_2/Pr^{4+} is at pO^{2-} 7.88, Pr_2O_3/Pr^{3+} at 4.81, CeO_2/Ce^{4+} at 9.43, and Ce_2O_3/Ce^{3+} at 5.0.

With oxidation states of +2 and +3, europium reveals minor differences with its E-pO^{2-} diagrams (Fig. 21) compared to Nd (+3 only) as well as Ce and Pr (both +3 and +4). As with the other diagrams, the Li and Ca potentials are also shown as dashed lines. In this case, the potential window is 0.8V but must be at $pO^{2-} > 7.3$ to avoid EuO formation. By comparison, the E-pO^{2-} for Dy is shown in Figure 22. This diagram clearly resembles Nd in Figure 18(a). It has a potential window that is 0.45V above but, in this case, the pO^{2-} must be > 5.3.

All of these diagrams were constructed using pure thermodynamics route to identify stable species that might exist within the molten salt assuming unit activity for each of the phases. These diagrams also thermodynamically describe the electrochemical system predicting reaction conditions essential to electrolytically produce REE-metal. Considering all diagrams, it can also be said that the potentials at which Li and Ca can be electrowon remain the same for all the REEs and at a potential of 4.9V all these REEs can be electrowon in a fluoride bath. Reactions similar to those described for Nd would be expected, particularly if species like NdOF form.

6. Experimental

6.1. Characterization

Initial materials and products for this work were characterized using X-ray Diffractometry (XRD), Scanning Electron Microscopy with Energy Dispersive X-ray (SEM-EDX), Inductively Coupled Plasma-Mass Spectrometry (ICP-MS), and Inductively Coupled Plasma-Optical Emission Spectrometry (ICP-OES). These different analytical tools are discussed in the ensuing sections following a brief description of the materials and procedures.

6.2. Materials

All reagents used for this work were of analytical grade. Neodymium and lithium fluoride were purchased from Stem Chemicals, calcium fluoride and neodymium oxide were obtained from Beantown Chemical, molybdenum wire was procured from Goodfellow Cambridge Ltd., carbon rod as well as graphite crucibles were acquired from National Carbon Co., Inc., and ultra-high purity (UHP) argon gas was attained from General Distributing Company.

6.3. Electrolysis Procedure

Molten salt electrolytic experiments were conducted using a bath comprised of 72% mole LiF, 18% mole CaF_2 and 10% mole NdF_3 at high chemical purity due to them being analytical grade. This composition was used because LiF has a large electrochemical window and CaF_2 was also added as flux for temperature and viscosity reduction. Furthermore, CaF_2 makes the electrochemical window more negative for lower activity of Li^+ [134]. These materials were combined and thoroughly homogenized using a mortar and pestle. After placing the mixture in a graphite crucible, it was heated with a Thermo Scientific Lindberg Blue-M furnace at a rate of 6°C per minute. Throughout the experiment, argon gas was used to purge the system and prevent contamination from outside gases as shown in Figure 23. The following ranges were used for the

condition variables: temperature (950-1050°C), Nd_2O_3 addition (2-10 wt. %), and dwelling time for the oxide in the bath before electrowinning (1-5 hours). When the beset temperature was reached, the molten mixture was left to dwell before polarizing for the prescribed amount of time depending on the experiment. Carbon rod with average diameter of 6.16 mm was used as the anode and molybdenum rod with a diameter of 1 millimeter (mm) was employed as the cathode. A voltage of 4.9V was applied using a Lambda model LK 340-A power supply with a mean current of 2.5A recorded from the reading gauge. After there is no current reading, the experiment would shut down by itself and the molten bath was allowed to cool to room temperature. The crucible assembly were removed from the furnace, solidified products were carefully removed from the crucible so that they could be analyzed. The crucible and electrodes were reused in subsequent experiments.

Figure 23: Set up of the electrowinning experiment

6.4. XRD

X-ray Diffraction was carried out with a Rigaku Ultima IV X-ray Diffractometer (XRD) using Cu-Kα radiation at 40 kV and 40 mA. This was used to quantify the materials and determine the various phases of the products following the experiments upon solidification and cooling.

6.5. SEM/EDX

A Scanning Electron Microscope coupled with an Energy Dispersive X-ray (SEM-EDX) analyzer was engaged to determine the chemical compositions of all phases in the metal and the spent bath. The SEM/EDX system was a TESCAN TIMA with a tungsten filament and an EDAX Z2 analyzer. Samples were hand-separated, homogenized as needed, and cold-mounted in epoxy using molds approximately 25 mm in diameter and 10 mm thick. Resulting mounts were ground to a smooth finish using a rotary polisher with a series of grit sandpaper of decreasing sizes and comprised of aluminum oxide. Ultimately, the mounts were polished with 0.05 and 0.01µm aluminum powder, washed and dried, and then conductively coated with gold to obtain SEM images by backscattered electron (BSE) detection. EDX analyses helped determine the chemical compositions of all products.

6.6. ICP

Aqua Regia (3:1 v/v HCl to HNO_3) was used to digest the metal. Resulting solutions were analyzed by ICP-OES to determine the elemental content of the resulting metal. Dilution were done with aqua regia as need. Some sample were analyzed by ICP-MS in the Montana Bureau of Mines and Geology (MBMG). This was done to double check the results obtained using the ICP-OES.

6.7. Results and Discussions

6.7.1. Electrolysis

Figure 24(a) and (b) illustrate example products of Nd metal and spent bath obtained for one experiment. The spent bath shows two layers. The lower layer is made of partially dissolved oxide (NdOF) for 2 wt.% Nd_2O_3 and a mixture of NdOF and Nd_2O_3 for the 10 wt.% Nd_2O_3 added. Because it is quite heavy, this material settled to the bottom of the crucible due to the density of the oxide being higher than that of the bath. Thus, the upper layer is light unspent electrolyte which, in industrial settings, could be recycled for further use.

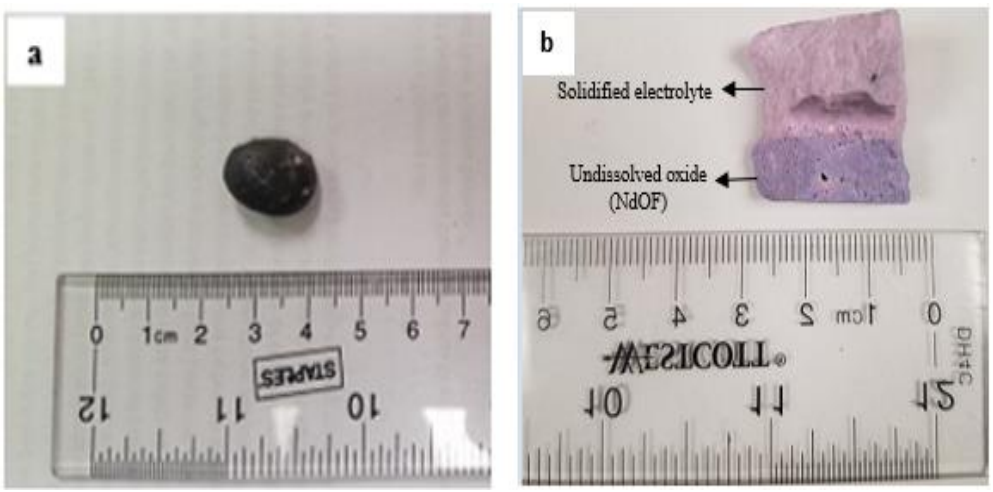

Figure 24: Metal (a) and solidified spent bath (b) recovered from the electrolysis

6.7.2. XRD

XRD patterns in Figure 25(a)-(d) confirm the crystalline phases of samples used. Figure 25(e) and (f) show a typical example of spent bath after electrolysis and cooling. Each of the three fluorides are observed along with neodymium-oxyfluoride (NdOF) when 2 wt.% Nd_2O_3 was added (Fig. 25(e)) and, both Nd_2O_3 and NdOF phases were identified in the XRD pattern when 10 wt.% oxide addition was made. The NdOF is a secondary phase formed from Nd_2O_3

reacting with NdF_3 and/or F^-, similar to Equations 20 and 21, and the Nd_2O_3 peaks shown in Figure 25(f) may be the result of backward reaction (Equations 32 and 33) between the Nd metal and anodic gases [135].

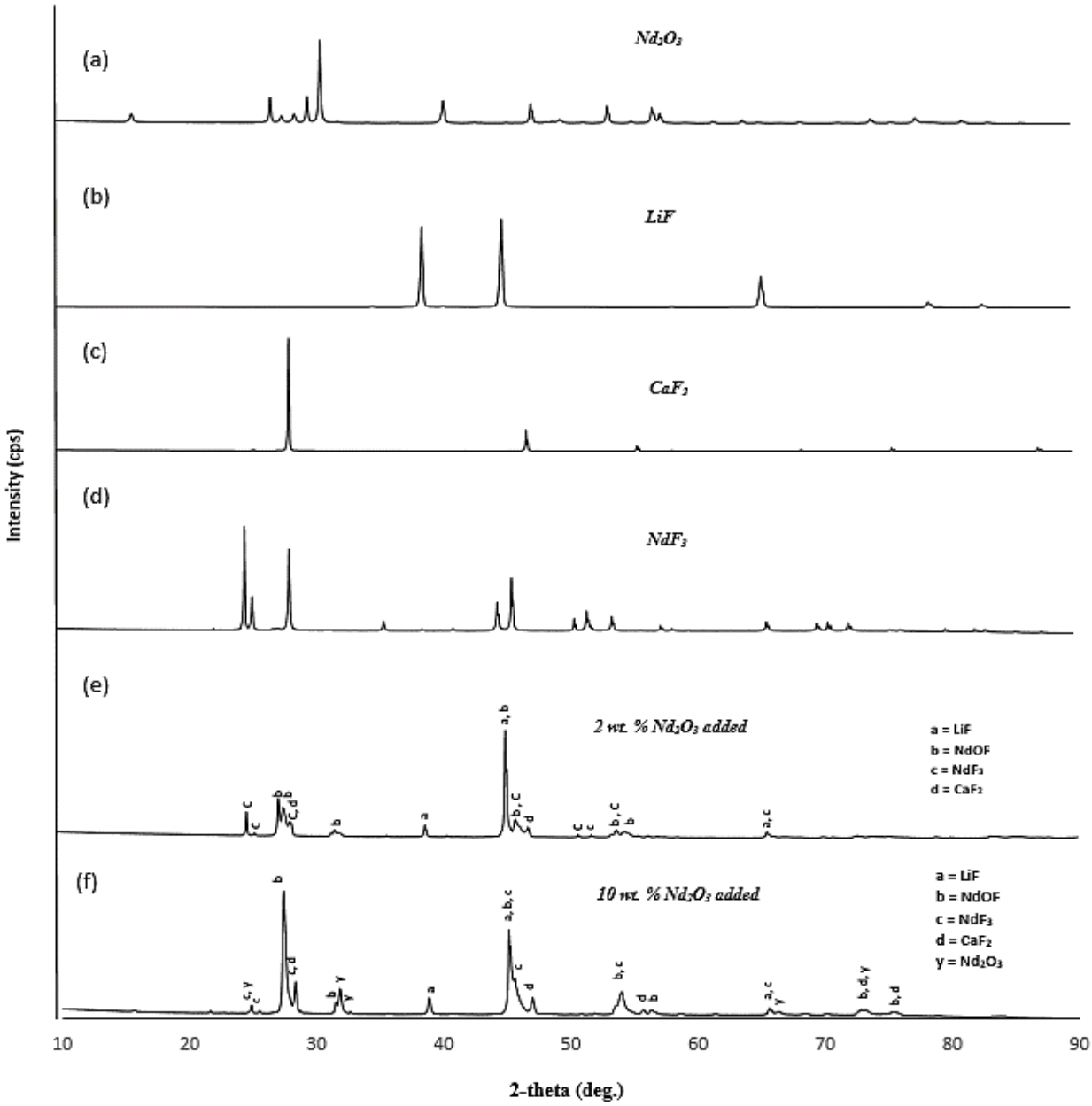

Figure 25: XRD patterns of feed materials and spent bath after solidification.

6.7.3. SEM/EDX

The BSE image in Figure 14 shows there are three distinct phases in the spent bath for 2 wt.% Nd_2O_3 addition. EDX analyses of the three indicated points in Figure 26(a)-(c) show they have a distinctive chemistry: white areas (a) appear to be NdOF correlating to the heavy, undissolved oxide also illustrated in Figure 24(b) and 25(e). The black areas (b) are attributed to LiF; and gray areas (c) are speculated to contain the three fluoride salts, which identifies as the light material in the spent electrolyte, also discussed and shown in Figure 24(b). It is important to note that Li was not observed in Figure 26(b)-(c) because it has too low of an atomic mass to be detected by this technology [136]

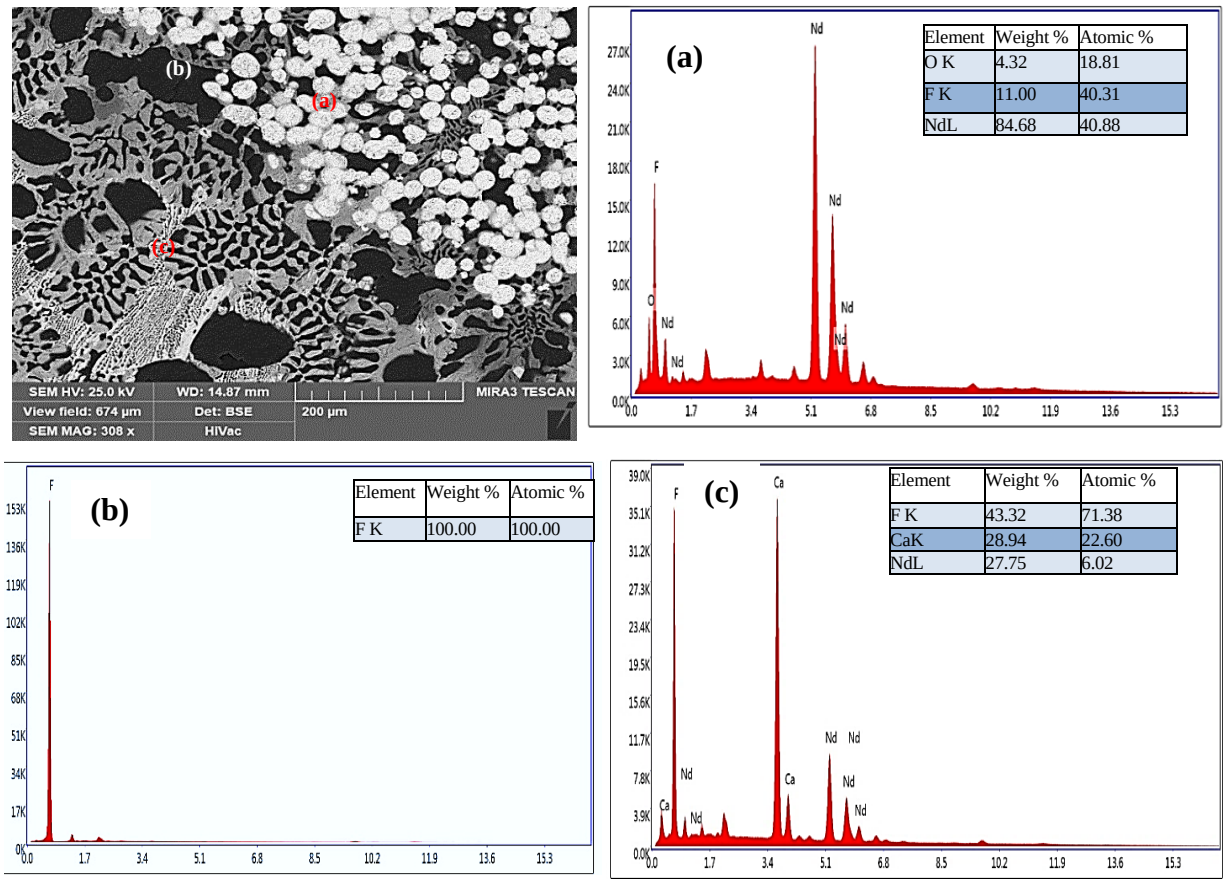

Figure 26: EDX analyses of the 2wt % Nd_2O_3 addition spent bath at the indicated spots on the BSE image

Similarly, the BSE image and EDX analysis of the recovered metal is shown in Figure 27. Results clearly show the micrograph exemplifies pure $Nd_{(s)}$. It is possible that $Li_{(s)}$ could be present because, as noted, it is not measurable with this method. To ensure that Li is not present and to verify that the proper voltage was applied in the experiments, additional analytical techniques had to be used, namely ICP-OES and ICP-MS to help determine the amount if any.

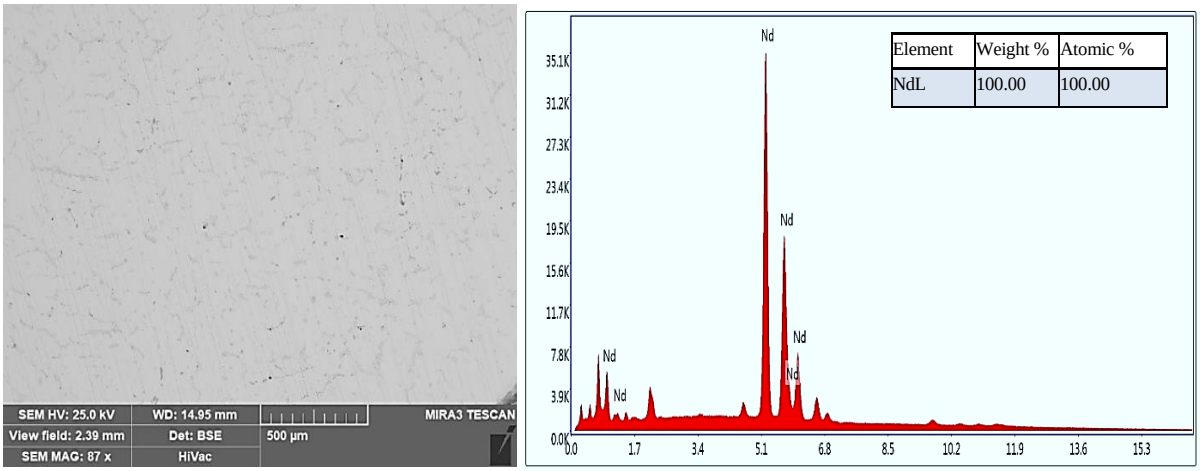

Figure 27: BSE image and EDX analysis of the metal obtained from 2wt % Nd_2O_3 addition

6.7.4. ICP

Table X shows the ICP-OES analysis results of the metal sample. The purity level of the metal is indeed very high with traces of other metallic elements, which are all contaminants from the materials used to perform the experiment. A goal of this research, though, is to maximize current efficiency and metal production.

Table X: Elemental Composition (%) of the Nd made by adding 2% Nd_2O_3 in a Fluoride Salt Electrolysis

Sample composition	Nd	Ca	Fe	Li	Mo	Others
Wt. (%)	99.992	0.00156	0.000915	0.004051	0.001312	4.1791E-06

From the XRD, SEM/EDX and ICP analyses it can be concluded that NdOF forms in the extraction process when the oxide reacts with either NdF_3 of F^- at high temperature and likely becomes insoluble during solidification and cooling, precipitates out as a result, and then settles to the bottom of the cell. While solubilized, it can have little to no participation in the electrolytic reactions because it is not charged. This could also be a factor that decreases the current efficiency and therefore the amount of metal that can be made [87]. A goal of this research, though, is to maximize current efficiency and metal production.

6.7.5. Summary

Based on these findings as well as the discussions in Chapter 6 about the possible reactions, it is not likely that NdOF is directly reduced to $Nd_{(l)}$ metal:

$$NdOF\ \textit{(this is neutral)} + 3e^- \rightarrow Nd_{(l)} + O^{2-} + F^- \qquad \text{Equation 36}$$

Instead, the NdOF must dissolve in the bath as NdO^+ cations which are then attracted to and electrowin out on the negatively charged cathode:

$$NdOF \rightarrow NdO^+ + F^- \qquad \text{Equation 37}$$

$$NdO^+\ \textit{(this is a cation)} + 3e^- \rightarrow Nd_{(l)} + O^{2-} \qquad \text{Equation 38}$$

These reactions were proposed earlier in Chapter 6 as Equations 22 and 24, respectively. They are repeated here for simplicity.

7. Response Surface

7.1. Methodology

In order to moderate the number of experiments and capture the collaborations of the process variables in determining the process performances, Response Surface Methodology (RSM) was pragmatic in the analysis of the experiments. RSM is a mathematical and statistical technique that employs empirical models to fit the experimental data with reference to the detailed experimental design. With the process responses not following a linear model, the Box-Behnken design was employed for designing the experimental matrix to delineate the response surfaces generated by the condition variables [137-139]. This design opts for points in the experimental domain for a three-level factorial arrangement that permits proficient approximation of the first and second order coefficients for the mathematical model [140]. The user acknowledges a high level and a low level of each condition variable and the mid-point is automatically identified for the point selection. A number of experiments (usually 3 or 5) are conducted at the mid-point of all variables to estimate the inherent variability associated with the experimental technique.

For this work, the objectives were to maximize both metal yield and Nd percent recovery in the metal. The reduction experiments were performed per the RSM design of experiments and developed using the statistical software Design Expert 9 procured from Stat-Ease Inc., U.S.A. [141]. During the scoping tests, a number of condition variables were identified that significantly affected the metal yield and Nd recovery. In order to limit the number of experiments, the three most important condition variables were chosen, namely the amount of Nd_2O_3 added, dwelling time (i.e. the time the bath is at the target temperature before electrowinning is commenced), and bath temperature. These variables were also selected because of their effects on solubility. Of

course, the identified responses were metal yield and Nd recovery per the objectives. The selected points in the experimental domain and the responses obtained are discussed in the following section along with the response surfaces, model equations, and the interaction of the condition variables. The optimization process and point predictions are also discussed.

With respect to the E-pO^{2-} diagram (shown previously in Fig. 18b and represented in Fig. 28) and the electrolysis system, it was assumed that the process will be free of oxygen gas such that the only source of oxygen is the oxide in Nd_2O_3 that was added to react with NdF_3 to form NdOF and then NdO^+ and/or Nd^{3+}. While this actual scenario is difficult to achieve, $Ar_{(g)}$ was used to help prevent as much free oxygen as possible and maximize conversion to NdOF from Nd_2O_3.

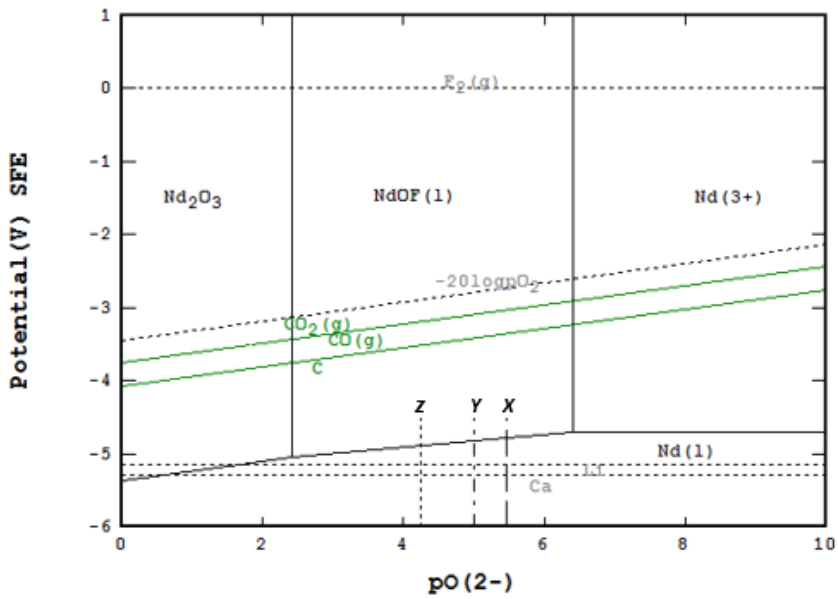

Figure 28: Starting point of Nd_2O_3 wt. % added to the bath

From Equation 20 and, since the amount of NdF_3 is fixed (at 10% mole as part of the salt composition per the design of experiment), calculations were performed to determine the amount of oxygen in Nd_2O_3 that will react with NdF_3 to form NdOF assuming the solubility of Nd_2O_3 in

the bath is 0.51 %mole [32, 87]. Results showed 2 wt.%, 6 wt.% and 10 wt.% excess Nd_2O_3 equated to 3.3557E-6, 1.0072E-5 and 5.7133E-5 moles of oxygen which were then converted to pO^{2-} using the formula $pO^{2-} = -\log[O^{2-}]$ and found to be 5.47, 4.99 and 4.24, respectively. These points are labelled *X*, *Y* and *Z* on the E-pO^{2-} diagram shown in Figure 28.

7.2. Results and Discussions

Table XI shows the Design of Experiments (DOE) along with condition variables and responses. In all, 17 experiments were performed in this part of the study with a temperature range of 950–1050°C, Nd_2O_3 addition range of 2–10 wt. %, and dwelling time range of 1-5 hours.

Table XI: DOE Outlining the Number of Experiments with Their Conditions and Responses

Run No.	Nd_2O_3 (%)	Dwelling Time (hrs.)	Temp (°C)	Metal Yield (g)	Nd Recovery (%)
1	6	5	950	0	0.00
2	6	1	950	0.0942	0.69
3	2	3	950	0	0.00
4	6	1	1050	1.8922	13.80
5	6	3	1000	1.0243	7.47
6	10	5	1000	1.3541	5.92
7	6	3	1000	1.3760	10.04
8	6	5	1050	2.3592	17.21
9	2	1	1000	1.1167	24.44
10	10	1	1000	2.0167	8.82
11	2	5	1000	0.9095	19.90
12	10	3	950	0.0833	0.36
13	6	3	1000	1.3047	9.52
14	6	3	1000	0.7787	5.71
15	6	3	1000	1.2439	9.07
16	10	3	1050	2.4939	10.91
17	2	3	1050	1.4845	32.49

Furthermore, 5 experiments were completed with all condition variables being at midpoints. Results were analyzed to develop a statistically significant model for the responses of metal yield and percentage of Nd recovery as shown in Equations 39 and 40:

$$Metal\ Yield(g) = 1.15 + 0.30A + 0.093B + 1.04C - 0.11AB + 0.23AC + 0.14BC + 0.066A^2 + 0.14B^2 - 0.20C^2 - 0.31A^2B - 0.066A^2C \quad \text{Equation 39}$$

$$Nd\ \ Recovery\ (\%) = 8.36 - 5.31A + 0.68B + 7.58C - 5.49AC + 1.03BC + 4.71A^2 + 1.70B^2 - 2.13C^2 - 2.54A^2B + 3.18A^2C - 2.09AB^2 \quad \text{Equation 40}$$

where, A denotes Nd_2O_3 added, B is the dwelling time, and C stands for temperature.

It may be noted that, in the equations, the process variables are all in terms of the coded values and differ in the range +1 to –1 with the mid-point having a value of zero. Thus, for C, the maximum temperature of 1050°C corresponds to +1 and the lowest temperature of 950°C corresponds to –1 whereas the midpoint temperature of 1000°C corresponds to 0. In order to utilize these statistically significant equations, the actual variable value needs to be converted to the coded form lying between +1 and –1. For example, a temperature of 1010°C corresponds to a value of +0.2 for C. With the help of the model equations, the system was optimized by maximizing the weight of metal yield and the percentage of Nd recovery. The best result with maximum desirability value 0.790 was chosen and the optimum condition along with the responses under these conditions for this case are as follows

Nd_2O_3 addition: 2.197 wt. % *Metal Yield*: 1.556 g *Temperature*: 1050°C

Nd Recovery: 35.48 % *Dwelling Time*: 1 hr

Using Equations 39 and 40, 3-D surface plots in Figures 29 and 30 were generated to illustrate the effects on the responses.

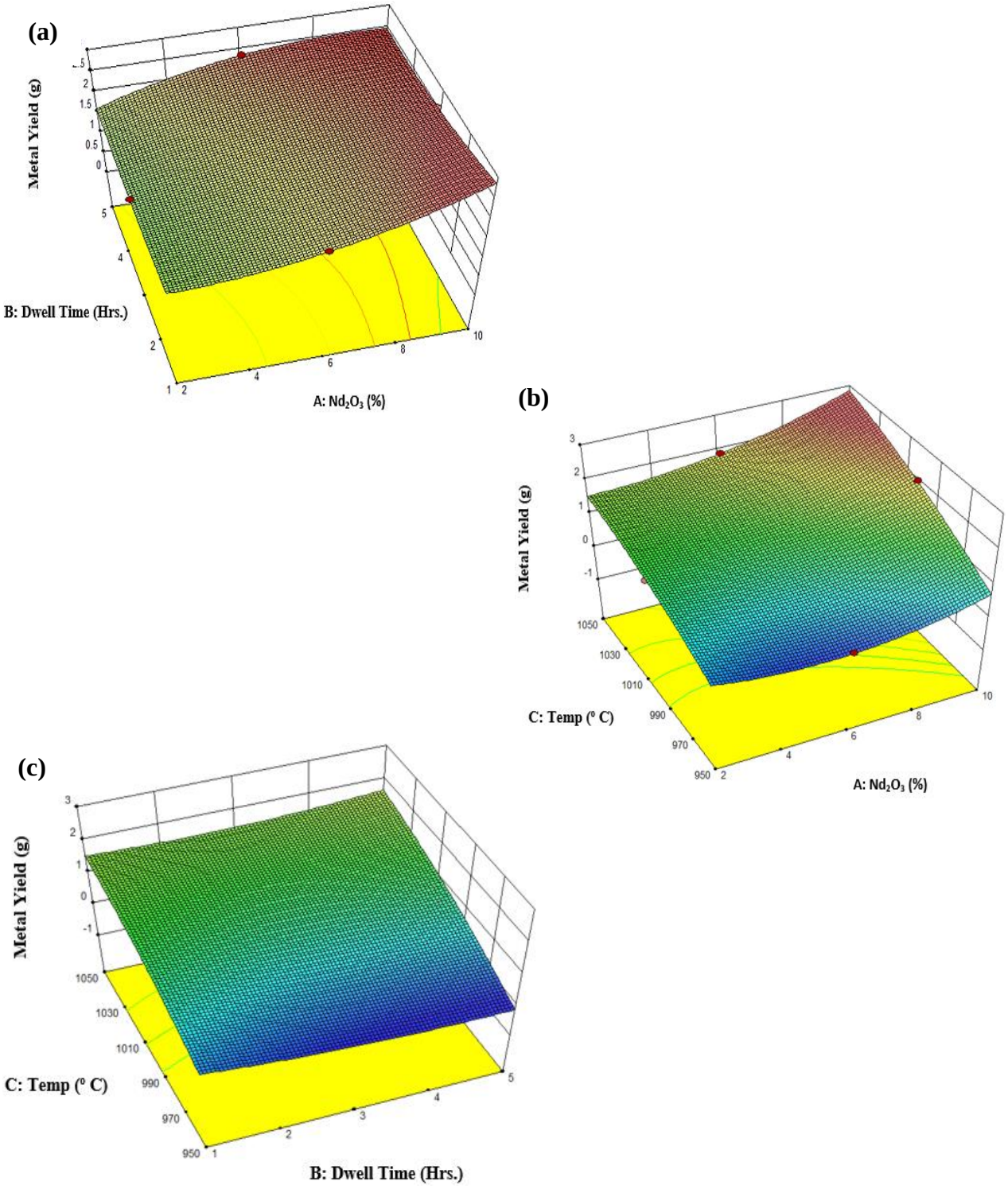

Figure 29: 3D plots of metal yield with respect to process variables at (a) 1050°C, (b) 1 hour, and (c) 2.25% Nd_2O_3

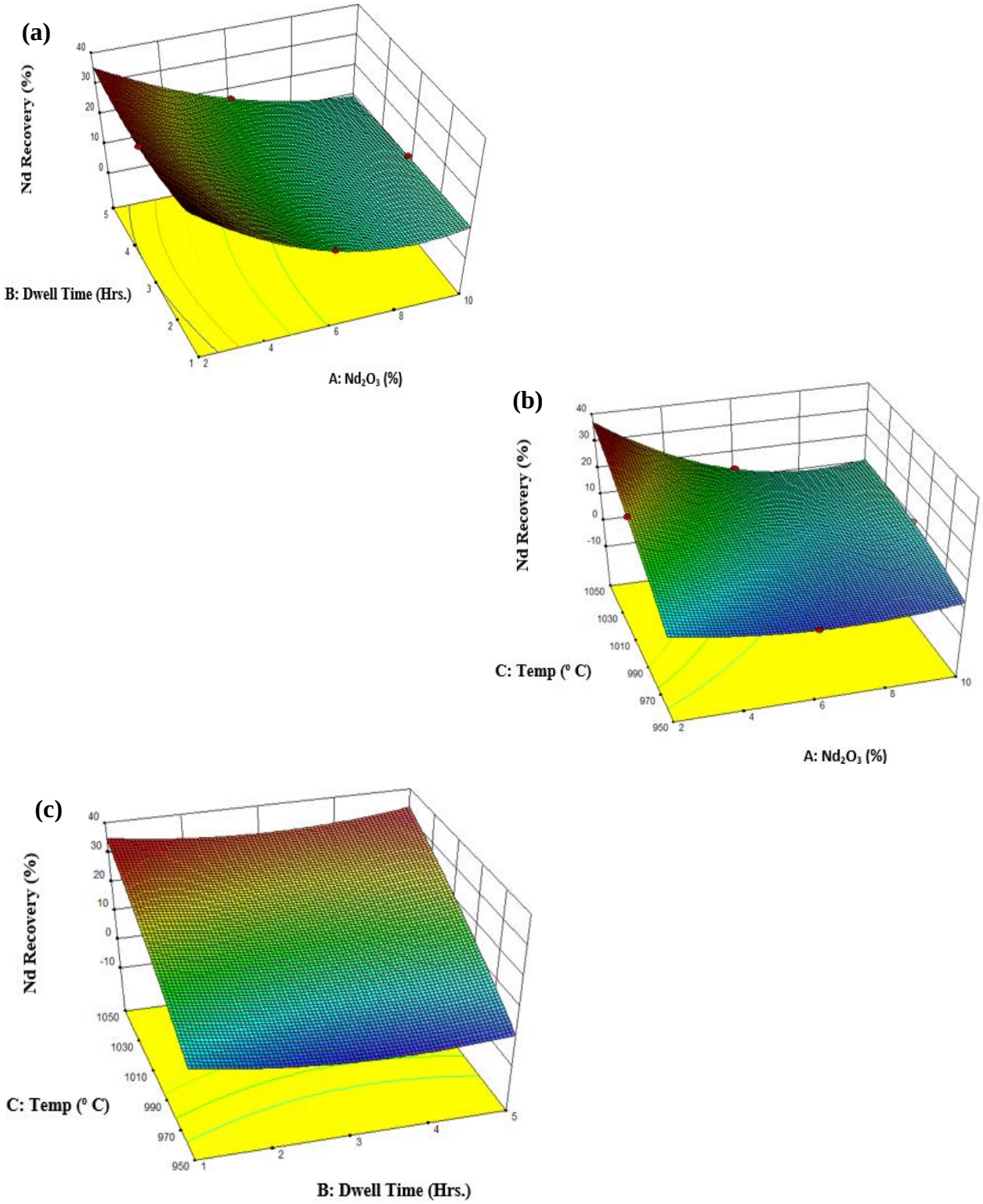

Figure 30: 3D plots of Nd recovery with respect to process variables at (a) 1050°C, (b) 1 hour, and (c) 2.25% Nd_2O_3

Per Equation 39, the 3-D plots in Figure 29(a)-(c) were determined to illustrate the distinction of metal yield in terms of process variables. The plots divulge the impact of temperature, Nd_2O_3 addition and dwelling time on metal yield. From Figures 29(b) and (c) it can be said that temperature appears to have more prominent effect on the process efficiency. It can also be observed from Figures 29(a) and (b) that the metal yield increases to some extent with increasing Nd_2O_3 addition. Evidently, a higher temperature (1050°C) is more conducive for a higher metal yield. Because there is very little dependence of yield on dwelling time, a short dwelling time is preferable. On the other hand, Nd_2O_3 added had less significant impact at low temperature but aided metal yield more significantly at higher temperature.

Comparing with the percentage of Nd_2O_3 added, it is also seen from Table XI and Figures 29(a) and (b) that small amounts of Nd_2O_3 added gave a better Nd metal yield than when higher percentages were added. For the 2 wt.% (which is indicated as *X* in Figure 28 as the starting point) it can be said that the Nd_2O_3 will react with the NdF_3 to form NdOF and after that some of the NdOF will react to form metallic Nd in accordance with Equations 22-24 (see Chapter 6). The same reaction will also occur for 6 and 10 wt.% Nd_2O_3 addition; but, may be influenced by increasing basicity. From Figure 28, it can also be seen that the line between NdOF and Nd begins to slope from pO^{2-} value of 6.5 to 1 which narrows the potential window for Nd electrolysis. The potential window is 0.41V at $pO^{2-} = 6.5$ and is 0V at $pO^{2-} = 1.5$ where the line intersects with the Li line. Consequently, metal yield from 2 wt.% will be more than that at 6 and 10 wt.% in accordance with the DOE values in Table XI.

Examination of Figure 29(a) and (c) reveals that variation of the response with dwelling time is very small throughout the operating regime which implies that dwelling time does not have much of an impact on the metal yield due to the excess F^- in the melt for no oxide addition

and more NdOF in the higher oxide addition cases. When oxide (as Nd_2O_3) is added in the bath, according to Equations 20 and 21, NdOF will form. It will some dissociate into NdO^+ (Equation 22), react with F^- to form $NdOF_5^{4-}$ (Equation 23), or not do anything and essentially remain as a neutral species. It appears the latter predominates with increasing basicity which causes the reaction to decrease.

Figure 30(a)-(c) was generated from Equation 40 and illustrates the response surfaces of Nd recovery in relations to process variables: Nd_2O_3 addition, dwelling time and temperature. From these plots, it is observed that dwelling time again did not influence Nd recovery to any significant extent. However, Nd_2O_3 addition, as observed in Figure 30(a) and (b), has significant impact on Nd recovery. At high temperature, the recovery dropped sharply with oxide addition. With increasing oxide addition, the total Nd content of the melt increased but Nd recovery did not increase proportionally. This is attributed to all of the Nd_2O_3 reacting to form NdOF per Equations 20 and 21. In view of its low solubility, only a small fraction of NdOF would dissociate F^- into NdO^+ according to Equation 22. With NdO^+ thus formed, conversion to metallic $Nd_{(l)}$ by electrolysis per Equation 24 would commence. At high temperature, NdOF solubility is relatively high and therefore, the sharp drop in Nd recovery with oxide addition is prominent. At low temperature, the solubility is poor and leads to low recovery with increasing oxide addition. According to Figure 30(b) and (c), temperature has a much greater influence on Nd recovery and this impact was observed to decrease slightly with increasing Nd_2O_3 addition. This is attributed to higher oxide solubility because more NdOF will form and solubilize at higher temperature. Clearly, the melt temperature was by far the most dominant factor on the process as a whole.

Interestingly, the interactive terms (AB, AC, A^2, B^2, C^2, A^2B, A^2C, AB^2, and BC) in the model Equation 39 and 40 also has a substantial consequence on the complete term because most of the interactive terms have a large coefficient, consistent with the size for the variables. For this reason, when values for the variable ranges are substituted into the Equations, the interactive terms will have a noticeable effect on the outcome. On account of this, it is imperative to understand that the use of these Equations are constrained to the variable ranges that were used and not outside them.

With respect to temperature, it can be said that this study confirms Le Chatelier's Principle which predicts how much a system will respond to a change in external conditions. Considering this work where the solubility process is endothermic, increase in temperature makes more heat available to the dissolution process. Thus, the dissolution increases with an increase in temperature and aids the metal deposition process.

The solute dissolution rate (*dm/dt*) is affected by the addition of more solute (Nd_2O_3) to the solvent (molten bath). But since Nd_2O_3 has a low solubility in fluoride, it appears that the addition of more Nd_2O_3 alters the Nd deposition mechanism with respect to the bath to a limited extent as shown in Figures 29 and 30 [94]. Dissolved oxide concentration cannot be increased too much by adding excess oxide into the bath at constant temperature and fixed salt composition. However, oxide addition can increase the kinetics of the reactions because increasing the concentration of a reactant increases the number of collisions between the reacting species and therefore increases the reaction rate [100]. This will be truer if all the oxide is dissolved. It does not happen as much at lower temperature due to the low solubility of the oxide, so the addition of the oxide merely increases the Nd content of the melt by means of forming insoluble oxyfluoride.

The sharp drop in Nd recovery with addition of oxide bears a testimony to the low solubility of oxide in the fluoride bath. Of course, the solubility increases at elevated temperature as observed in the present investigation by the increased metal yield and Nd recovery. With more addition of oxide, the Nd recovery dropped sharply due to the limited solubility even at higher temperature. Enhanced REO solubility leads to higher concentration of Nd^{3+} cations in the melt. This is why the metal yield and Nd recovery increases. But with increased Nd_2O_3 level and limited solubility, even at higher temperature, the Nd recovery dropped sharply. The oxide addition merely increased the available Nd in the melt. Evidently, the solubility, at any specified temperature, is the limiting factor in this case. Additionally, dissolution rates change from one system to another and, according to the Noyes-Whitney equation, solute dissolution is time dependent. Since solubility is the deciding factor of how much solute dissolves in a solvent, substances with low dissolution rates typically exhibit low solubility while substances with high solubility leads to high dissolution rates.

Cogitating all of these discussions, it is quite justified that a high temperature with low Nd_2O_3 addition will help in the achievement of better metal yield with maximum Nd metal recovery. Dwelling time does not appear to be so critical beyond the one hour and therefore, a short dwelling time would be advisable.

Faraday's Law of electrolysis was also used as a check on the optimum values from the statistical model. This law is ideal and provides the amount (grams) of metal yield that will be recovered in an electrolysis process represented in the expression:

$$m = \frac{QM}{FZ} \qquad \text{Equation 41}$$

where, *m* is the mass (g) of metal yield, Q is the total electric charge passing through the electrolyte, F is Faraday's constant, *M* is the molar mass of the type of metal electrowon, and *Z* is the valance number of ions of the metal. With a mean current reading of 2.5A being applied for 1 hour, the value for metal yield (g) per Equation 41 is 4.484g; however, only 1.556g was obtained. This low faradic metal agrees with literature [142]. Note that the 1 hour used in this calculation is the duration time that the electrolysis was done (i.e., the time from the voltage being turned on to the system shutting down).

High current efficiency is necessary for any cathodic or anodic process because it is used to determine if the reactions proceed unimpeded. In rare earth extraction from molten salt, current efficiency is generally low, and for Nd metal electrolysis, current efficiency can be computed by Equation 42 [89,143]:

$$w = \frac{100m}{itz} \qquad \text{Equation 42}$$

where w is the current efficiency (%), m is the mass (g) of metal yield, *i* is current (amps), t is time (hours) the voltage was applied, and z is electrochemical equivalent of the metal.

Similarly, by using the mass of Nd (metal yield) obtained using Faraday's laws and experimental values (duration of 1 hour and current of 2.5A), computation of current efficiency was 100%. However, when this same calculation is done with respect to the metal yield from the statistical model, current efficiency of 34.7%. This difference is attributed to anodic and cathodic spacing as shown in Figure 31.

Because the cell used in this study is small, the anodic-cathodic spacing is limited which affects the current efficiency negatively [86]. Other factors, as already stated, can also affect current efficiency; however, most agree that the formation of species unfavorable to the

electrolysis (such as neutral NdOF) as well as back reactions (such as Equations 32 and 33) between the electrowon metal (in the melt) and anodic gases are the most prevalent [86].

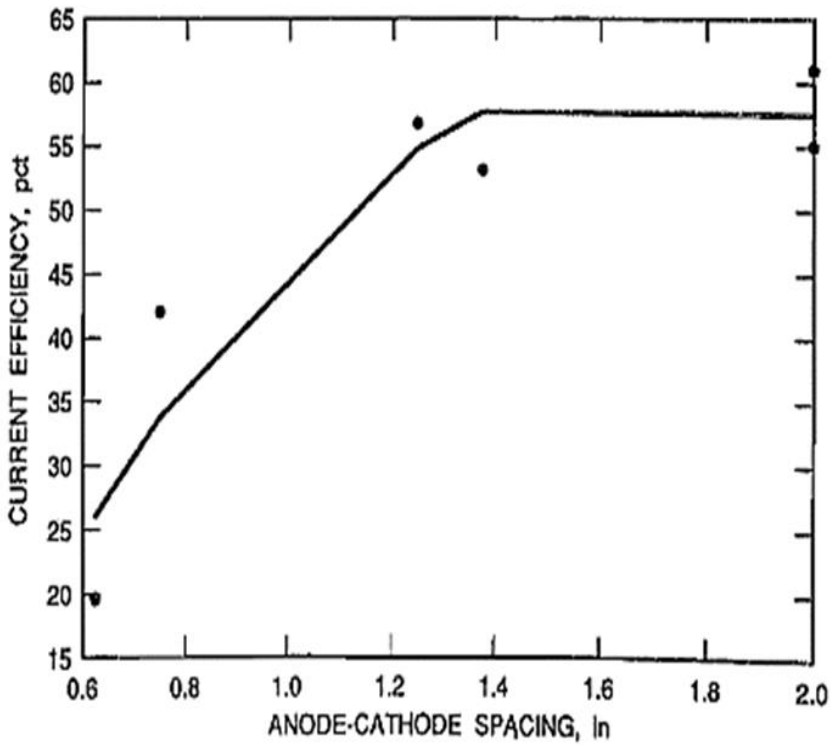

Figure 31: Current efficiency vs anode-cathode spacing [86]

8. Electrochemical Measurement

8.1. Cyclic Voltammetry

Electrochemical studies with cyclic voltammetry (CV) involve measuring current responses as a potential scan is applied to a working electrode at an unremitting rate in a forward and reverse directions with single or multiple cycles [144]. Typically, an electrochemical cell entails two electrodes immersed in electrolyte. In a cell used for electroanalytical measurements like cyclic voltammetry, three electrodes are mostly used due to the complications that arise from the synchronized measurement of current and potential as shown in Figure 32. Although not used in this study, cyclic voltammetry can be done with four electrodes with a second reference electrode used to monitor the counter electrode.

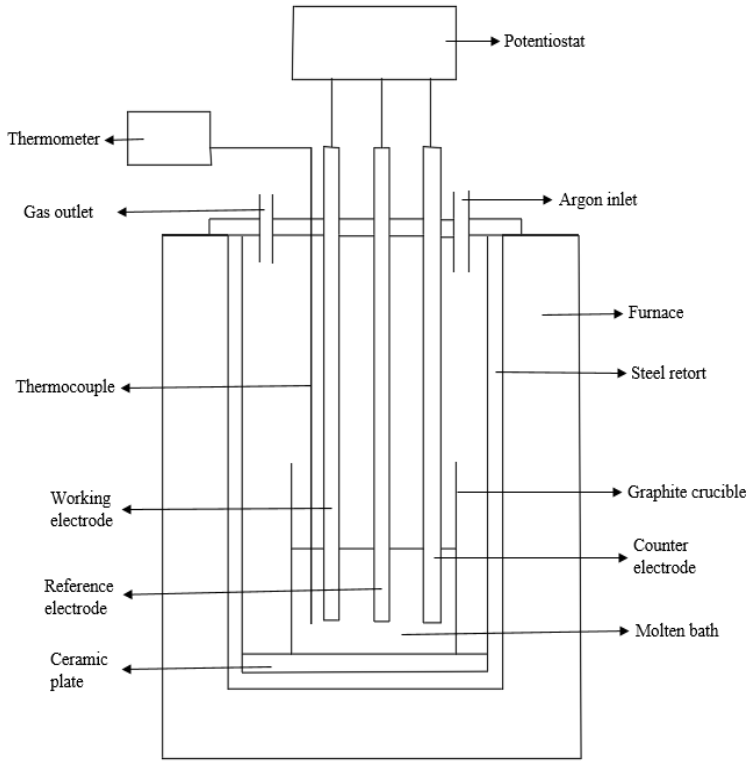

Figure 32: Cross-section of a three-electrode connection cell inside the furnace

In the three-electrode system, one electrode is the working electrode (WE). It is the electrode at which the electrochemical phenomena (reduction or oxidation) being investigated take place. Connected to the WE is a second electrode, either called a sense electrode or reference electrode (RE). The combination of both electrodes is often referred to as the working-sense or working reference. Both are component of the differential amplifier that measures/controls the voltage between both electrodes [145]. The RE is the electrode whose potential is constant enough that it is taken as the reference standard against which the potentials of the other electrodes present in the cell can be measured. For best results, the RE and WE need to be as close to each other as possible without being in contact. The third functional electrode is the auxiliary or counter electrode (CE) which serves as a source or sink for electrons so that current can be passed from the external circuit through the cell. In essence, the CE and the WE are oppositely polarized such that, for example when one is at +1V, the other is at -1V. All these electrodes were used in this research to conduct cyclic voltammetry experiments and verify the E-pO^{2-} diagram for Nd in fluoride bath at 1050°C.

For aqueous systems, as reported earlier, the E_H-pH diagram for a metal is used to express conditions of thermodynamic equilibrium of all the reactions that can occur when the metal is in contact with an aqueous solution at a given temperature. Also, any solid, liquid, gas or dissolved substance having a definite chemical potential in the presence of an aqueous solution only at conditions corresponding to certain definite domains in an E_H-pH diagram. In a CV study of this system, the commonly used reference electrodes are silver-silver chloride electrode (Ag/AgCl/4M KCl, E= 0.222V) or the Calomel electrode (Hg/HgCl/KCl). Studies have been used to show voltammetric experiments as a function of pH can be used to predict and verify E_H-pH diagrams. Examples of voltammetric behavior are numerous but include, for one, chalcocite

electrodes over a wide range of solution pH reported by Young et al. (1988) yielded CV results that agreed with the E_H-pH diagram predicted with metastable copper sulfide phases identified by Koch and McIntyre (1976) [146-148]. Also, Grujicic et al. (2002 and 2005) studied reaction and nucleation mechanisms of copper electrodeposition from ammoniacal solutions on vitreous carbon. They showed an AFM morphology of copper deposition at different stages of the cyclic voltammetry for pH 4, 6 and 8 as shown in Figure 33 [149,150].

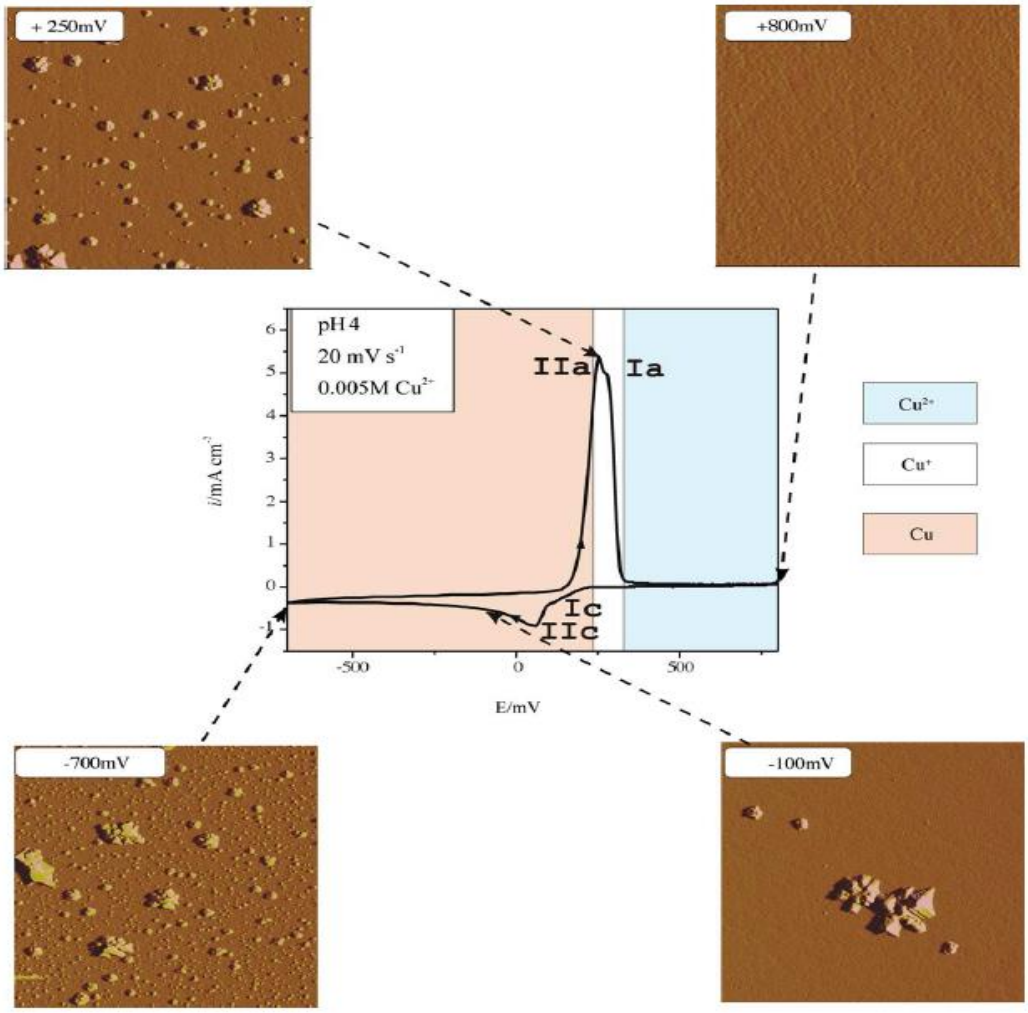

Figure 33: AFM morphology of the copper deposition at different stages of the cyclic voltammetry for pH 4 [149,150]

In non-aqueous systems, however, the electrolyte is molten salt bath, often with a dissolved oxide. This system consists of charged ions and neutral combinations as well as solvent molecules referred to as the molten bath [151]. Similar to the aqueous system, E-pO^{2-} diagrams have been designated for thermodynamically modeling molten salt systems as reported in Chapter 6. Because high temperatures and corrosion associated with the system, wires comprised of precious metals, like Pt with a high melting temperature, are usually used as the reference electrode. Even at these high temperatures, the precious metal wires have excellent electrochemical activity and superior oxidation resistance [152-153].

8.2. Experimental

All electrochemical experiments were carried out in a laboratory in a glassy carbon crucible inside a steel retort under an inert atmosphere of Argon gas in a three-electrode set-up at 1050°C. A Mo wire (1mm in diameter) was used as the working electrode, a graphite rod (6.17mm in average diameter) served as the counter electrode, and a Pt wire (1mm in diameter) was used as the reference electrode. The instrumental equipment consisted of a high power potentiostat Princeton Applied Research VersaSTAT 4 made by AMETEK Scientific Instruments as shown in Figure 34. The instrument was connected to a computer by a Universal Serial Bus (USB) connector. The system enabled computer control of the electrochemical processes and simultaneously provided data acquisition and processing by VersaStudio software developed by producers of the potentiostat. All experiments were done on with an initial potential of -0.5, vortex potential of -2 and a final potential of -0.5V under varied scan rate. Materials (if needed) were combined and thoroughly homogenized by means of a mortar and pestle and, after that, the mixture were placed in the glassy carbon crucible. It was then heated

with a Thermo Scientific Lindberg Blue-M furnace at a rate of 6°C per minute until attainment of the targeted temperature.

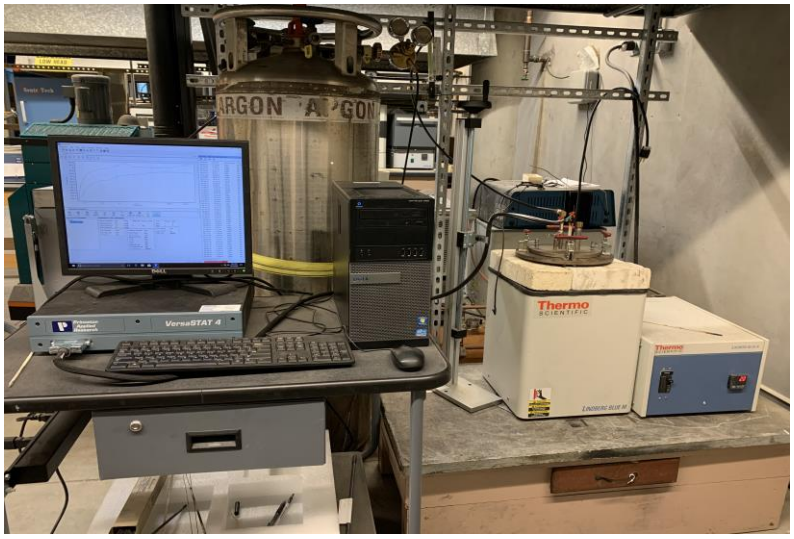

Figure 34: Cyclic voltammetry experimental setup

8.3. Results and Discussions

The cyclic voltammogram of only LiF at 1050ºC in Figure 35 was collected with Mo as WE, C as CE, and Pt as RE. It exhibits one peak in the cathodic run at B and another in the anodic run at B'. The shape of B is typical of the anodic reduction of Li^+ to Li and B' is the reverse and therefore the cathodic oxidation back to Li^+ as illustrated by Equations 43 and 44:

B *(reduction)*: $Li^+ + e^- = Li$ Equation 43

B'*(oxidation)*: $Li = Li^+ + e^-$ Equation 44

Figure 36 shows the cyclic voltammogram of LiF with CaF_2 at the eutectic composition of 70 LiF-30% CaF_2. Both CV's are compared in Figure 37. Results show the appearance of two new peaks at A and A' which must be due to the addition of CaF_2. It is therefore concluded that the

peaks must be due to the reduction and oxidation of calcium (Ca) as shown in Equations 45 and 46:

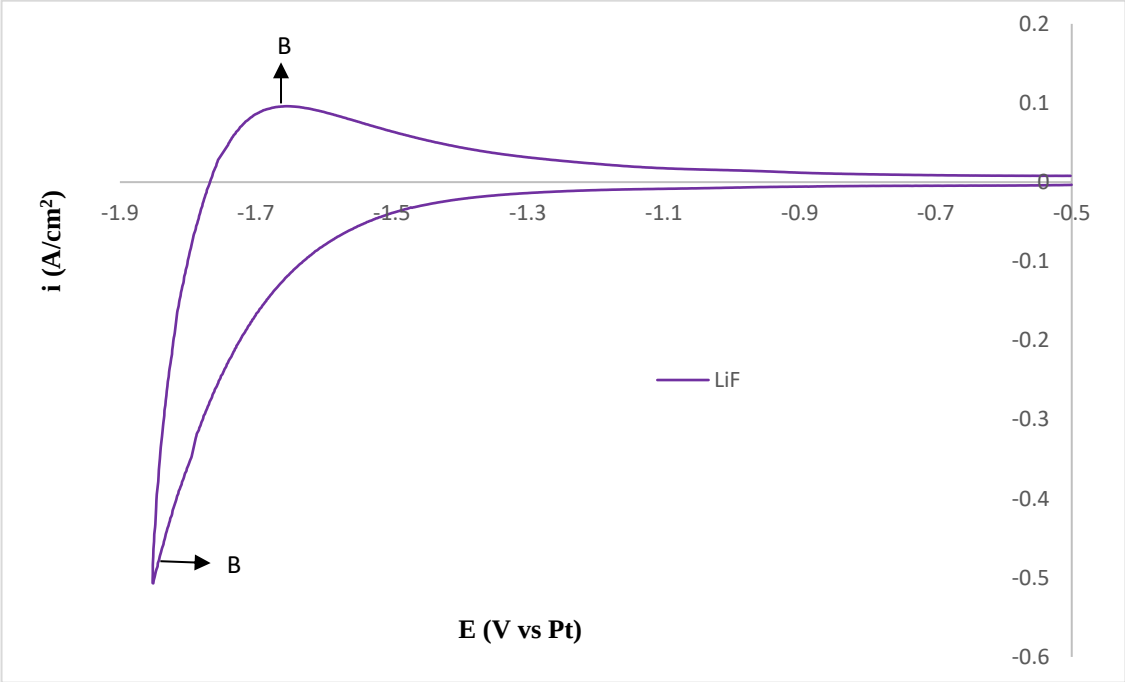

Figure 35: Cyclic voltammogram of LiF at 1050°C; working electrode: Mo; counter electrode: carbon; reference electrode: Pt; scan rate = 0.001V/s

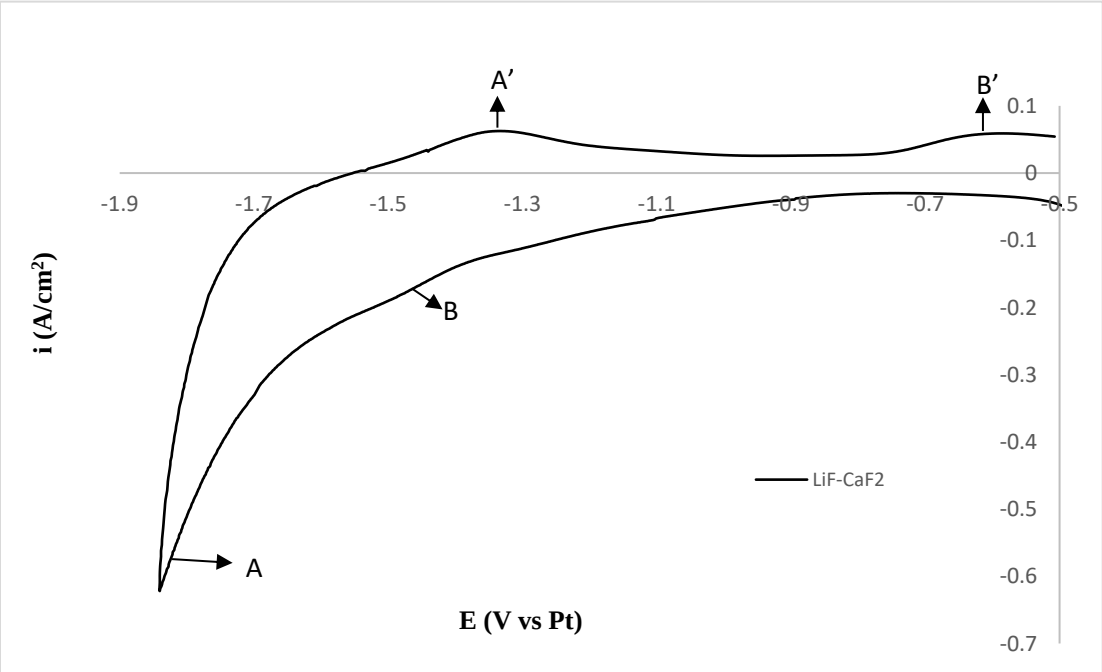

Figure 36: Cyclic voltammogram of LiF-CaF_2 eutectic composition at 1050°C; working electrode: Mo; counter electrode: carbon; reference electrode: Pt; scan rate = 0.001V/s

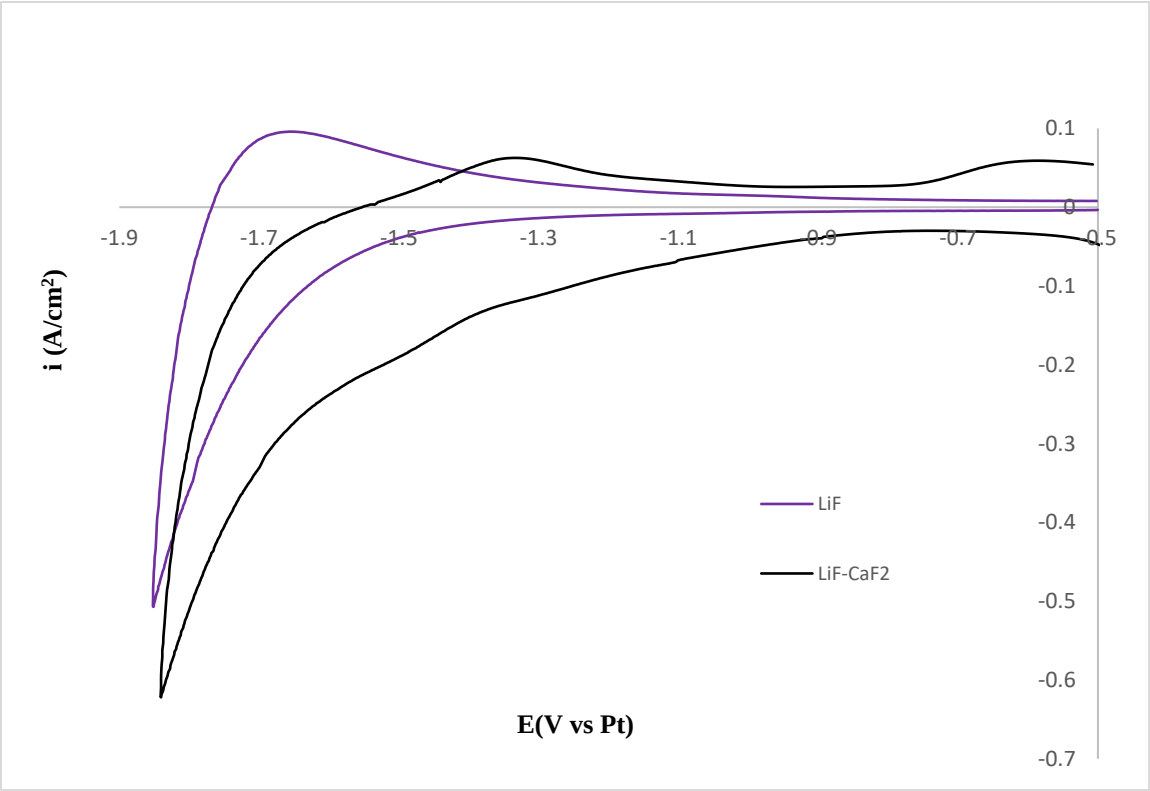

Figure 37: Cyclic voltammogram of LiF and LiF-CaF_2 eutectic composite on at 1050°C; working electrode: Mo; counter electrode: carbon; reference electrode: Pt; scan rate = 0.001V/s

A *(reduction)*: $Ca^{2+} + 2e^- = Ca$ Equation 45

A' *(oxidation)*: $Ca = Ca^{2+} + 2e^-$ Equation 46

which are similar to the Li reactions in Equations 43 and 44. The reaction in Equation 43-46 must be avoided in order for Nd electrolysis (Equations 17 and 24) to occur which requires the applied voltage to be within the potential window that Nd^o, Li^+ and Ca^{2+} are simultaneously stable. This range is below Nd^{3+}, Nd_2O_3 and NdOF stability regions and above the stability region of Li and Ca in Figure 18(b). As discussed previously in Chapter 6, this potential window varies with pO^{2-} (basicity) of the system. Furthermore, in this range, F^- is stable and will not convert to $F_{2\,(g)}$ as also discussed earlier regarding Equation 28.

$LiF\text{-}CaF_2\text{-}Nd_2O_3$ and $LiF\text{-}CaF_2\text{-}NdF_3$ plots are shown in Figure 38. Because of the introduction of Nd_2O_3 and NdF_3, it can be seen that additional peaks appear on the voltammogram plots which must be attributed to Nd. In this respect, peaks C and C' represent the reduction and oxidation peaks as shown in Equations 47 and 48, respectively:

$$C\ (\textit{reduction}):\ Nd^{3+} + 3e^- = Nd \qquad \text{Equation 47}$$

$$C'\ (\textit{oxidation}):\ Nd = Nd^{3+} + 3e^- \qquad \text{Equation 48}$$

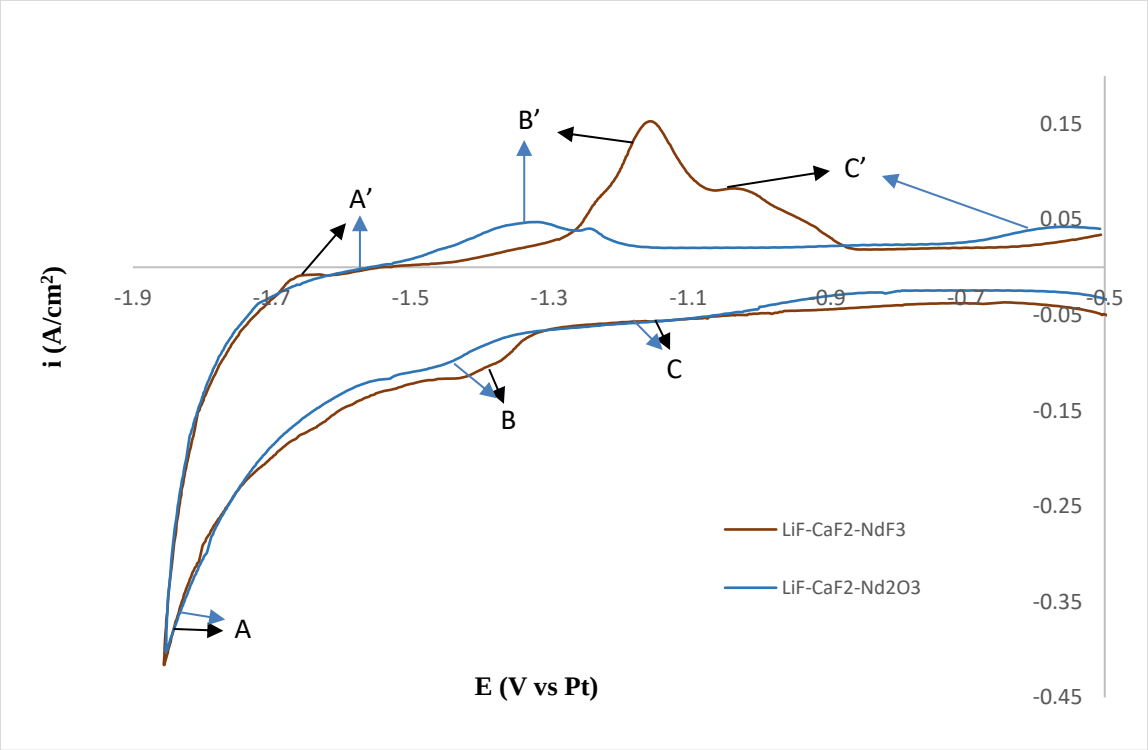

Figure 38: Cyclic voltammogram of $LiF\text{-}CaF_2\text{-}NdF_3$ and $LiF\text{-}CaF_2\text{-}Nd_2O_3$ composition at 1050°C; working electrode: Mo; counter electrode: carbon; reference electrode: Pt; scan rate = 0.001V/s

Equations 47 and 48 are representative and therefore could involve redox reactions of other Nd species such as NdO^+ and $NdOF_5^{4-}$, etc. and thus are not exclusive. Comparing the two CV's shows anodic scan is fairly clean such that C occurs before B which occurs before A. Clearly, the potential window to operate within is between C and B. On the other hand, the

cathodic side shows peaks (represented by A', B' and C') shifting to lower potentials. This is attributed to the Nd_2O_3 system being more basic than the NdF_3 system. Nd_2O_3 would increase (O^{2-}) and therefore decrease pO^{2-} causing the peaks to shift. However, there are other factor that play a role including but not limited to alloy formation, deposition effects, and subsequent kinetics as cathodic oxidation leads to dissolution.

Figure 39 results when Nd_2O_3 and NdF_3 are both added to the molten $LiF\text{-}CaF_2$ bath. For this experiment, Nd_2O_3 was 2.197 wt.%. In this case, both the anodic and cathodic scan are straight forward. Thus C/C' clearly represent Nd/Nd^{3+} equilibrium, A/A' are Ca/Ca^{2+} and B/B' relate to Li/Li^{+} which would concur with the E-pO^{2-} diagram.

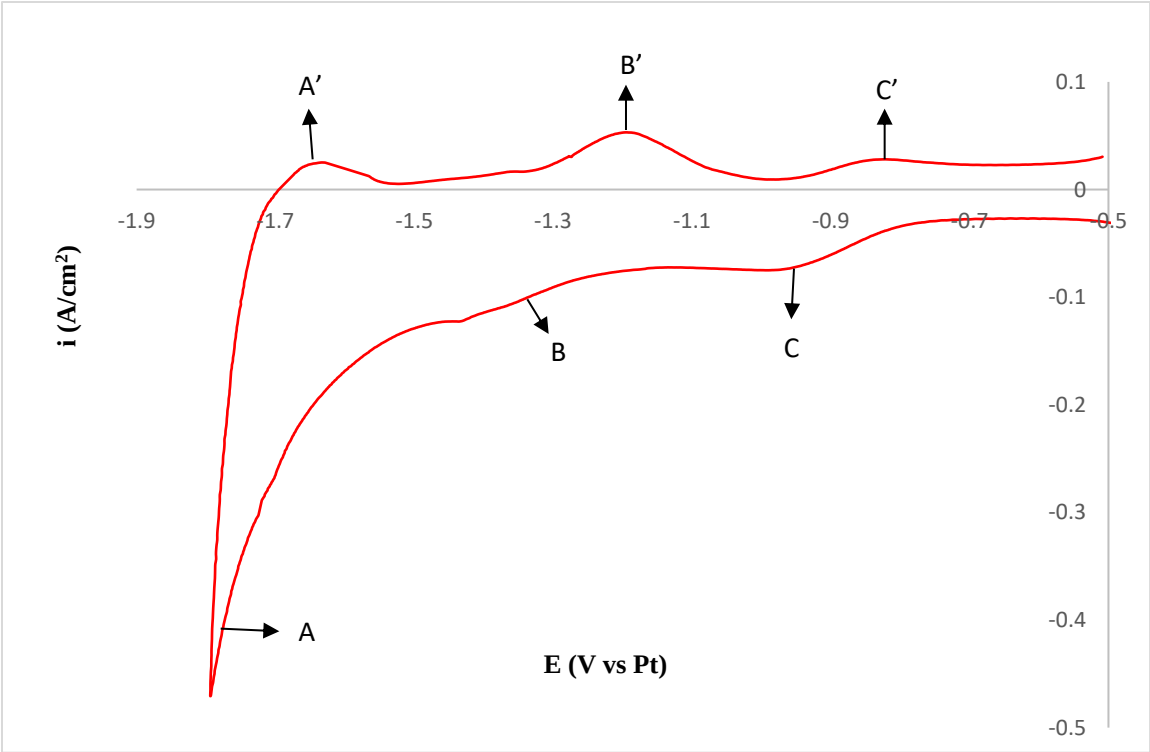

Figure 39: Cyclic voltammogram of $LiF\text{-}CaF_2\text{-}NdF_3$-2.197wt. % Nd_2O_3 composition at 1050°C; working electrode: Mo; counter electrode: carbon; reference electrode: Pt; scan rate = 0.001V/s

Calculations show that 2.197 wt.% Nd_2O_3 is equivalent to a pO^{2-} value of 5.43. When this value is projected onto the E-pO^{2-} diagram, it intersects the line between Nd and NdOF at -4.76V. Plotting the CV onto the E-pO^{2-} diagram such that the 0-current axis lies at the pO^{2-} = 5.43 results in Figure 40. As illustrated, the interval between -4.76 and -5.15V (the Li line) matches the window at which Nd can be electrowon. It is a range of 0.39V which agrees quite well with peak C for Nd formation on the voltammogram. Similarly, the Li reduction window between -5.15 and -5.30V concur with peak B and potentials below -5.30V is where Ca reduction occurs in agreement with peak A. Clearly, this substantiates that the E-pO^{2-} diagram agrees with the cyclic voltammetry results.

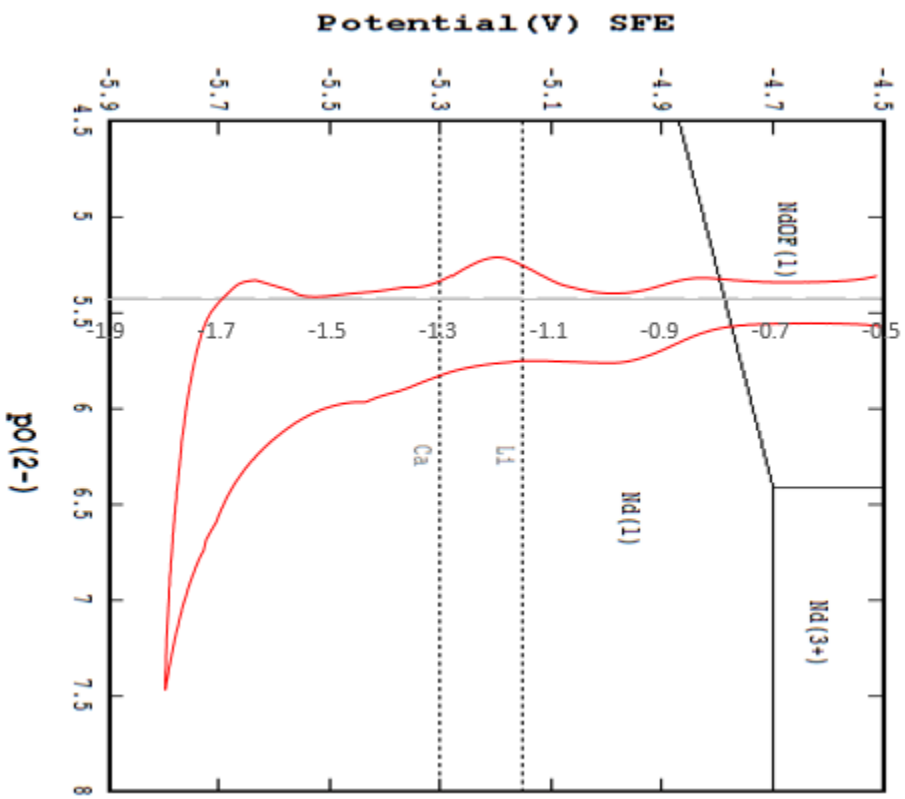

Figure 40 : Agreement between the E-pO^{2-} diagram and the cyclic voltammetry of LiF-CaF_2- NdF_3 -Nd_2O_3 (2.197 wt. %) composition at 1050°C

With 0.2 wt. % of Nd_2O_3 was added to the salt composition, the resulting CV in Figure 41 was obtained. As before, reduction (peaks C, B and A) and oxidation (peaks C', B' and A') reactions are shown. From the voltammogram, it can be said that Nd(III)/Nd reaction occurs followed by the Li(I)/Li and then Ca(II)/Ca in correspondence with the E-pO^{2-} diagram.

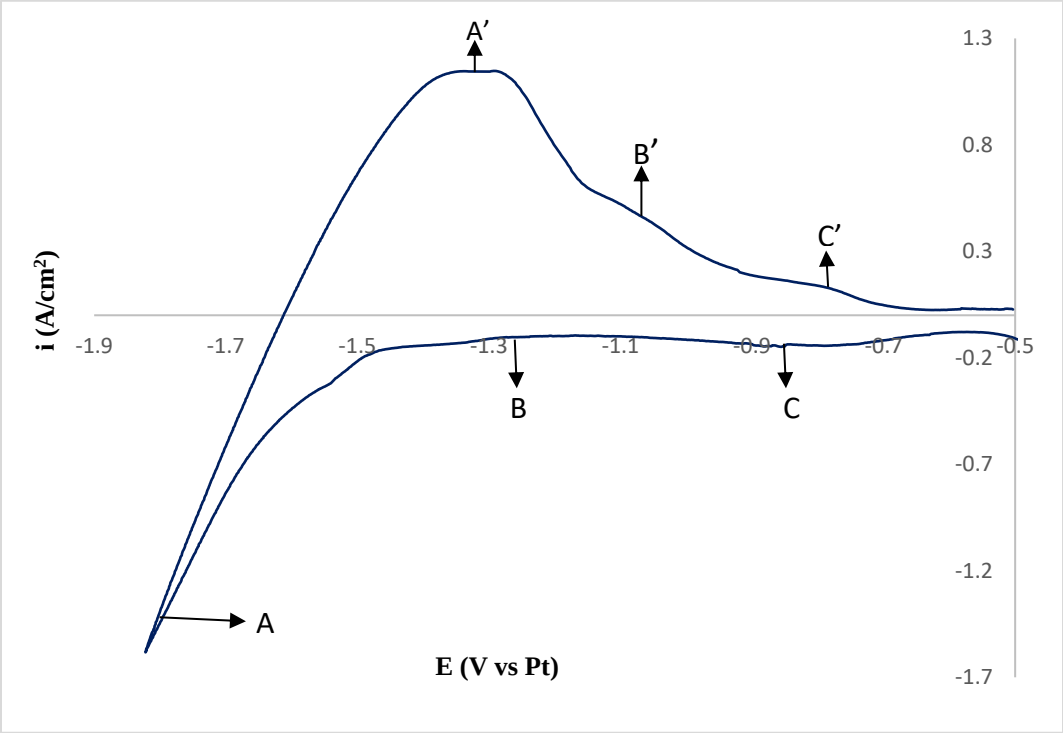

Figure 41: E-pO^{2-} diagram and the cyclic voltammetry of $LiF-CaF_2$- NdF_3 -Nd_2O_3 (0.2 wt. %) composition at 1050°C

In the case, calculation show that 0.2 wt.% Nd_2O_3 corresponds to a pO^{2-} value of 5.94 and, when this point is projected onto the E-pO^{2-} diagram, it intersects the line between Nd and NdOF at -4.74V. As illustrated on Figure 42, the interval between -4.74 and -5.15V (the Li line) is the window at which Nd can be electrowon. Under these conditions, the window has a range of 0.41V, corresponds with peak C, and is slightly longer than in Figure 40. This value also agrees with the reduction interval value for Nd formation on the CV. The Li reduction window

between -5.15 and -5.30V is also in agreement (peak B) as is the Ca reduction (peak A) below -5.30V. As before, this substantiates the E-pO^{2-} diagram.

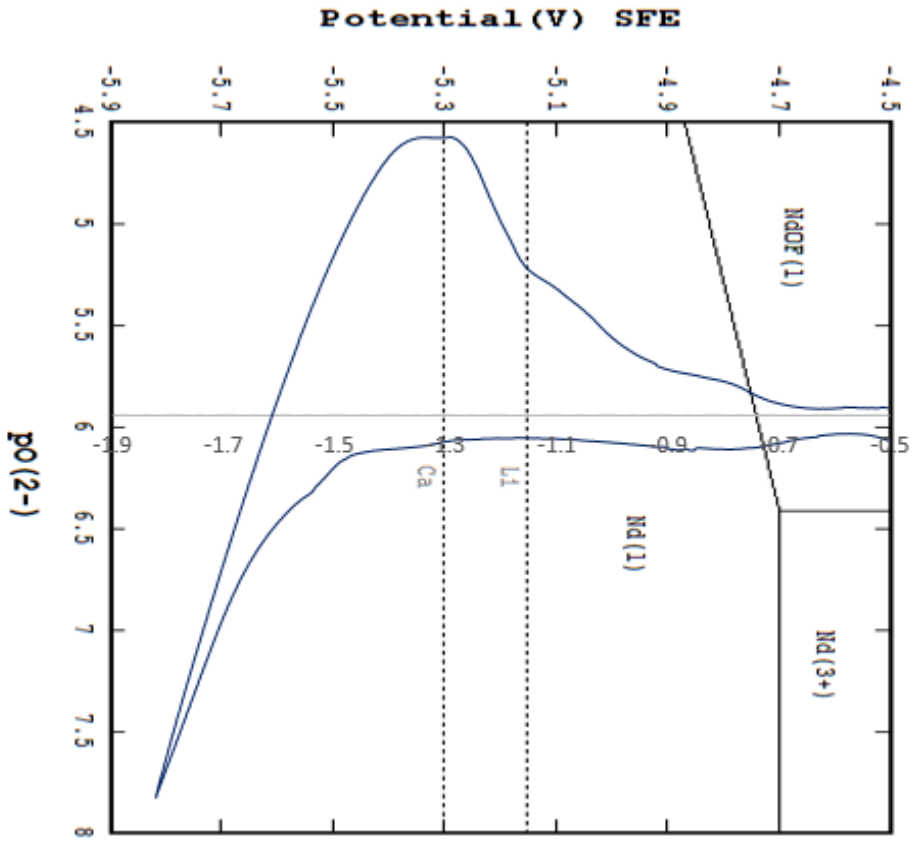

Figure 42: Agreement between the E-pO^{2-} diagram and the cyclic voltammetry of LiF-CaF_2- NdF_3 -Nd_2O_3 (0.2 wt. %) composition at 1050°C

For the CV potentials to match up with that of the E-pO^{2-}, a potential value of -4.0V needs to be added to the CV potential to get them to scale the same. This -4.0V is attributed to the C and $CO_{(g)}$ reaction that occurs on the surface of the reference electrode as shown previously in the Equation 30.

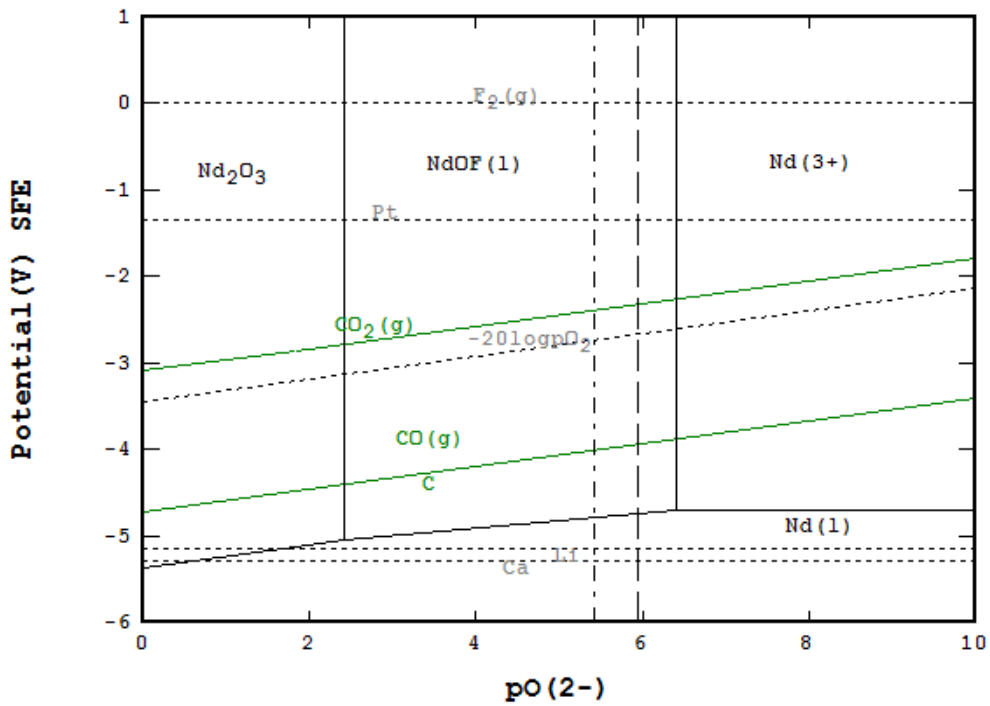

Figure 43: E-pO^{2-} diagram showing the Pt line and where the C/CO(g) line intersect both 2.197 and 0.2 wt. %Nd_2O_3 addition lines at 1050°C

To demonstrate, Figure 43 was developed from the same assumptions as Figure 18(b) except it was assumed $P_{CO(g)}$ was 10^{-6} atm for the $C_{(s)}/CO_{(g)}$ equilibrium (see Reaction 30). As shown previously, 2.197 and 0.2 wt.% Nd_2O_3 equate to pO^{2-} of 5.43 and 5.94, respectively. These are plotted as the vertical dashed lines in Figure 43 and are shown to intersect with the $C_{(s)}/CO_{(g)}$ line at -4.0 and -3.96 V vs SFE, respectively. In essence, both values are -4.0V which is all that is needed to convert the potentials in the CV work from V vs Pt to V vs SFE. In this regard, -4V is added to the potential scale used for the CV's to make them V vs SFE so that they would be the same scale as the E-pO^{2-} diagrams. Results are shown in Figure 44. Clearly, the anodic scans on both CV's show current beginning to flow at potentials that match those of thermodynamically calculated equilibria on the E-pO^{2-} diagrams. The close agreement of the potential values suggests converting the CV potentials from V vs Pt to V vs SFE by adding -4V

is good. In fact, the results are surprising considering that it was based on an assumption that $P_{CO(g)}$ was 10^{-6} atm for the $C_{(s)}/CO_{(g)}$ equilibrium (see Reaction 30).

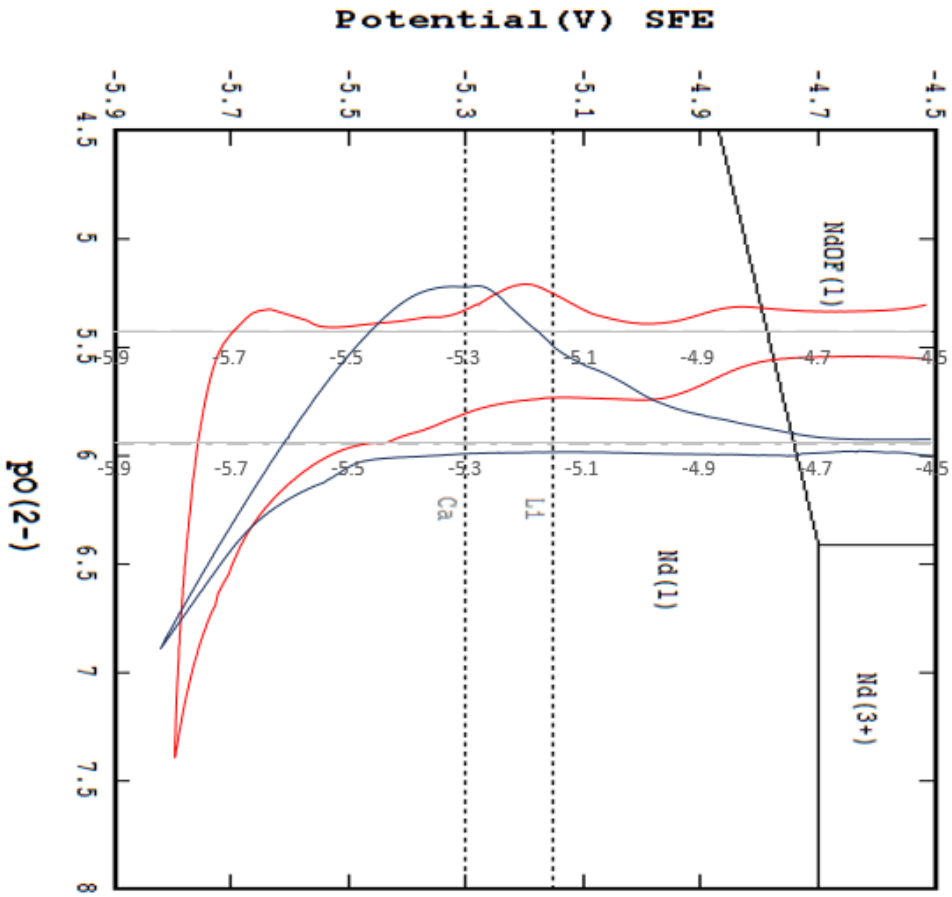

Figure 44: E-pO^{2-} diagram and scaled up cyclic voltammetry of LiF-CaF_2- NdF_3 with both 2.197 (red) and 0.2 wt. %Nd_2O_3 (blue) addition at 1050°C

Additional CV was completed but by adding CaO and Li_2O instead of CaF_2, LiF and Nd_2O_3. In this case, 19.51 wt.% CaO, 41.6 wt.% Li_2O and 38.89 wt.% NdF_3 was used and therefore equivalent to the same CaF_2/LiF ratio except with oxides. However, the source of F^- was only NdF_3 and the source of O^{2-} was not Nd_2O_3. Figure 45 displays the voltammetry results at 1050ºC. Not surprisingly, similar results were obtained. Although the solubility of CaO and

Li_2O in the molten salt was not studied in this research, the plot shows the customary reduction and oxidation of the Ca (A/A'), Li (B/B') and Nd (C/C').

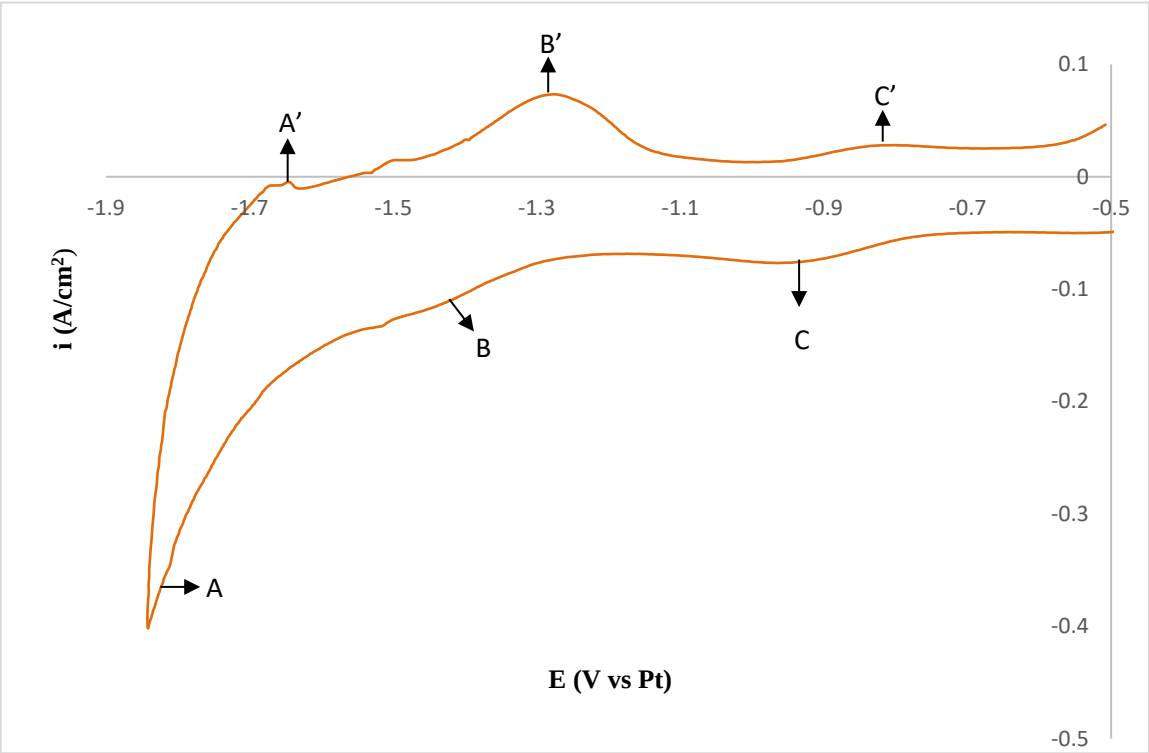

Figure 45: Cyclic voltammogram of Li_2O-CaO-NdF_3 composition in the bath at 1050°C; working electrode: Mo; counter electrode: carbon; reference electrode: Pt; scan rate = 0.001V/s

In reactions similar to Equations 20 and 21 that led to the formation of NdOF, these results suggest Li_2O and CaO release oxide to react with NdF_3 to form NdOF:

$$NdF_3 + O^{2-} = NdOF + 2F^- \qquad \text{Equation 49}$$

After solidification of the melt and removal from the crucible, a purple colored layer was seen at the bottom of the solidified melt which proved to be NdOF formation as illustrated in Figure 46 (a) and (b), these images shows similarities in color when compared with Figure 24(b).

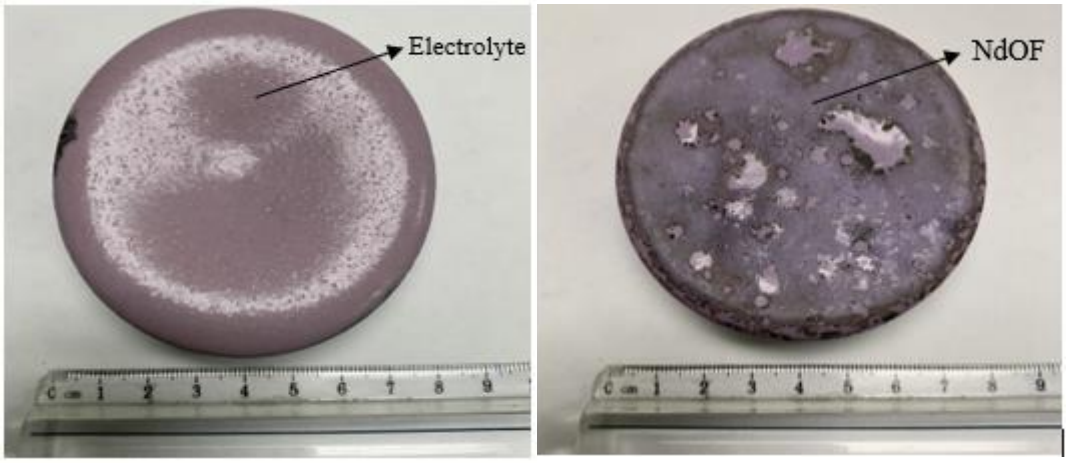

Figure 46: Solidify molten bath where (a) top portion of the spent (b) at the bottom is the NdOF formed

9. Summary

9.1. Conclusions

Molten salt electrolysis in the extraction of rare earths is not a sure bet owing to the nature of the rare earths. Nonetheless, by understanding the thermodynamic considerations, the type of molten bath, decomposition potential, as well as solubility and rare earth properties, optimum results can be achieved.

In molten salt electrolysis, the bath is a twofold service which functions to lower the melting point by means of two or more inert salts but also a solvent to solubilize the reactive metal salt, in this case, rare earth fluoride in the absence or presence of rare earth oxide.

E-pO^{2-} diagrams are used to thermodynamically model the electrolysis of molten salts similar to the E_H-pH diagrams for the electrolysis of aqueous systems. Although the diagrams resemble one another and are similarly used, pO^{2-} and pH are opposite measures for acidity/basicity.

A case study for Nd-electrolysis from LiF-CaF_2-NdF_3 baths was examined to demonstrate the utility of E-pO^{2-} diagrams. Results concur with the literature. Furthermore, results in the absence and presence of Nd_2O_3 dissolved in 72 mol% LiF, 18 mol% CaF_2 and 10 mol% NdF_3 showed that cathode potentials between -4.71V and -5.15V would be needed to make Nd under acidic conditions. However, this window decreased as the basicity increased. When Nd_2O_3 was added, NdOF would form and extend the pO^{2-} window to a lower basicity. From other REEs, an average potential of 5V shown to be a potential at which metals of these REEs can be electrowon. Consequently, it was established that molten salt electrolysis using fluoride salt in the recovery of neodymium metal is possible and metal produced using this technology is much purer.

From the analysis, it was be confirmed that not all of the Nd_2O_3 dissolved in the molten salt. Some reacted to form neodymium oxyfluoride (NdOF). As the Nd_2O_3 content increased, both undissolved Nd_2O_3 and NdOF showed up in the spent bath. Both were found to be heavier and therefore settled to the bottom of the spent bath. This factor decreases the current efficiency because both materials are neutral and do not get attracted to the negatively charged cathode. Furthermore, upon settling, they would no longer be in the vicinity of the cathode so reduction cannot occur. This effect worsened at higher oxide addition levels.

Oxide solubility does increase at higher temperature but not significantly. Thus, metal recovery could improve with higher temperatures but only minimally with increased oxide addition. At increased oxide addition, the recovery drops sharply even at high temperature due to low solubility. Using statistical design of experiment (DOE), process parameters such as dwelling time, melt temperature and Nd_2O_3 addition were defined in detail and a better process regime for the electrolysis process was identified. It was established that higher temperatures, low Nd_2O_3 additions, and short dwelling times will achieve the best performance in neodymium metal recovery and the metal yield from a fluoride bath by this electrowinning technique.

It is known that E_H-pH diagrams are related to cyclic voltammetry for aqueous systems and used to determine extraction conditions at which electrodeposition or electrowinning can be performed. The SHE-electrode is commonly selected for calculations and the SCE-electrode is commonly used for experimental work. For E-pO^{2-} diagrams, cyclic voltammetry can also be used but, unlike aqueous systems that use water as a consistent medium, there is no one bath for fused-salt systems. For this dissertation research, the SFE-electrode was used. However, for this non-aqueous system, the CV results had to be scaled to match the E-pO^{2-} diagram. In this regard, a constant near -4.0V was added to the CV potentials depending on the basicity of the system.

Since the hydrometallurgical method can be used to produce Nd in the form of fluoride or oxide and the pyrometallurgical method for Nd electrowinning, the combination of these processes can be used to recycle the Nd in magnets (and other secondary materials) and thereby help minimize dependence on raw resources which will increase REE sustainability.

9.2. Future Work

Further research is recommended:

1. Use the same experimental approach but with a focus on other REEs (and their E-pO^{2-} diagrams) to see if other rare earth metal can be recovered by electrolysis;
2. Adapt the same experimental approach but increase the temperatures (and their E-pO^{2-} diagrams) to see if Nd recovery and metal yield can be improved;
3. Find ways to get oxyfluoride to react in the molten bath and increase the potential window as well as the log(oxide) window on the E-pO^{2-} diagram;
4. Introduce other variables in more design of experiment studies to see their effects on the metal recovery. Example variables might include continuous stirring of the molten bath, performing these experiments under pressure/vacuum chamber to see if, for example, O_2 pressure can improve metal yield and metal purity, and having other rare earth fluorides present with Nd will still allow pure Nd to be made; and
5. Gas analysis on the off gases coming out from the electrolysis system, particularly for this system F_2, O_2, CO and CO_2.

10. References

1. McLemore, V.T., Rare Earth Elements Deposits in New Mexico, 2014, in Conway, F.M., ed., Proceedings of the 48th Annual Forum on the Geology of Industrial Minerals, Phoenix, Arizona, April 30 - May 4, 2012. Arizona Geological Survey Special Paper #9, Chapter 3, p. 1-16.
2. Krishnamurthy, N., Gupta, C. K., & CRC Press. (2016). *Extractive metallurgy of rare earths*. Boca Raton: CRC Press/Taylor & Francis Group.
3. Tyler, G. (January 01, 2004). Ionic charge, radius, and potential control root/soil concentration ratios of fifty cationic elements in the organic horizon of a beech (Fagus sylvatica) forest podzol. *The Science of the Total Environment, 329,* 1-3.
4. Marc, F. S. (2018) Master of Science thesis, "Surface Chemistry and Modelling of Salicyl Hydroxamic Acid Adsorption at the Surface of Rare Earth Oxide, Carbonate and Phosphates," Montana Tech, Butte MT, USA. pp. 1.
5. Binnemans, K., Jones, P. T., Acker, K., Blanpain, B., Mishra, B., & Apelian, D. (January 01, 2013). Rare-Earth Economics: The Balance Problem. *Jom Warrendale-*, 65, 7, 846-848.
6. Woolley, A. R., & Kjarsgaard, B. A. (January 01, 2008). Paragenetic types of carbonatite as indicated by the diversity and relative abundances of associated silicate rocks: evidence from a global database. *The Canadian Mineralogist, 46,* 4, 741-752.
7. Charalampides, G., Vatalis, K. I., Apostoplos, B., & Ploutarch-Nikolas, B. (January 01, 2015). Rare Earth Elements: Industrial Applications and Economic Dependency of Europe. *Procedia Economics and Finance*, 24, 126-135.

8. Binnemans, K., & Jones, P. T. (January 01, 2014). Perspectives for the recovery of rare earths from end-of-life fluorescent lamps. *Journal of Rare Earths*, 32, 3, 195-200.

9. Van Gosen, B.S., Verplanck, P.L., Seal, R.R., II, Long, K.R., and Gambogi, Joseph, 2017, Rare-earth elements, chap. O *of* Schulz, K.J., DeYoung, J.H., Jr., Seal, R.R., II, and Bradley, D.C., eds., Critical mineral resources of the United States—Economic and environmental geology and prospects for future supply: U.S. Geological Survey Professional Paper 1802, p. O1–O31.

10. Barakos, G., Mischo, H., & Gutzmer, J. (April 01, 2016). An outlook on the rare earth elements mining industry. *Ausimm Bulletin*, 62-66.

11. Pecht, M., & Center for Energetic Concepts Development (College Park, Md.). (2012). *Rare earth materials: Insights and concerns*. College Park, Md: CALCE, EPSC Press.

12. Xu, L., Guo, G., Uy, D., O'Neill, A. E., Weber, W. H., Rokosz, M. J., & McCabe, R. W. (June 01, 2004). Cerium phosphate in automotive exhaust catalyst poisoning. *Applied Catalysis B: Environmental, 50,* 2, 113-125

13. Long, K.R., 2011, The future of rare earth elements; will these high-tech industry elements continue in short supply? U.S. Geological Survey Open-File Report 2011-1189, 41 p. [http://pubs.usgs.gov/of/2011/1189/].

14. Chakhmouradian, A. R., and Wall, F. (2012). Rare earth elements: Minerals, mines,magnets (and more). *Elements* 8, 333–340.

15. Gibson, M., and Parkinson, I. (6 March 2011). Once ignored on the periodic table, don't ignore them now-A rare earth element industry overview. CIBC Report, CIBC World Markets Inc.

16. National Development and Reform Commission. (2012). China rare earth - 2011. Rare Earth Information 4, 4–8.

17. Tan, Q., Li, J., & Zeng, X. (April 03, 2015). Rare Earth Elements Recovery from Waste Fluorescent Lamps: A Review. *Critical Reviews in Environmental Science and Technology*, 45, 7, 749-776.

18. Nawshad Haque, Anthony Hughes, Seng Lim, & Chris Vernon. (January 01, 2014). Rare Earth Elements: Overview of Mining, Mineralogy, Uses, Sustainability and Environmental Impact. *Resources*, 3, 4, 614-635.

19. Humphries, M., Library of Congress., & Federation of American Scientists. (2010). *Rare earth elements: The global supply chain*. Washington, DC: Congressional Research Service, Library of Congress.

20. GE, Lighting. Available online: http://www.gelighting.com (accessed on 11 September 2013).

21. Hurst, C., & Institute for the Analysis of Global Security. (2010). *China's rare earth elements industry: What can the West learn?*. Washington, D.C: Institute for the Analysis of Global Security.

22. USGS. USGS Minerals Information. Available online: http://minerals.usgs.gov/minerals/pubs/commodity/rare_earths (accessed on 11 September 2013).

23. MMTA. Minor Metals Trade Association. Available online: http://www.mmta.co.uk/metals/Ce (accessed on 2 November 2013).

24. Hughes, A.E. Interfacial Phenomena in Y_2O_3-ZrO_2-Based Ceramics: A Surface Science Perspective. *Mater. Sci. Monogr*. 1995, 81, 183–238.

25. Ahmad, Z. (February 01, 2003). The properties and application of scandium-reinforced aluminum. *Jom*, *55*, 2, 35-39.

26. United States. (2011). *Critical materials strategy*.

27. Raw Materials Supply Group. (2014). *Report on critical raw materials for the EU: Report of the Ad-hoc Working Group on defining critical raw materials*. S.L: European Commission, Enterprise and Industry.

28. Binnemans, K., Jones, P. T., Blanpain, B., Van, G. T., Yang, Y., Walton, A., & Buchert, M. (July 15, 2013). Recycling of rare earths: a critical review. *Journal of Cleaner Production*, 51, 1-22.

29. Guyonnet, D., Planchon, M., Rollat, A., Escalon, V., Tuduri, J., Charles, N., Vaxelaire, S., Fargier, H. (November 16, 2015). Material flow analysis applied to rare earth elements in Europe. *Journal of Cleaner Production*, *107*, 215-228.

30. Eggert, R., Wadia, C., Anderson, C., Bauer, D., Fields, F., Meinert, L., & Taylor, P. (November 01, 2016). Rare Earths: Market Disruption, Innovation, and Global Supply Chains. *Annual Review of Environment and Resources*, *41*, 1, 199-222.

31. Lee, J. C. K., & Wen, Z. (January 01, 2016). Rare Earths from Mines to Metals: Comparing Environmental Impacts from China's Main Production Pathways. *Journal of Industrial Ecology*.

32. Goonan, T. G., & Geological Survey (U.S.). (2011). *Rare earth elements: End use and recyclability*. Reston, Va: U.S. Dept. of the Interior, U.S. Geological Survey.

33. Guo, X., Sietsma, J., & Yang, Y. (January 01, 2016). A Critical Evaluation of Solubility of Rare Earth Oxides in Molten Fluorides∗∗AF, alkali metal fluoride; AeF_2, alkali earth

metal fluoride; REO, rare earth oxide; REM, rare earth metal; RF_3, rare earth fluoride. 223-234.

34. U.S. Geological Survey. Minerals Year Book—Rare Earths. Available online: https://minerals.usgs.gov/minerals/pubs/commodity/rare-earth/mcs-2015-raree.pdf (accessed on 9 February 2017).
35. Baolu Zhou, Zhongxue Li, & Congcong Chen. (January 01, 2017). Global Potential of Rare Earth Resources and Rare Earth Demand from Clean Technologies. *Minerals, 7,* 11.)
36. Wang, M. R., and Jia, H. J. (2012). Comments on 'Emission standard of pollutants for rare earths industry'. *Chinese Rare Earths* 33, 98–101
37. Meyer, L., and Bras, B. (2011). "Rare earth metal recycling," in *Sustainable Systems and Technology (ISSST), 2011 IEEE International Symposium*. Chicago: Institute of Electrical and Electronics Engineers, 1–6.
38. Tanaka, M., Oki, T., Koyama, K., Narita, H., & Oishi, T. (January 01, 2013). Recycling of Rare Earths from Scrap. 159-211.
39. Anderson, C.D., Anderson, C.G., Taylor, P.R., (2012). A survey of recycled rare earths metallurgical processing. In: Rare Earths 2012, Proceedings of the 51st Annual Conference of Metallurgists of CIM (COM 2012, Niagara Falls, Ontario, Canada, 30 September 3 October 2012), pp. 411-422.
40. Graedel, T. E., Allwood, J., Birat, J.-P., Buchert, M., Hagelüken, C., Reck, B. K., Sibley, S. F., ... In United Nations Environment Programme. (2011). *Recycling rates of metals: A status report*.
41. Reck, B.K., Graedel, T.E., (2012). Challenges in metal recycling. *Science 337*, 690-695.

42. Tuncuk, A., Stazi, V., Akcil, A., Yazici, E. Y., & Deveci, H. (2012). Aqueous metal recovery techniques from e-scrap: *Hydrometallurgy in recycling. Minerals Engineering, 25*, 1, 28-37.

43. United States Environmental Protection Agency. <Washington, DC>. (2012). *Rare earth elements: A review of production, processing, recycling, and associated environmental Issues.* Washington, D.C: U.S. Environmental Protection Agency.

44. Jha, M. K., Kumari, A., Panda, R., Rajesh, K. J., Yoo, K., & Lee, J. Y. (2016). Review on hydrometallurgical recovery of rare earth metals. *Hydrometallurgy*, 161, 77.

45. Thakur, N. V., Jayawant, D. V., Iyer, N. S., & Koppiker, K. S. (1993). Separation of neodymium from lighter rare earths using alkyl phosphonic acid, PC 88A. *Hydrometallurgy, 34*, 1, 99-108.

46. Preston, J. S. (1996). The recovery of rare earth oxides from a phosphoric acid byproduct. Part 4. *The preparation of magnet-grade neodymium oxide from the light rare earth fraction*. Randburg: Mintek.

47. Lu, D., Horng, J. S., & Hoh, Y. C. (April 01, 1989). The separation of neodymium by *quaternary amine from didymium nitrate solution. Journal of the Less Common Metals*, *149*, 219-224.

48. Morais, C. A., & Ciminelli, V. S. (January 01, 2004). Process development for the recovery of high-grade lanthanum by solvent extraction. *Hydrometallurgy Amsterdam-, 73*, 237-244.

49. Radhika, S., Nagaphani, K. B., Lakshmi, K. M., & Ramachandra, R. B. (January 01, 2011). Solvent extraction and separation of rare-earths from phosphoric acid solutions with TOPS 99. *Hydrometallurgy Amsterdam-, 110*, 50-55.

50. Panda, N., Devi, N., & Mishra, S. (August 01, 2012). Solvent extraction of neodymium (III) from acidic nitrate medium using Cyanex 921 in kerosene. *Journal of Rare Earths*, 30, 8, 794-797.

51. El-Hefny, N. E. (July 01, 2007). Kinetics and mechanism of extraction and stripping of neodymium using a Lewis cell. *Chemical Engineering and Processing: Process Intensification*, *46*, 7, 623-629.

52. Lee, M.-S., Lee, J.-Y., Kim, J.-S., & Lee, G.-S. (January 01, 2006). Solvent extraction of neodymium ions from hydrochloric acid solution using PC88A and saponified PC88A. *Separation and Purification Technology*, *46*, 1, 72.

53. Banda, R., Jeon, H., & Lee, M. (January 01, 2012). Solvent extraction separation of Pr and Nd from chloride solution containing La using Cyanex 272 and its mixture with other extractants. *Separation and Purification Technology*, *98*, 481-487.

54. Guo, C., & Zhi, Y. (July 01, 2017). Effective solvent extraction of La, Ce and Pr from hydrochloric acid with a novel extractant N,N-dihexyloxamic acid. *Journal of Chemical Technology & Biotechnology*, *92*, 7, 1596-1600.

55. Esmaeil Jorjani, & Malek Shahbazi. (January 01, 2016). The production of rare earth elements group via tributyl phosphate extraction and precipitation stripping using oxalic acid. *Arabian Journal of Chemistry. Supplement 2*, *9.*

56. Belova, V. V., Voshkin, A. A., Kholkin, A. I., & Payrtman, A. K. (July 01, 2009). Solvent extraction of some lanthanides from chloride and nitrate solutions by binary extractants. *Hydrometallurgy*, *97*, 198-203.

57. Chen, J., Guo, L., Deng, Y., Li, D., (2013). Application of [A336][P507]/[P204] on High Selective Extraction and Separation of Rare Earths (III) from Mechanism to Techniques.

In: London, I.M., Goode, J.R., Moldoveanu, G., Rayat, M.S. (Eds.), 52nd Conference of Metallurgists (COM). Canadian Institute of Mining Metallurgy and Petroleum, Montreal, Canada, pp. 367–374.

58. Rout, A., Kotlarska, J., Dehaen, W., & Binnemans, K. (September 18, 2013). Liquid–liquid extraction of neodymium(iii) by dialkylphosphate ionic liquids from acidic medium: the importance of the ionic liquid cation Electronic supplementary information (ESI) available: NMR spectra of the ionic liquids. Physical Chemistry *Chemical Physics, 15*, 39, 16533-16541.

59. Conference of Metallurgists, London, I. M., In Goode, J. R., Moldoveanu, G., Rayat, M. S., (2013) Canadian Institute of Mining, Metallurgy and Petroleum. Rare Earth Elements Symposium. Materials Science & Technology Conference. Rare earth elements: Proceedings of the 52nd Conference of Metallurgists (COM), October 27-31, 2013, Montréal, Québec, Canada.

60. Yan, C., Liao, C., Jia, J.W., M. and Li, B., (1999). Comparison of economical and technical indices on rare earth separation processes of bastnasite by solvent extraction. *J. Rare Earths 17 (1)*, 58–63.

61. Tian, X., Yin, X., gong, Y., Wu, Y., Tan, Z., & Xu, P. (November 01, 2016). Characterization, recovery potentiality, and evaluation on recycling major metals from waste cathode-ray tube phosphor powder by using sulphuric acid leaching. *Journal of Cleaner Production, 135*, 1210-1217.

62. Tunsu, C., Petranikova, M., Ekberg, C., & Retegan, T. (March 17, 2016). A hydrometallurgical process for the recovery of rare earth elements from fluorescent lamp waste fractions. *Separation and Purification Technology, 161*, 172-186.

63. Yang, F., Kubota, F., Baba, Y., Kamiya, N., & Goto, M. (June 15, 2013). Selective extraction and recovery of rare earth metals from phosphor powders in waste fluorescent lamps using an ionic liquid system. *Journal of Hazardous Materials*, 79-88.

64. Yoon, H.-S., Kim, C.-J., Chung, K.-W., Kim, S.-D., Lee, J.-Y., & Kumar, J. R. (October 01, 2016). Solvent extraction, separation and recovery of dysprosium (Dy) and neodymium (Nd) from aqueous solutions: Waste recycling strategies for permanent magnet processing. *Hydrometallurgy, 165*, 27-43.

65. Sahin, A. K., Voßenkaul, D., Stoltz, N., Stopic, S., Saridede, M. N., & Friedrich, B. (May 01, 2017). Selectivity potential of ionic liquids for metal extraction from slags containing rare earth elements. *Hydrometallurgy, 169*, 59-67.

66. Jowitt, S. M., Werner, T. T., Weng, Z., & Mudd, G. M. (October 01, 2018). Recycling of the rare earth elements. *Current Opinion in Green and Sustainable Chemistry, 13*, 1-7.

67. Walters, A., Lusty, P., & British Geological Survey. (2010). Rare earth elements. Keyworth, Nottingham, U.K: British Geological Survey.

68. Ueberschaar, M., & Rotter, V. S. (January 01, 2015). Enabling the recycling of rare earth elements through product design and trend analyses of hard disk drives. *Journal of Material Cycles and Waste Management, 17*, 2, 266-281.

69. Yang, Y., Walton, A., Sheridan, R., Guth, K., Gauss, R., Gutfleisch, O., Buchert, M., ... Binnemans, K. (March 01, 2017). REE Recovery from End-of-Life NdFeB Permanent Magnet Scrap: A Critical Review. *Journal of Sustainable Metallurgy, 3*, 1, 122-149.

70. Önal, M. A. R., Borra, C. R., Guo, M., Blanpain, B., & Van, G. T. (June 01, 2017). Hydrometallurgical recycling of NdFeB magnets: Complete leaching, iron removal and electrolysis. *Journal of Rare Earths, 35*, 6, 574-584

71. Zepf V (2013) Rare Earth Elements. Vasa. doi:10.1007/978-3- 642-35458-8 13.

72. Goldman A (1999) *Handbook of modern ferromagnetic materials*. Boston: Kluwer Academic Publishers.

73. Rotter, V. S., Chancerel, P., Ueberschaar, M., & REWAS 2013: Enabling Materials Resource Sustainability - TMS 2013 Annual Meeting and Exhibition. (December 04, 2013). Recycling-oriented product characterization for electric and electronic equipment as a tool to enable recycling of critical metals. *Tms Annual Meeting,* 192-201.

74. Hatch G (2011) Seagate, rare earths and the wrong end of the stick. Technol Met Res

75. Han, W., Li, M., Zhang, M. L., & Yan, Y. D. (January 01, 2016). Progress in preparation of rare earth metals and alloys by electrodeposition in molten salts. *Rare Metals Beijing English Edition, 35,* 11, 811-825.

76. Beaudry, B. J., and Gschneidner, K. A. (1978). Chapter 2 preparation and basic properties of the rare earth metals. In: Gschneidner, K. A., B¨unzli, J. C., and Pecharsky, V., eds. Handbook on the physics and chemistry of rare earths. Amsterdam: Elsevier (pp. 173–232).

77. Xiao, W., & Wang, D.-H. (August 01, 2016). Rare metals preparation by electro-reduction of solid compounds in high-temperature molten salts. *Rare Metals, 35*, 8, 581-590.

78. Gerhartz, W., Yamamoto, Y. S., Pfefferkorn, R., Rounsaville, J. F., & Campbell, F. T. (1986). Ullmann's encyclopedia of industrial chemistry: Vol. A6. (Ullmann's encyclopedia of industrial chemistry / executive editor Wolfgang Gerhartz; editors Barbara Elvers ... [et al.].) Weinheim: VCH.

79. Bose, D. K., Mehra, O. K., & Gupta, C. K. (August 01, 1985). Preparation of rare earth-silicon-iron alloy by metallothermic reduction. *Journal of the Less Common Metals, 110*, 239-242.

80. Meyer, G., & Schleid, T. (January 01, 1986). The metallothermic reduction of several rare-earth trichlorides with lithium and sodium. *Journal of the Less-Common Metals, 116*, 1, 187-197.

81. SHARMA, R. A., & SEEFURTH, R. N. (May 03, 1988). ChemInform Abstract: The Metallothermic Reduction of Nd2O3 with Ca in CaCl2-NaCl Melts. *Cheminform, 19*, 18.

82. Luna, A. J. S., Flores, V. A., Muñiz, V. R., Fuentes, A. F., Torres, J., Rodríguez, R. N., Ortiz, J. C., Orozco, P. (January 01, 2011). Cerium extraction by metallothermic reduction using cerium oxide powder injection. *Journal of Rare Earths, 29*, 1, 74-76.

83. Pang, S., Yan, S., Li, Z., Chen, D., Xu, L., & Zhao, B. (May 01, 2011). Development on molten salt electrolytic methods and technology for preparing rare earth metals and alloys in China. Xiyou Jinshu/*chinese Journal of Rare Metals, 35*, 3, 440-450.Electrochimica Acta, Vol 3, 195-207.

84. Muthmann, W., & Hofer, H. (January 01, 1903). Ueber die Verbrennung des Stickstoffs zu Stickoxyd in der elektrischen Flamme. *Berichte Der Deutschen Chemischen Gesellschaft, 36*, 1, 438-453.

85. http://www.ausetute.com.au/images/elcmx.gif.

86. Morrice, E., Henrie, T. A., & United States. (1967). Electrowinning high-purity neodymium, praseodymium, and didymium metals from their oxides. Washington, D.C.: U.S. Department of the Interior, Bureau of Mines.

87. Murphy, J. E., Dysinger, D. K., & Chambers, M. F. (January 01, 1995). Electrowinning Neodymium Metal from Chloride and Oxide-fluoride Electrolytes. Light Metals, 1313.

88. Grebnev, V. A., & Dmitrienko, V. P. (2007*). Obtaining neodymium from melts by electrolysis*. Томский политехнический университет.

89. Stefanidaki, E., Hasiotis, C., & Kontoyannis, C. (May 01, 2001). Electrodeposition of neodymium from LiF–NdF_3–Nd_2O_3 melts. *Electrochimica Acta, 46,* 17, 2665-2670.

90. Abbasalizadeh, A., Teng, L., Sridhar, S., & Seetharaman, S. (October 02, 2015). Neodymium extraction using salt extraction process. *Mineral Processing and Extractive Metallurgy, 124,* 4, 191-198.

91. Shirayama, S., & Okabe, T. H. (June 01, 2018). Selective Extraction and Recovery of Nd and Dy from Nd-Fe-B Magnet Scrap by Utilizing Molten $MgCl_2$. *Metallurgical and Materials Transactions B, 49,* 3, 1067-1077.

92. Zhu, H. (2014). Rare Earth Metal Production by Molten Salt Electrolysis, 1765-1772.

93. Hamel, C., Chamelot, P., Taxil, P. (June 25, 2004). Neodymium (III) cathodic processes in molten fluorides. Electrochimica *Acta, 49,* 4467- 4476.

94. Thudum, R., Srivastava, A., Nandi, S., Nagaraj, A., & Shekhar, R. (January 01, 2010). SHORT COMMUNICATION: Molten salt electrolysis of neodymium: electrolyte selection and deposition mechanism. *Transactions- Institution of Mining and Metallurgy Section C Mineral Processing and Extractive Metallurgy, 119,* 2, 88-92.

95. Huang, C., Liu, X., Gao, Y., Liu, S., & Li, B. (January 01, 2016). Cathodic processes of neodymium (iii) in LiF-NdF_3-Nd_2O_3 melts. *Faraday Discussions, 190,* 339-49.

96. Vogel, H., Flerus, B., Stoffner, F., & Friedrich, B. (March 01, 2017). Reducing Greenhouse Gas Emission from the Neodymium Oxide Electrolysis. Part I: Analysis of the Anodic Gas Formation. *Journal of Sustainable Metallurgy, 3*, 1, 99-107.

97. Bukatova, G. A., Kuznetsov, S. A., & Gaune-Escard, M. (August 01, 2007). Electrochemical synthesis of rare-earth metal (Eu, Nd) borides in molten salts. Russian *Journal of Electrochemistry, 43*, 8, 929-935.

98. Carlson, O. N., & Schmidt, F. A. (1961a). Metallothermic preparation of yttrium metal. In Spedding, F. H. and Daane, A. H. (eds.), The Rare Earths. John Wiley, New York. pp. 113-125.

99. Takeda, O., Nakano, K., & Sato, Y. (February 14, 2014). Recycling of rare earth magnet waste by removing rare earth oxide with molten fluoride. *Materials Transactions, 55*, 2, 334-341.

100. Abbasalizadeh, A., Malfliet, A., Seetharaman, S., Sietsma, J., & Yang, Y. (January 01, 2017). Electrochemical extraction of rare earth metals in molten fluorides: Conversion of rare earth oxides into rare earth fluorides using fluoride additives. *Journal of Sustainable Metallurgy, 3*, 3.

101. Doyle, F. M. (September 01, 2005). Teaching and learning environmental hydrometallurgy. *Hydrometallurgy, 79*, 1-14.

102. Um, N. (July 26, 2017). Hydrometallurgical Recovery Process of Rare Earth Elements from Waste: Main Application of Acid Leaching with Devised τ-T Diagram.

103. Dring K., Dashwood R. & Inman D. (2005). Predominance Diagrams for Electrochemical Reduction of Titanium Oxides in Molten $CaCl_2$, *J. of Electrochemical Society, 152*, 10.

104. Mansfeld, F. and Bertocci, U. (2011). Electrochemical corrosion testing. Symposium on Progress in Elecrochemical Corrosion Testing. Philadelphia, Pa: American Society for Testing and Materials.

105. Jiao S. and Zhu H. (May 30, 2011). An investigation into the Electrochemical Recovery of Rare Earth Ions in a CsCl-based Molten Salt, *Journal of Hazardous Materials,189*, 3, 821-826.

106. Edeleanu, C., & Littlewood, R. (January 01, 1960). Thermodynamics of corrosion in fused chlorides. *Electrochimica Acta, 3,* 3, 195-207.

107. Janz, G. J., & Tompkins, R. P. T. (1972). *Nonaqueous electrolytes handbook: V. 1*. New York: Academic Press.

108. Brajendra, M. and David, L.O. (2004). Molten salt applications in materials processing.

109. Basin, A. S., Kaplun, A. B., Meshalkin, A. B., & Uvarov, N. F. (September 01, 2008). The LiCl-KCl binary system. *Russian Journal of Inorganic Chemistry, 53*, 9, 1509-1511.

110. Trulove, P. C., & Electrochemical Society (U.S.). (2002*). Molten salts XIII*: *Proceedings of the international symposium.* Pennington, N.J: Electrochemical Society.

111. Korin, E., & Soifer, L. (January 01, 1997). Thermal analysis of the system KCl-LiCl by differential scanning calorimetry. *Journal of Thermal Analysis, 50*, 3, 347-354.

112. Ghosh, S., Ganesan, R., Sridharan, R., & Gnanasekaran, T. (December 01, 2018). Investigation on the Phase Diagram of LiCl-KCl-$NdCl_3$ Pseudo-Ternary System. *Journal of Phase Equilibria and Diffusion, 39*, 6, 916-932.

113. Outokumpu Research, Finland, 2002, HSC Chemistry for Windows, Chemical Reaction and Equilibrium Software with extensive Thermochemical Database.

114. Kubaschewski, O., & Evans, E. L. (1958). *Metallurgical thermochemistry*. London: Pergamon Press.

115. Littlewood, R. (January 01, 1962). Diagrammatic Representation of the Thermodynamics of Metal-Fused Chloride Systems. *Journal of the Electrochemical Society, 109,* 6, 525.

116. Wang, J. (2006). Analytical electrochemistry. Hoboken, NJ: J. Wiley.

117. Seeber, R., Zanardi, C., & Inzelt, G. (June 01, 2016). The inherent coupling of charge transfer and mass transport processes: the curious electrochemical reversibility. *Chemtexts, 2*, 2.

118. Balluffi, R. W., Allen, S. M., & Carter, W. C. (2005). *Kinetics of materials*. Hoboken, N.J: Wiley-Interscience.

119. Sarfo, P., Young, C. and Huang, H.H. (2019). Consideration and Construction of Potential-pO2-Diagrams with Emphasis on Molten Salt Electrolysis of Neodymium Metal from its Oxide, Mining, xx Journal, Vol Y, xx-yy.

120. Merrill, D. R., Bikson, M., & Jefferys, J. G. (January 01, 2005). Electrical stimulation of excitable tissue: design of efficacious and safe protocols. *Journal of Neuroscience Methods, 141*, 2, 171-98.

121. Okada, T. (January 01, 1998). Interpretation of Ion-Exchange Chromatographic Retention Based on an Electrical Double-Layer Model. *Analytical Chemistry, 70*, 9, 1692.

122. Lyklema, J. (1971). *The Electrical Double Layer on Oxides*. Croatian Chemical Society.

123. Li, Y., Zhang, G.-F., He, Y.-Y., & Hou, X.-D. (January 01, 2012). Electrical Double Layer Model and Thermodynamic Coupling for Electrochemically Deposited Hydrogenated Amorphous Carbon Films. *Journal- Electrochemical Society, 159,* 12.

124. Nagy, T., Boda, D., & Henderson, D. (October 06, 2011). Simulation of an electrical double layer model with a low dielectric layer between the electrode and the electrolyte. *Journal of Physical Chemistry B, 115*, 39, 11409-11419.

125. Islam, M. M., Alam, M. T., & Ohsaka, T. (October 23, 2008). Electrical Double-Layer Structure in Ionic Liquids: A Corroboration of the Theoretical Model by Experimental Results. *The Journal of Physical Chemistry C, 112*, 42, 16568-16574.

126. A. Mallik, & B.C. Ray. (2011). *Evolution of Principle and Practice of Electrodeposited Thin Film: A Review on Effect of Temperature and Sonication. International Journal of Electrochemistry.*

127. Shiguan, C., Xiaoyong, Y., Zhogxing, Y. and Qingtao, L. (1994) Rare Metals 13, 46.

128. STABCAL, version 2019; Stability Calculation for Aqueous and Nonaqueous System; Montana Tech: Butte, MT, USA, 2019.

129. Dysinger, D. K., & Murphy, J. E. (1994). *Electrowinning of neodymium from a molten oxide-fluoride electrolyte*. Washington, D.C.: U.S. Dept. of Interior, Bureau of Mines.

130. Hamlin, J. D., and N. E. Richards. (1963). Studies of the Anode Gas from the Hall-Heroult Cell. Paper in Proceedings of 1st International Symthe Hall-Heroult Cell and Proceedings of 1st International Symposium on the Extractive Metallurgy of Aluminum. Wiley, pp.51-63. 12.

131. Gunawan, A. (2015) Master of Science thesis, “Thermodynamic Considerations in Molt Electrolysis for Rare Earth Metals,” Montana Tech, Butte MT, USA. pp. 30-35

132. Tamamura, H., Shimooka, T. and Utsunomiya, M. (1990). Proc. Seventh Int. *Symp. Molten Salts, 90*, 17, 611.

133. Kaneko, A., Yamamoto, Y. & Okada, C. (1993). “Electrochemistry of rare earth fluoride molten salts”, *J. Alloys Compd*, *193*, 44– 46.10.

134. Shi, Y., Liu, X., Gao, Y., Huang, C., & Bing Li, B. (March 7, 2017). Electrochemical Behavior of Dy (III) and Dy-Fe Alloys Preparation by Co-Reduction in Molten Fluoride Salts. *Journal of The Electrochemical Society*, *164*, 4, D263-D268.

135. Knudson, G., & State Univ. of Iowa, Iowa City. (August 01, 1954). Preparation and properties of the rare earth fluorides and oxyfluorides. *Journal of the American Chemical Society*, 3921-2.

136. Kolovos, K., Tsivilis, S., & Kakali, G. (January 01, 2005). SEM examination of clinkers containing foreign elements. *Cement and Concrete Composites*, *27*, 2, 163-170.

137. Sarfo, P., Wyss, G., Ma, G., Das, A., & Young, C. (June 01, 2017). Carbothermal reduction of copper smelter slag for recycling into pig iron and glass. *Minerals Engineering*, *107*, 8-19.

138. Sarfo, P., Das, A., Young, C., & Wyss, G. (December 01, 2017). Recovery of metal values from copper slag and reuse of residual secondary slag. *Waste Management*, *70*, 272-281

139. Box, G. E. P., & Behnken, D. W. (November 01, 1960). Some New Three Level Designs for the Study of Quantitative Variables. *Technometrics*, *2*, 4, 455-475.

140. Bezerra, M. A., Santelli, R. E., Oliveira, E. P., Villar, L. S., & Escaleira, L. A. (September 15, 2008). Response surface methodology (RSM) as a tool for optimization in analytical chemistry. *Talanta*, *76*, 5, 965-977.

141. Stat-Ease, Inc. (2003). Design-ease: Software for design of experiments. Minneapolis, MN: Stat-Ease.

142. Ciumag, M., Gibilaro, M., Massot, L., Laucournet, R., & Chamelot, P. (April 01, 2016). Neodymium electrowinning into copper-neodymium alloys by mixed oxide reduction in molten fluoride media. *Journal of Fluorine Chemistry*, 184, 1-7.

143. Mukherjee, A., Van, D. J., Blanpain, B., Guo, M., & Mukherjee, A. (February 01, 2017). CSLM study on the interaction of Nd_2O_3 with $CaCl_2$ and CaF_2-LiF molten melts. *Journal of Materials Science, 52*, 3, 1717-1726.

144. Valero, V. C., & Igual, M. A. (January 01, 2013). Influence of protein adsorption on corrosion of biomedical alloys. 187-219.

145. Rani, S., Abdullah, W. F. H., Zain, Z. M., & N.Z.N, A. (March 01, 2018). Integrated Circuit Design of 3 Electrode Sensing System Using Two-Stage Operational Amplifier. Iop Conference Series: *Materials Science and Engineering, 340*, 12017.

146. Woods, R., Young, C. A., & Yoon, R. H. (December 01, 1990). Ethyl xanthate chemisorption isotherms and E_H-pH diagrams for the copper/water/xanthate and chalcocite/water/xanthate systems. *International Journal of Mineral Processing, 30*, 17-33.

147. Young, C.A., Woods, R., Yoon, R.H. (1988). A voltammetric study of chalcocite oxidation to metastable copper sulfides. In: Richardson, P.E., Woods, R. (Eds.)., Proc. Int. Symp. Electrochemistry in Mineral and Metal Processing II. Electrochem. Soc., Pennington, NJ, pp. 3–17.

148. Koch, D. F. A., & McIntyre, R. J. (August 01, 1976). The application of reflectance spectroscopy to a study of the anodic oxidation of cuprous sulphide. *Journal of Electroanalytical Chemistry and Interfacial Electrochemistry, 71*, 3, 285-296.

149. Grujicic, D., & Pesic, B. (July 01, 2002). Electrodeposition of copper: the nucleation mechanisms. *Electrochimica Acta*, *47*, 18, 2901-2912.

150. Grujicic, D., & Pesic, B. (January 01, 2005). Reaction and nucleation mechanisms of copper electrodeposition from ammoniacal solutions on vitreous carbon. *Electrochimica Acta*, *50*, 22, 4426-4443.

151. Simka, W., Puszczyk, D., & Nawrat, G. (September 30, 2009). Electrodeposition of metals from non-aqueous solutions. *Electrochimica Acta*, *54*, 23, 5307-5319.

152. Jeong, S. M., Shin, H.-S., Cho, S.-H., Hur, J.-M., & Lee, H. S. (November 01, 2009). Electrochemical behavior of a platinum anode for reduction of uranium oxide in a LiCl molten salt. *Electrochimica Acta*, 54, 26, 6335-6340.

153. Hur, J.-M., Jeong, S. M., & Lee, H. (May 01, 2010). Underpotential deposition of Li in a molten LiCl–Li2O electrolyte for the electrochemical reduction of U from uranium oxides. *Electrochemistry Communications*, *12*, 5, 706-709.

Appendix A: Response for Metal Yield

ANOVA for Response Surface Reduced Cubic model
Analysis of variance table [Partial sum of squares - Type III]

Source	Sum of Squares	df	Mean Square	F Value	p-value Prob > F	
Model	9.67	11	0.88	17.92	0.0026	significant
A-Nd2O3	*0.74*	*1*	*0.74*	*15.13*	*0.0115*	
B-Time	*0.035*	*1*	*0.035*	*0.71*	*0.4384*	
C-Temp	*4.32*	*1*	*4.32*	*88.06*	*0.0002*	
AB	*0.052*	*1*	*0.052*	*1.06*	*0.3511*	
AC	*0.21*	*1*	*0.21*	*4.37*	*0.0908*	
BC	*0.079*	*1*	*0.079*	*1.60*	*0.2610*	
A^2	*0.019*	*1*	*0.019*	*0.38*	*0.5655*	
B^2	*0.079*	*1*	*0.079*	*1.62*	*0.2592*	
C^2	*0.16*	*1*	*0.16*	*3.31*	*0.1284*	
A^2B	*0.19*	*1*	*0.19*	*3.93*	*0.1041*	
A^2C	*8.587E-003*	*1*	*8.587E-003*	*0.18*	*0.6931*	
Residual	0.25	5	0.049			
Lack of Fit	*7.932E-003*	*1*	*7.932E-003*	*0.13*	*0.7332*	*not significant*
Pure Error	*0.24*	*4*	*0.059*			
Cor Total	9.92	16				

Std. Dev.	0.22		R-Squared	0.9753
Mean	1.15		Adj R-Squared	0.9208
C.V. %	19.28		Pred R-Squared	N/A
PRESS	N/A		Adeq Precision	13.739Case(s) with leverage of 1.0000: Pred R-Squared and PRESS statistic not defined

Appendix B: One Factor and Interaction Plot on Metal Yield

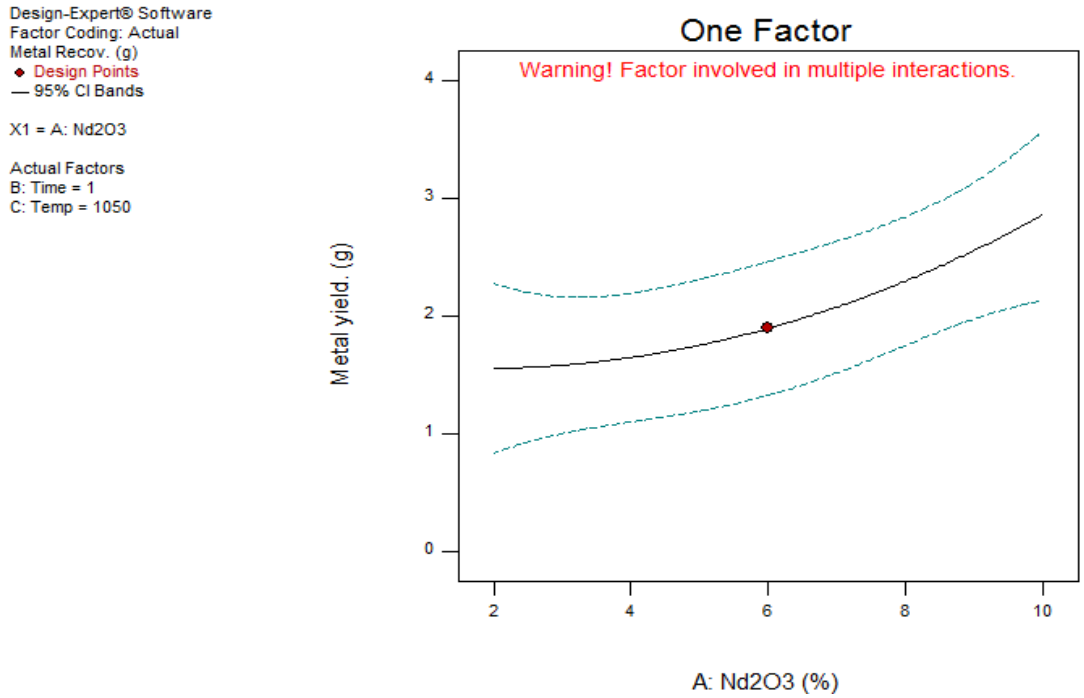

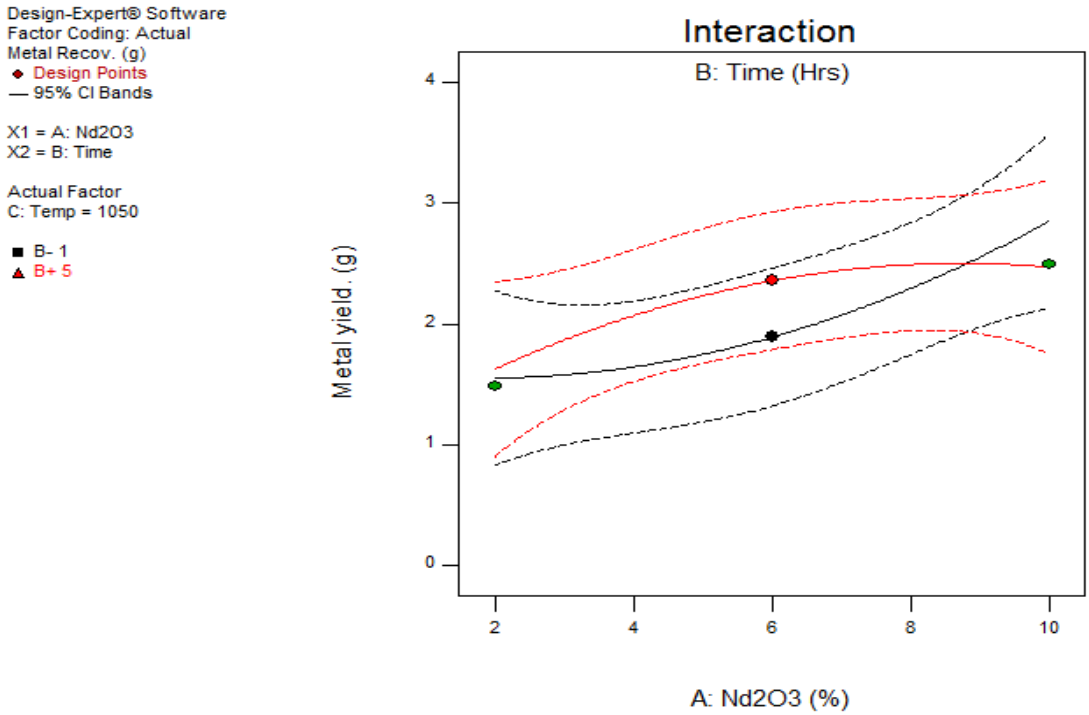

Appendix C: Predicted vs. Actual and Cook's Distance plot on Metal Yield

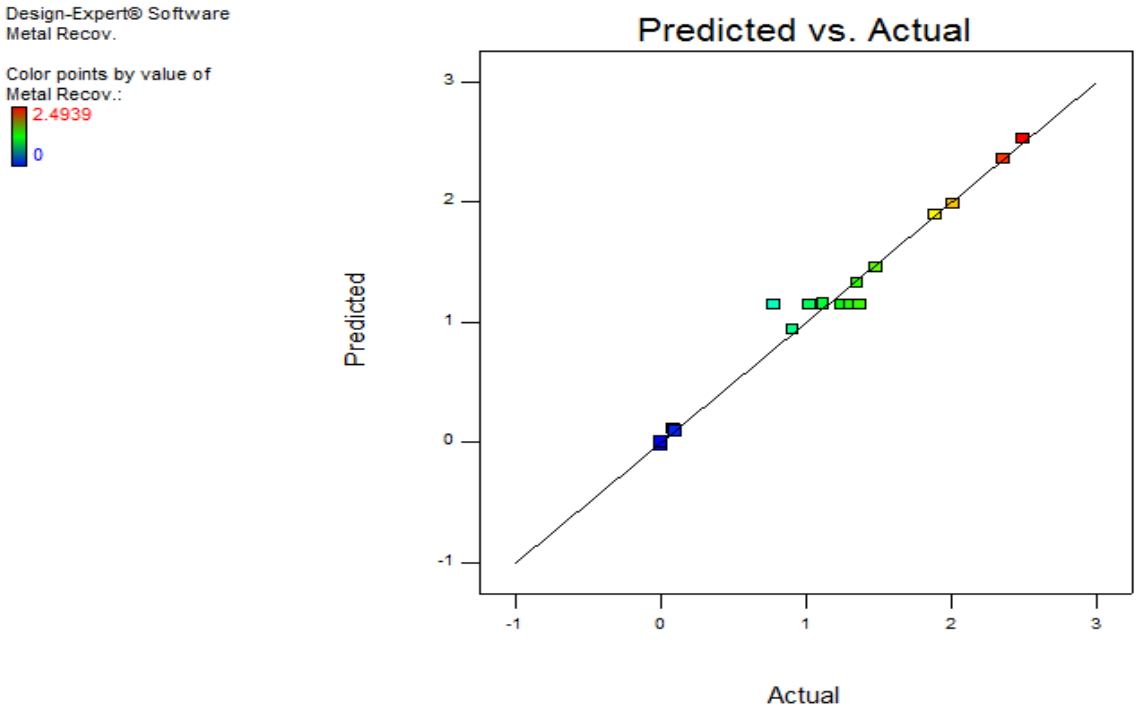

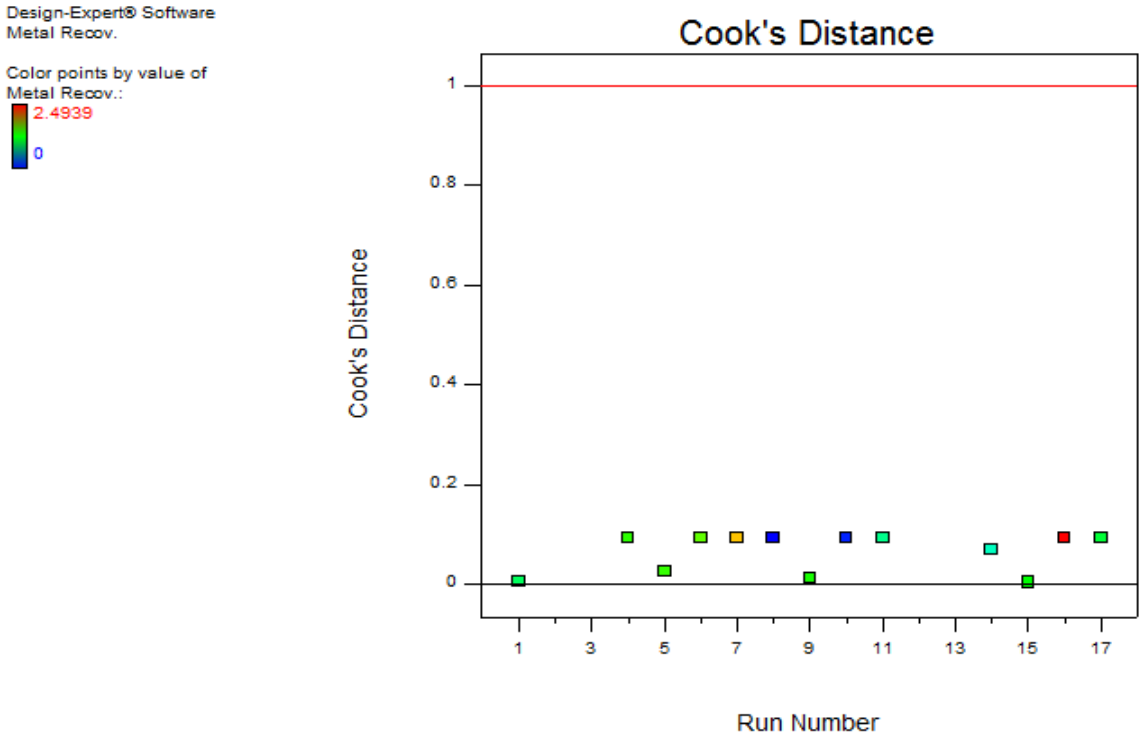

Appendix D: Recovery of Nd Metal from Nd Oxide

ANOVA for Response Surface Reduced Cubic model
Analysis of variance table [Partial sum of squares - Type III]

	Sum of		**Mean**	**F**	**p-value**	
Source	**Squares**	**df**	**Square**	**Value**	**Prob > F**	
Model	1287.59	11	117.05	44.48	0.0003	significant
A-Nd2O3	*112.57*	*1*	*112.57*	*42.77*	*0.0013*	
B-Time	*1.85*	*1*	*1.85*	*0.70*	*0.4401*	
C-Temp	*229.83*	*1*	*229.83*	*87.33*	*0.0002*	
AC	*120.34*	*1*	*120.34*	*45.73*	*0.0011*	
BC	*4.20*	*1*	*4.20*	*1.60*	*0.2621*	
A^2	*93.47*	*1*	*93.47*	*35.51*	*0.0019*	
B^2	*12.12*	*1*	*12.12*	*4.60*	*0.0847*	
C^2	*19.17*	*1*	*19.17*	*7.28*	*0.0429*	
A^2B	*12.90*	*1*	*12.90*	*4.90*	*0.0777*	
A^2C	*20.22*	*1*	*20.22*	*7.68*	*0.0393*	
AB^2	*8.78*	*1*	*8.78*	*3.34*	*0.1274*	
Residual	13.16	5	2.63			
Lack of Fit	*0.67*	*1*	*0.67*	*0.22*	*0.6667*	*not significant*
Pure Error	*12.49*	*4*	*3.12*			
Cor Total	1300.75	16				

Std. Dev.	1.62		R-Squared	0.9899
Mean	10.37		Adj R-Squared	0.9676
C.V. %	15.64		Pred R-Squared	N/A
PRESS	N/A		Adeq Precision	23.837Case(s) with leverage of 1.0000: Pred R-Squared and PRESS statistic not defined

Appendix E: One Factor and Interaction Plot on Nd Recovery

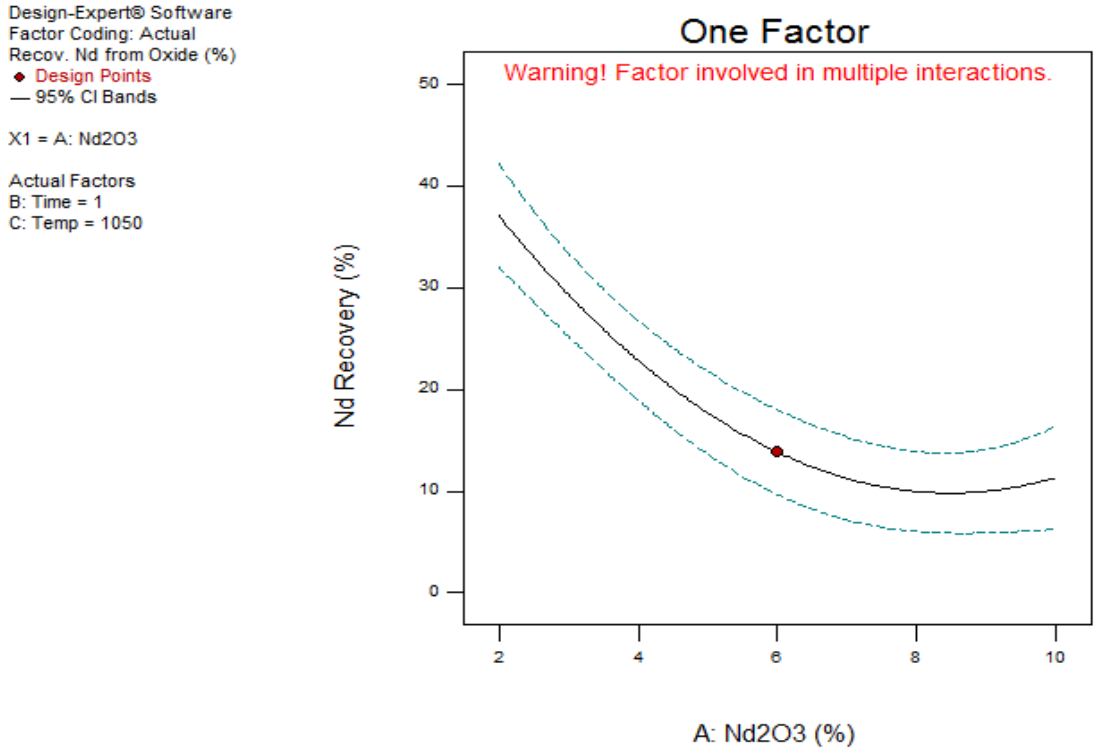

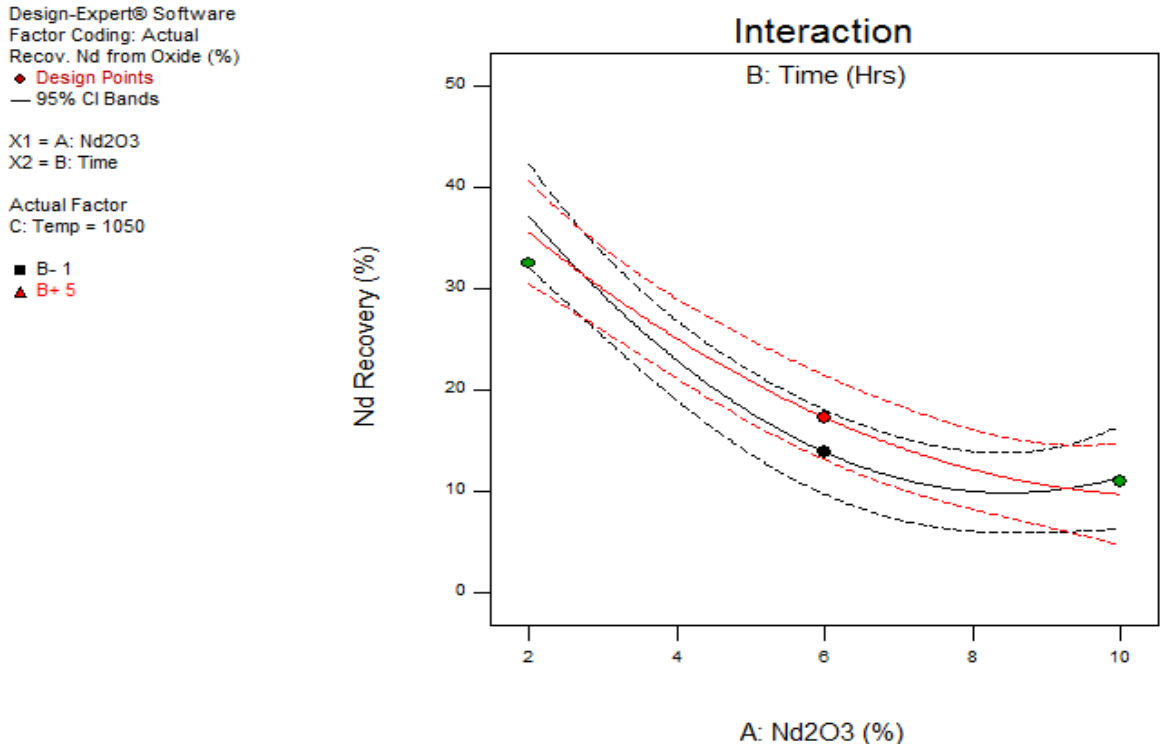

Appendix F: Predicted vs. Actual and Cook's Distance plot on Metal Yield

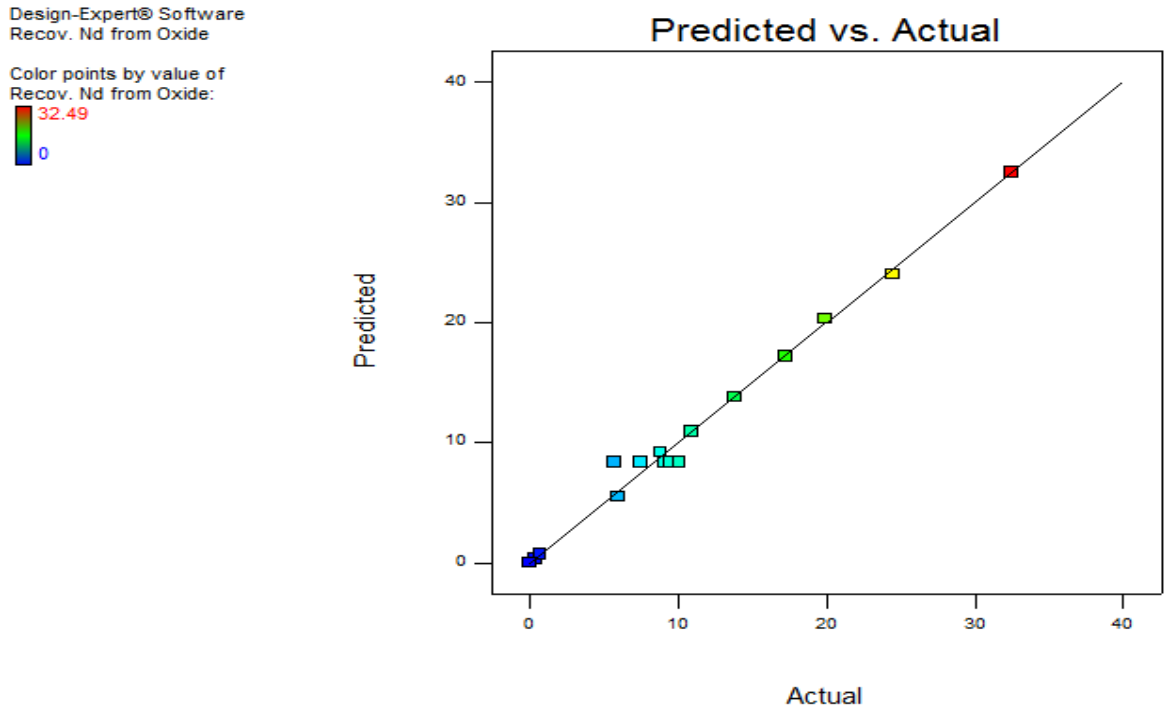

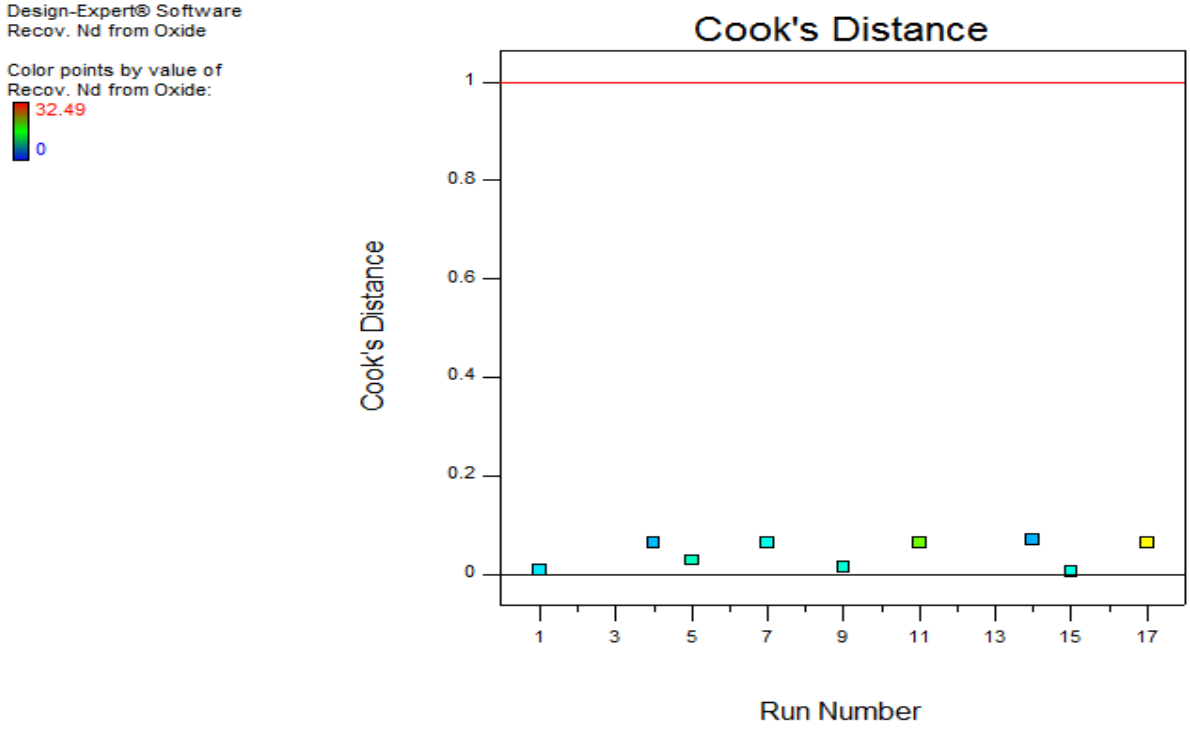

Appendix G: Point Prediction Table and Conformation Report

Factor	Name	Level	Low Level	High Level	Std. Dev.	Coding
A	Nd_2O_3	2.20	2.00	10.00	0.000	Actual
B	Time	1.00	1.00	5.00	0.000	Actual
C	Temp	1050.00	950.00	1050.00	0.000	Actual

	Predicted	Predicted			CI for	Mean	99% of	Population
Response	**Mean**	**Median**	**Std Dev**	**SE Mean**	**95% CI low**	**95% CI high**	**95% TI low**	**95% TI high**
Metal Yield.	1.55574	1.55574	0.221504	0.266376	0.871004	2.24048	-0.239964	3.35145
Nd Recovery from Oxide	35.4801	35.4801	1.62229	1.87315	30.665	40.2951	22.5981	48.362

Confirmation Report						
Two-sided	**Confidence =**	**95%**	**n =**	**1**		
Factor	**Name**	**Level**	**Low Level**	**High Level**	**Std. Dev.**	**Coding**
A	Nd_2O_3	2.20	2.00	10.00	0.000	Actual
B	Time	1.00	1.00	5.00	0.000	Actual
C	Temp	1050.00	950.00	1050.00	0.000	Actual

	Predicted	Predicted						
Response	**Mean**	**Median**	**Std Dev**	**n**	**SE Pred**	**95% PI low**	**Data Mean**	**95% PI high**
Metal Recov.	1.55574	1.55574	0.221504	1	0.35	0.67		2.45
Recov. Nd from Oxide	35.4801	35.4801	1.62229	1	2.48	29.11		41.85